DIRECT NUMERICAL SIMULATIONS OF INTERFACIAL TURBULENCE AT LOW FROUDE AND WEBER NUMBERS

A Dissertation

by

QI ZHANG

Submitted to the Office of Graduate and Professional Studies of
Texas A&M University
in partial fulfillment of the requirements for the degree of

DOCTOR OF PHILOSOPHY

Chair of Committee,	Robert A. Handler
Committee Members,	Kumbakonam Rajagopal
	Devesh Ranjan
	Serap Savari
Head of Department,	Andreas A. Polycarpou

May 2014

Major Subject: Mechanical Engineering

ABSTRACT

Sea surface temperature accessible through use of remote sensing techniques (IR imaging, etc.) suggests abundant flow and thermal field information at the ocean surface that is closely related to subsurface turbulent activities. The suggested information includes wind stress, surface dissipation, underneath velocity and vorticity, and heat and gas transportation. Due to the constantly outgoing interfacial latent and sensible heat flux, the very surface of the ocean is often cooler than the bulk. This so called 'cool skin layer' below the very surface is greatly involved in the underlying interfacial turbulence and is the primary support of using sea surface temperature imaging to detect the subsurface activities. In addition, studies have shown that for this detection method the effects of ubiquitous surfactants (surface free agents) to the subsurface turbulence should also be considered.

In the case when the wind stress at the surface is far less significant than the buoyancy force in the water phase, the cool skin layer accumulates and triggers free convection. A series of numerical simulations is conducted to reproduce such a free convection flow to obtain detailed statistics and structural features in order to investigate the correlation between the surface temperature and the subsurface activities of the flow. The simulations are also aimed at the quantitative evaluation of the surfactant effects on the flow. The results of the simulations demonstrate that the surface temperature is statistically and structurally correlated to the subsurface activities in various patterns, and that surfactant has a certain influence to the subsurface turbulence with an overall effect of reducing the average surface temperature.

Based upon the framework of the controlled flux method, a novel approach to actively determine the interfacial gas transfer velocity at the free convection surface is proposed and numerically investigated. The proposed and simulated approach employs a temporal

volumetric heating source to suppress the free convection. The heating source is defined and parameterized with respect to the physical properties of radiation absorption in water phase. Observation and interpretation of the surface temperature evolution and the flow features during and after the heating suggest the effective suppression of the free convection, the onset of the Rayleigh instability and the re-establishment of the free convection. Based on that, an analytical conduction model is formulated to obtain the heat transfer velocity at the free surface from the surface temperature. The gas transfer velocity is then inferred through similarity.

DEDICATION

This dissertation is dedicated to my beloved parents Yongquan Zhang and Xiuli Li for their unconditional support and encouragement, to my lovely little sister Yan Zhang, and to my grandma, Deying Tian, with whom I spent my childhood.

ACKNOWLEDGEMENTS

I would like to express my sincere gratitude to my advisor, Dr. Handler, for his invaluable support, deep insights of the area, inspiring mental guidance and warm encouragement all through my graduate research, that is not only essential to my doctoral study, but will also benefit and enlighten my career in the future.

I also appreciate my committee members, Dr. Rajagopal, Dr. Ranjan and Dr. Savari, for their time and precious advice throughout the course of this research.

Thanks to my friends, colleagues, and the department faculty and staff for making my time at Texas A&M University a great experience.

TABLE OF CONTENTS

Page

LIST OF FIGURES

FIGURE Page

LIST OF TABLES

TABLE Page

1. INTRODUCTION

1.1 Background

Recent development of remote sensing techniques (IR imaging, etc.) and their applications in the measurement and estimation of surface temperature of geophysical flows have excited the exploration of relationships between the temporal and spatial surface temperature signal and the underlying flow and thermal field information, such as surface wind stress, surface dissipation, air-water heat and gas transfer velocity. These types of flow and thermal information are of great significance in environmentalogy, oceanography, and meteorology. For example, estimation of greenhouse gas absorption and release from ocean is of interest in climate system study[1].

The flow and heat transfer processes at sea surface is very complicated. In terms of interface topology, the local surface deformation patterns can be categorized into 4 classes based on the capability of the most energetic turbulent eddies to disturb the surface. The capability is measured with two ratios of the eddy's characteristic kinetic energy versus both gravitational energy and surface tension energy, each corresponds to one of the two major restoration forces, the gravity force and surface tension force that act against the surface deformation. The two ratios are denoted as Froude number Fr and Weber number We respectively. The 4 classes of the local surface deformation patterns now correspond to both, either or none of Fr and/or We being significantly greater than unity. In the high Fr or We cases, there are breaking or non-breaking waves, capillary waves or bubbles. In the low Fr and We case the local surface deformation is considered negligible, the examples are sea surface, lakes and dams under very swift wind.

In general, the latent and sensible heat flux are outwards from the immediate interface, while the solar radiation is inwards with certain absorption depth (1cm to 10cm), as a

result, the overall effect of the total sea surface heat flux is that the very surface of the water tends to be cooler than below. The cooling effect is enhanced by the existence of aqueous viscous boundary layer, within which molecular diffusion dominates compared to turbulent transport, and heat diffuses much slower. The thermal boundary layer at the sea surface is also referred to as the 'cool skin layer'[2]. The cool skin layer is greatly influenced by the underlying turbulent motion, and the sea surface temperature variation obtained through IR imaging is indeed a projection of the subsurface activities.

Specifically, in the case of low Fr and We, when the surface is flat and in quiescent appearance, the flow beneath surface can still be turbulent[3, 4, 5, 6]. In this scenario, if it is hypothesized that the hydrodynamic and physicochemical characteristics of the exterior surface of water phase are not affected by those of the adjacent air phase, the flow is referred to as free surface convection[7, 8]. In this case, the wind shear stress is also negligible, due to the aforementioned surface cooling, the thickness of the aqueous thermal boundary layer (cool skin layer) keeps increasing until Rayleigh instability is triggered and circular motion is initiated. Direct numerical simulations especially spectral methods are most conveniently employed for this low Fr and We free convection flows by virtue of their higher accuracy, higher resolution, and simultaneous access to the flow and thermal field compared to experiments.

Previous studies have shown that surface free agents (surfactants), which are usually generated by ocean organisms or human activities and ubiquitously exist at sea surface, have effects on a wide variety of surface activities including surface waves, surface signature of ship wakes, mesoscale geophysical flows, small scale laminar and turbulent flows, thermal signature of ocean surface, and gas transport across the air-sea interface. Therefore, it is necessary to consider the surfactant effects as one of the primary factors in investigation of the relationships between the IR image of sea surface temperature and the subsurface turbulence. Regarding the free surface convection flow, surfactant can signif-

icantly alter interfacial elasticity, affect the cool skin layer and the subsurface advection, and in consequence change the average sea surface temperature. Nevertheless, for free convection flow, a comprehensive study to quantitatively evaluate the surfactant effects on surface temperature, subsurface flow, and thermal structures and statistics is yet seen elsewhere.

Upon use of the IR imaging of sea surface temperature to infer the gas transfer velocity across air-sea interface, the 'controlled flux method'[9] has made an inspiring approach. Based on the similarity of heat and gas transfer in water phase, the approach employs heat as the tracer. By heating up the water surface and tracking the surface temperature evolution, the characteristic time scale of the heat/gas transfer velocity was successfully inferred. However, the theoretical satisfaction and practical calibration of the 'controlled flux method' require subsurface turbulence modeling, which is a problem without a universally accepted solution. To overcome this difficulty, in this study we propose to further heat up the water surface to actively suppress the subsurface turbulence activity and to explore possible access of heat/gas flux through the surface temperature measurement during the interference of the turbulence convection. In addition, the strong heating at surface may resemble the warm layer stratification under strong solar radiation in ocean[10, 11].

1.2 Literature review

1.2.1 Thermal signature of ocean surface and related subsurface dynamics

A great number of studies have been done on interpretation of IR images of ocean surface. These studies include in-situ measurements on ships and buoys, laboratory experiments in the effort of reproducing ocean surface circumstances, numerical simulations to emulate subsurface dynamics and statistics, and theoretical modeling for example surface renewal model and surface strain model.

Among the great amount of works for measuring and resolving the sea surface thermal signature, Marmorino et al.[12, 13, 14, 15] obtained IR images of the sea surface in the

study of Lanmuir circulation, surface slicks and subsurface turbulence. Chickadel et al.[16, 17] employed the thermal IR based PIV during the interruption of the cool skin layer of turbulent flow to estimate turbulent statistics, surface velocity, turbulence kinetic energy and dissipation. Jessup et al.[18, 19, 20] used the infrared measurement to determine the breaking and micro-breaking wave signatures, to infer surface dissipation caused by the wave breaking. Handler et al.[21, 22, 23] simulated the thermal structures of flows beneath the free surface, calculated the statistics of the simulated flows and compared them to the IR measurement results. Bentamy and Katsaros[24, 25, 26, 27] obtained the surface wind shear and the latent heat flux from the satellite signals. Katsaros et al.[28] provided a detailed description on radiation sensing of the sea surface temperature. Garbe et al.[29, 30, 31] presented a methodology to measure the net heat flux from the IR image sequences by taking derivative of the surface temperature with respect to time.

On the topic of bulk parameterization and turbulence statistics beneath surface, Paulson and Simpson[32, 33, 34] did in-situ measurements of the vertical temperature profiles below the sea surface using buoys and compared their observation of the cool skin layer with Saunders' model[2] subject to various wind stress and heat flux. Smith, Prasad, et al.[35, 36, 37, 38] experimentally and Handler et al.[39, 40] and Leighton et al.[6] numerically did study of the horizontally averaged statistics of temperature and turbulent kinetic energy budget (e.g. production, dissipation and transport) for the flat surface convection flow with and without surface wind shear.

In the modeling of surface-bounded flow, Dommermoth[41, 42] studied the vortex-surface interaction. Smith et al.[43] explored the thermal signatures of a upwelling vortex through surface IR image. Osborne[44], Csanady[45] and Banerjee et al.[46] developed the surface straining/divergence model. Wells et al.[47] studied the straining flow effect to the cool skin layer through observing the upwelling vortical flow in experiments and applying the surface straining model to the experimental observation.

In the effort of relating the heat/gas transfer to the signatures of the surface temperature, Danckwerts[48] developed surface renewal theory in the study of gas absorption across liquid film. Liu and Businger[49, 50] modeled and measured the molecular sublayer in a way assuming that it undergoes cyclic growth and destruction, based on the model they calculated the temperature profile in the sublayer. Soloviev et al.[51] modeled the sea surface with the surface renewal theory, upon which he then parameterized the cool skin layer and the interfacial heat and gas transfer processes. Jessup et al.[52, 53] measured the skin temperature from IR signal and the vertical temperature profile beneath the surface with probe in a laboratory water tank, upon which he deduced the surface heat flux with gradient flux technique[54] and verified the surface renewal rate. Garbe et al.[55, 56] extensively evaluated the surface renewal model with IR imaging of the turbulence footprint and laboratory measurement of the water bulk temperature together with synthetic data of the surface temperature. Turney and Banerjee[57, 58, 59] compared the surface renewal model with the surface divergence model on predicting interfacial gas transfer.

1.2.2 Surfactant effects on ocean surface

It is demonstrated that surfactants ubiquitously exist in oceans and have certain effects on air-water interfacial dynamics. In the modeling of energy attenuation in the far ship wake, Milgram et al.[60, 61, 62] took the significant damping effects of surfactants in consideration. Alpers et al.[63] showed that viscoelastic surface film can introduce the Marangoni damping effect to certain high wavenumber resonance regions in spectral space, this so called 'energy sink' also affects long surface waves including longitudinal waves[64, 65, 66, 67] through nonlinear wave-wave interaction. Liu and Duncan[68, 69] showed in experiment that surfactants have strong effects on the shapes of the wave breakers that very likely play the role of boosting interfacial heat transfer in the forms of bubbles and sprays.

Among the efforts on modeling and simulation of the air-sea interface with surfac-

tants, Scriven[70] and Sarpkaya[7] defined and derived the general interfacial dynamics and boundary conditions of the air-water free surface. Shelley[71] discussed several computational models of surfactants. Phongikaroon et al.[72] investigated temperature effect to surface tension with presence of soluble and insoluble surfactants. Handler et al.[73] performed direct numerical simulations for free surface convection with surfactant and estimated its effect to interfacial passive scalar transport. Shen et al.[74] did simulation and theoretical study of aqueous thermal and viscous boundary layer with presence of surfactant. Kawagochi et al.[75] and Yu et al.[76, 77] did numerical simulations as well as experimental study on the turbulence statistics, heat transfer and drag reduction with presence of a surfactant. Ganesan and Tobiska[78, 79] provided a finite element numerical computation scheme to simulate free surface flow with surfactant. Xu et al.[80] employed level-set method, Lai et al.[81] employed immersed boundary method in computation of the interfacial flow with surfactant.

In the study of relationships between surfactant-vortex interaction and surfactant-gas flux, Tsai and Yue[82, 83, 84], Tryggvason et al.[85] studied the two-dimensional interaction between a surfactant contaminated surface and an upwelling vortical pair. Hirsa and Willmarth[86], Hirsa et al.[87] and Vogel et al.[88, 89] measured the concentration evolution of an insoluble surfactant monolayer interacting with a canonical vortex pair impinging the surface and compared the results to a theoretical model. Lopez and Chen[90] numerically investigated the viscoelastic free surface interaction with a swirling vortex. McKenna and McGillis[91, 92] measured the gas transfer across grid-stirred turbulence surface with and without surfactant, they also measured the surface divergence with PIV and calibrated its relationship with the surface gas flux supplied by Csanaday[45]. Khakpour, Shen and Yue[93] did simulations and investigation of passive scalar beneath the surfactant contaminated free surface.

1.2.3 Gas transfer and active thermography on turbulent buoyant convection

One of the objectives of the IR thermal signature and subsurface dynamics study is to unveil their connection to the interfacial gas exchange, in order to detect it remotely. As is stated, the aqueous boundary layer of momentum remains in all circumstances the threshold of the turbulent transfer processes across the interface including both heat and mass. Various models have been proposed to approach the aqueous boundary layer and the gas transfer process across it. Besides the aforementioned surface renewal model and surface straining model(see section 1.2.1), Fortescue and Pearson[94] proposed the large scale eddy model to describe gas absorption at sea surface and supported their model with experimental results. In addition, Lamont and Scott[95] proposed the small eddy model to describe mass transfer at the turbulent air-water interface. Liss and Slater[96] and Hasse[97] explored a molecular plus eddy diffusivity model to describe the interfacial gas transfer, they also asserted that capillary waves have positive effect to the interfacial gas transfer. Soloviev and Schlüssel[51, 98] firstly employed the surface renewal model to parameterize the cool skin layer as well as the gas transfer coefficient, then they also investigated the solar heating effects on damping convection instability and reducing surface renewal rate and gas transfer rate.

Experiments and simulations, besides modeling, are also done in the area of interfacial gas flux estimation. Liss[99] carried out experiments on water tank and wind-water tunnel to measure and compare the interfacial exchange constant of oxygen and carbon dioxide. Jähne et al.[100] carried out wind tunnel experiments to measure the gas transfer velocity subject to various wind speed. The results showed that for a smooth surface under wind speed below 3 m/s the gas transfer velocity is proportional to the wind speed, while for rough surface under higher wind speed gas transfer velocity is greatly enhanced by surface waves. Large and Pond[101] measured the latent and sensible heat

flux in ocean from ships, using Reynolds flux method and dissipation method. Ocampo et al.[102] measured the gas transfer rate in indoor laboratory with and without wind. Pan and Banerjee[103, 104], Nagaosa[105, 106] and Nagaosa and Handler[107] conducted direct numerical simulations for the turbulent open channel flows and investigated the interfacial gas transport of the simulated flows. Handler et al.[108] further simulated the passive scalar transport process in the turbulent open channel flow, followed by Kermani et al.[109] who did the similar simulation. De Angelis et al.[110, 111] simulated a deformable sheared air-water interface.

Among the efforts of modeling and detecting the interfacial heat/gas transfer at sea surface, Jähne et al.[9] proposed a promising strategy that comes from the inversion of the traditional measurement scheme. The strategy was based on the similarity of heat and gas transport in water, imposed a fixed heat flux at surface, and emulated the concentration evolution through inquiry of the surface temperature. Later on, Haußecker et al.[112] furnished and improved the controlled flux method through proposing and comparing three detailed techniques for its realization. Inspired by the controlled flux method, in this study we propose to further heat up the surface to actively suppress the free convection, to explore the surface temperature variation during the suppression, in attempt to acquire the information regarding heat/gas transfer velocity.

Active heating was first seen employed to postpone the onset of instability or to oppose the transition of turbulence, which is also referred to as stability control. Kral and Fasel[113] did 3-D numerical investigation on the active control of boundary layer transition, where surface heating was used to had successfully attenuated surface waves. Joslin et al.[114] demonstrated in experiment, computation and theoretical investigation that the two-dimensional TS waves can be superposed with two dimensional waves to reduce the amplitudes of the original waves based on the principle of wave cancellation. Choi, Moin and Kim[115] demonstrated that the blowing and suction at walls can reduce the skin fric-

tion drag by reducing the coherent structures. Specifically, for the active control of Benard convection, Tang and Bau[116] employed feedback control to have stabilized the otherwise unstable Benard flow in porous media heated from below, they also provided a linear stability analysis of the problem. Howle[117] accomplished the stability control of Benard convection using a heater at the bottom as the actuator. In particular, Marimbordes[118] did simulation and linear stability analysis of the active suppression of Benard convection flow between horizontal parallel plates cooled from both above and below, using a volumetric heat source.

Early theoretical study of the classic Rayleigh-Benard convection problem can be found in Kraichnan[119], Howard[120], Deardorff and Willis[121], where the flow was placed between two horizontal parallel plates that was heated from below or cooled from above. Foster[122, 123], Chandrasekhar[124], Drazin and Reid[125] contributed in the early development of the comprehensive linear stability analysis of the Rayleigh convection. Adrian et al.[126] provided the summary of the Rayleigh scale, conduction scale and convection scales for the Rayleigh convection flow. Other than those, Boeck and Thess[127] studied the surface tension driven Benard convection in theory and simulation. Kovalchuk et al.[128, 129] explored the surface tension induced spontaneous Marangoni instability. Siggia[130] discussed the dimensionless characteristics of high Ra convection. Grossman and Lohse[131] did the parameterization of the Rayleigh convection and discussed the relationships between Pr, Ra and Re.

1.3 Objectives

The development of remote sensing techniques such as IR imagery has been providing solid support to the non-destructive detection of sea surface temperature. Temporal and spatial evolution of the temperature at the air-water interface obtained through remote sensing can be used to extract various signals and hints to the subsurface turbulence activities. Our study is focused on the condition of smooth surface subject to low wind speed,

where the surface deformation is negligible and the free surface convection dominates. Under this circumstance, the cool skin layer is the key mechanism that connects the surface temperature signature to the subsurface turbulence. Moreover, it is known that for the free surface convection the ubiquitously existing surfactants have significant effects on the surface dynamics and the subsurface turbulence.

The first objective of the thesis is to explore, for the buoyancy driven free surface convection flow, the connection between the interfacial temperature signatures and the flow and thermal structures and statistics of the subsurface turbulence activities. More importantly, the study is aimed to quantitatively evaluate the surfactant effects on the features and statistics of the underlying flow. The study employs numerical simulations to resemble the convection flow. Proper modeling and computational implementation of the surfactant are required. The expectation is to better understand the interaction between the cool skin layer and surface free agents, and to better interpret the sea surface temperature signature subject to surfactant contamination.

The second objective of the thesis is to propose and verify a novel method to estimate the heat/gas transfer velocity at the free convection surface. The method is based on the controlled flux method yet with further active heating to suppress the free convection and to monitor the subsequent surface temperature evolution in attempt to infer the heat/gas transfer information. The study employs direct numerical simulations to resemble the free convection, the heating, and the cooling processes. Modeling, parameterization and realization of the artificial heating source are required. The effective suppression of the free convection is expected in the observation of the simulations. The connection between the surface heat/gas transfer velocity and the measured surface temperature is to be established in theory and to be certified in the simulations.

2. PROBLEM FORMULATION AND NUMERICAL STRATEGY

2.1 Physical modeling and simplification

2.1.1 Limiting case of negligible surface deformation

In terms of topology, the kinematic unit of the air-water interfacial deformation in the free surface turbulence with coherent structures is named 'blobs', to refer to the relatively separate volume of fluid that moves parallel or perpendicular, outside, inside or traversing to the surface, which is in analogy with the concept 'eddy' in the single phase turbulence flow. To quantify the blobs, the most energetic turbulent length scale, the overall velocity, and as a result the representative kinetic energy density per unit mass are denoted as L, q and $k = q^2/2$, respectively. Specifically, in the case with no breaking waves or discontinuities, L can be chosen to be comparable with either gravity surface wave length or capillary wave length, and q can be chosen to be the characteristic velocity of the blob relative to the surrounding flow.[132, 133]

At the sea surface, there are two major stabilizing forces to restore wind introduced surface waves and breakers, which are gravity force and surface tension force. Consider a typical water 'blob' that is about to emerge, sink or roll over at the surface, which has a characteristic length scale L and a velocity scale q. According to our definition, the blob possesses the specific energy density gL due to gravity and $q^2/2$ due to kinetic energy. The comparison of these two specific energy leads to the turbulent Froude number

$$Fr = \frac{q}{\sqrt{2gL}} \tag{2.1}$$

When the Froude number Fr is low ($q^2/2 \ll gL$), the gravity force dominates, and the surface area remains flat. When Fr is high ($q^2/2 \gg gL$), the turbulence kinetic energy is intense, and the surface is not restrained flat any more. Instead, excursion and breaking

wave happens. For $Fr \sim O(1)$, there are non-breaking gravity waves and wave-turbulence interactions.[132, 133]

Another restoring force, surface tension T is the contractive tendency of the liquid surface, raises from cohesion of similar molecules (see section 3.1.1). It has the dimension of force per unit length, or equivalently, energy per unit area. Division of surface tension by fluid density gives the specific surface energy $S = T/\rho$, therefore SL^2 is compatible to the kinetic energy of a specific volume of fluid with characteristic length scale L, which is $q^2L^3/2$. The ratio of specific kinetic energy density $q^2L^3/2$ versus specific surface tension energy SL^2 yields the turbulence Weber number

$$We = \frac{q^2 L}{S} \tag{2.2}$$

A low Weber number ($We \ll 1$) indicates that the disturbance is small relative to surface tension, while a high Weber number ($We \gg 1$) implies that surface tension is unable to hold the blob as a whole, and surface will break up into bubbles and sprays. Moderate $We \sim O(1)$ refers to the zone of wavy surface, typically capillary waves.[132, 133]

In actual problems, both gravity and surface tension are active coincidently, in other words, the surface behavior depends on both Fr and We. In this case, the velocity -length scale $q - L$ graph is sketched in Figure 2.1 to illustrate the parameter spaces corresponding to various surface conditions from quiescent surface to completely break-up surface. This plane is divided by lines $q = \sqrt{2Fr_c gL}$ and $q = \sqrt{2We_c S/L}$ defined by critical Froude and Weber numbers Fr_c and We_c, into 4 regions that are discussed below. The estimation of upper and low bounds of Fr_c and We_c is done in such a way: For the upper bound, consider a blob that transforms into a spherical drop that barely reaches the surface when it has lost any overall motion. Such a drop of radius R has potential energy $4/3\pi R^3 gR + 4\pi R^2 S$, assuming representative length to be $L = 2R$. Then, compare the potential energy to

kinetic energy $q^2L/2$ to get $q^2 \approx \pi gL/24 + \pi SL/2$. For the lower level bound, consider a linear downwelling feature bounded by two, convex upward quarter-circles of radius r. The potential energy per unit length of such a depression is $(5/3 - \pi/2)gr^3 + (\pi - 2)rS$, assuming depression has the distribution with respect to turbulent length scale of $L = 5r$, resulting the lower bound to be $q^2 \approx 1/125(5/3 - \pi/2)gL + (\pi - 2)S/5L$[132, 133].

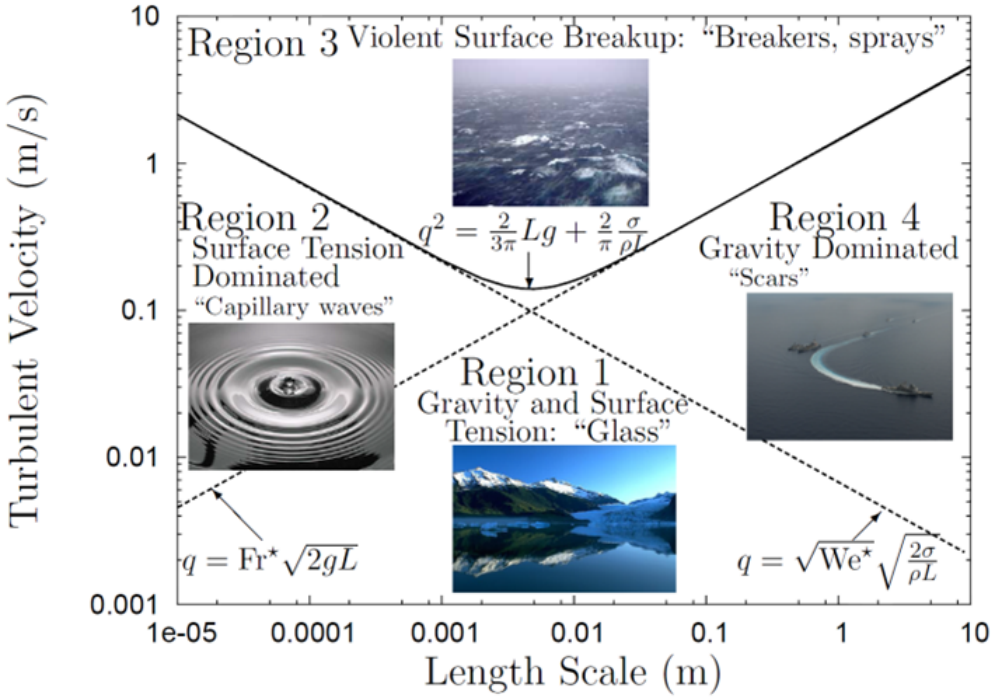

Figure 2.1: Surface deformation styles with respect to characteristic length scale and turbulent velocity.

Region 2 of Figure 2.1 goes with large Fr and small We, implying small scale deformation, i.e., in the order of 1 cm and less for water. In this scale of length, the gravity force is weak compared to the surface tension force. As the blob gets stronger, the gravity force fails to restrain the surface within flatness, yet still acts as reference to determine the

surface curvature, therefore the surface appears knobby. Nevertheless, the kinetic energy of the blob is under the critical value defined by Weber number, meaning surface tension is able to maintain surface continuity, therefore, the major deformation style in this region is capillary wave.

In region 3 of Figure 2.1, both Fr and We are greater than unity, indicating that the turbulence is strong and the kinetic energy of the blobs has overcome both the gravity force and the surface tension force, resulting in break up waves, bubbles, sprays, whitecaps, and spirals, to form a drastic transition zone of mixing of two phases.

Region 4 of Figure 2.1 is where $Fr \ll 1$ and $We \gg 1$, in other words, in this length scale, gravity is the main restoration force, and surface tension is relatively weak. Apparently, this is the commonly seen situation at geographical water surface such as river, sea, and ocean. In this case, though turbulence energy overwhelms the constraint of surface tension, it is insufficient to break through the gravity constraint, resulting in gravity waves, vortical dimples and scars (after vessels).

Region 1 is the case we focus on in the study, that is, when both Fr and We of the turbulence is smaller than unity. Here, the characteristic kinetic energy of the blobs is too weak to disturb the surface in either small scales where surface tension dominates or large scales where gravity dominates. As a result, there is little to no surface disturbance at all, the state corresponds to the rigid-lid free-slip boundary condition for the free surface turbulence. Practically, it is considered that the situation happens when the surface wind speed is below 3 m/s[21, 22]. It is worth noticing that even when the geometry of the surface is quite smooth, the subsurface turbulent eddies can still be active. In this case, the term 'blob' really refers to 'eddy', and the length and velocity scales of the 'blobs' become respectively the characteristic length and velocity of the most energetic eddy. The transient territory between region 1 and region 2 is recognized as ripple surface, and the transient territory between region 1 and region 4 is identified as wavy surface.

2.1.2 *Budget of ocean surface heat flux*

Generally, the air-sea surface heat exchange is modeled in energy budget as below[134]

$$N = S - L - H - E \tag{2.3}$$

where N is the net heat input to ocean, mostly from solar radiation, S is the net absorption of solar radiation, which depends on angle of incidence, cloud coverage, and other factors. L is the net loss from the ocean surface to atmosphere through longwave radiation, which is a function of sea surface temperature, atmospheric humidity, and cloudiness. H and E are respectively outgoing sensible and latent heat flux, which depend on wind speed, temperature and air side moisture. H and E are usually estimated from relationships

$$H = \rho c_p U C_H (T_s - T_a) \tag{2.4}$$

and

$$E = \rho L_E U C_E (Q_s - Q_a) \tag{2.5}$$

where ρ is density of air, c_p is isobaric specific heat of air, L_E is the specific latent heat due to vaporization. U is the mean wind speed at sea surface, T is the potential temperature, Q_a and Q_s are the specific humidity taken at a specified height and at the surface, respectively. C_H and C_E are empirically determined transfer coefficients.

Estimation of the individual terms may vary according to different climatology. Simpson and Paulson[135] have discussed measurement of solar radiation and infrared radiation of ocean surface. Bradley[134] concluded that the most important components are S and E, i.e., radiation absorption and latent heat flux. S ranges from 160 to 225 W/m^2, and E ranges from 60 to 120 W/m^2[134], both with uncertainty of around 80 W/m^2[136]. Also, his measurement result suggests that 'latent heat flux is an order of magnitude greater

than sensible heat flux' indicated in his Figure 9, while, in Large and Pond's measurement result[101] in their Figure 13, sensible heat flux is about 1/4 of latent heat flux at the same time.

Normally, for smooth surface in ocean, when the wind speed is lower than $3m/s$[21, 22], the solar radiation is absorbed in the detectable depth of $20m$[137] and the summation of latent and sensible heat flux is the premium source of outward heat flux. For the sake of simplicity, in our study, the interfacial heat transfer process of the smooth surface is modeled as a constant outgoing heat flux, typically around 200 W/m^2[138].

2.1.3 Boussinesq approximation

In ambient condition at sea surface, water is sufficiently treated as an incompressible fluid. Since in buoyancy driven flows, the exact governing equations are intractable[139], the simplest methodology to adopt buoyancy as the driving body force of the free convection is so called Boussinesq approximation[140]. In Boussinesq approximation, the fluid is considered incompressible, and fluid density is considered uniform everywhere, except for the gravitational body force term, where thermal expansion of fluid element is in consideration, and density difference is thus negatively proportional to temperature difference for water at ambient condition. Due to incompressibility assumption, the fluid undergoes isochoric process, and there is no pressure-volume work, or friction work anywhere, in other words, there is no work-heat coupling, the total mass, total heat and total momentum of the flow are conserved separately. Gravity force is allowed to produce work through buoyancy, the work transforms into kinetic energy, and is dissipated through viscosity. The incompressibility also eliminates sound waves by disengaging density variation, thus favorably simplifies the numerical process.

About Boussenesq approximation, although these equations are named after Boussinesq (see[139]), they seem to have been first used by Oberbeck[140]. The plausibility argument given by Chandrasekhar[124] is often referenced, Spiegel and Veronis[141] made

the first attempt to approach Boussinesq approximation at a detailed derivation in a dynamical situation, by considering a perfect gas of constant properties. Later assumptions, methods and mathematical works have been done along this way.[142].

2.2 System of governing equations, boundary and initial condition

2.2.1 Domain configuration, boundary condition and problem parameterization

In order to simulate the vast water body of ocean surface, the domain is better to be infinite on both vertical and horizontal directions, which is practically unattainable. Nevertheless, a sufficiently large cubic domain with limited dimensions is commonly acceptable, the actual size of which is empirically determined and is posteriorly amended during simulation. Generally, being sufficiently large means that, the vertical depth of the domain must be large enough to reach the bulk, that is the vertically homogeneous area certified by posterior flow statistics; the horizontal span of the domain must be capable of containing free evolution of multiple coherent flow structures. The illustration of the cubic domain is depicted in Figure 2.2.

For the cubic domain illustrated in Figure 2.2, the coordinate system is setup such that y axis is upwards, with its origin aligned at bottom of the domain, x and z axis are in horizontal directions, with their directions assigned in right-handed system. The domain is horizontally measured as L_x, L_z, and vertically measured as L_y, respectively. u, v, w are used to represent velocity components in corresponding directions, i.e.,

$$\vec{u}\,(x, y, z) = (u, v, w)\,(x, y, z) \tag{2.6}$$

$\theta\,(x, y, z)$ is used to represent temperature in the flow field.

To simulate the low Fr and low We situation at ocean surface specified in section 2.1.1, the top surface is modeled as non-deformed, implying the kinematic top boundary

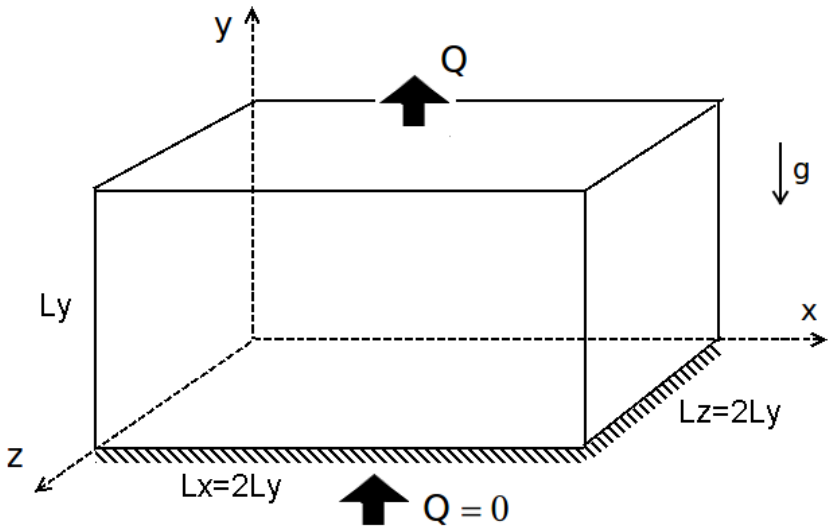

Figure 2.2: Schematic of the computational domain. An outgoing heat flux, Q, is imposed at the upper boundary while the bottom boundary remains thermally insulated. The gravitational acceleration, g, is directed downwards (negative y direction) as shown. The aspect ratio of the domain is 2:1:2 in the x, y and z direction respectively.

condition being rigid-lid, that translates to the Dirichlet boundary condition

$$v\left(y = L_y\right) = 0 \tag{2.7}$$

In addition, the dynamic top boundary condition at surface is specified through surface shear stress, which mathematically equals to the modeled driving wind shear stress due to continuity of shear stress. This translates to the Neumann boundary condition

$$\left.\frac{\partial u}{\partial y}\right|_{y=L_y} = \left.\frac{\partial w}{\partial y}\right|_{y=L_y} = \tau_0 \tag{2.8}$$

where τ_0 is the supposed shear stress at surface, which will be determined in the simulations of shear-driven turbulence and will be zero in the simulations of buoyancy driven free convection. To simulate the latent and sensible heat flux at surface (see section 2.1.2),

a constant outward temperature gradient (conduction boundary condition)

$$Q = -k\frac{\partial \theta}{\partial y} \tag{2.9}$$

is applied at top surface, since the very interface is considered pure conductive.

In cooperation with the effort of reducing domain size effect to simulated flow, the boundary conditions at the sideways are set periodic, i.e.,

$$u, v, w, \theta\,(x, y, z)\Big|_{x=0} = u, v, w, \theta\,(x, y, z)\Big|_{x=L_x} \quad u, v, w, \theta\,(x, y, z)\Big|_{z=0} = u, v, w, \theta\,(x, y, z)\Big|_{z=L_z} \tag{2.10}$$

In this traditional way, the inhomogeneity near side walls is avoided. In addition, the limited domain size in term of statistics can be compensated through multiple realizations of data. As long as multiple repeated flow structure is contained within the domain, it is considered reasonable approach of infinite spread at ocean surface. Moreover, for the same reason of reducing domain size effect, the bottom boundary condition is set to rigid-lid, shear-free and thermal insulated, i.e.,

$$v\,(y = 0) = 0 \frac{\partial u}{\partial y}\Big|_{y=0} = \frac{\partial w}{\partial y}\Big|_{y=0} = 0 \frac{\partial \theta}{\partial y} = 0 \tag{2.11}$$

The comprehensive parameter space of the problem is given in Table 2.1 .

Table 2.1: Parameter groups of the free convection problem

ν	α	k	ρc_p	$g\beta$	Q	L_y

where ν is the kinematic viscosity of water, α is the thermal diffusivity of water, k is the

thermal conductivity of water, ρ is the density of water, c_p is the isobaric heat capacity of water, g is the gravitational acceleration, Q is the constant heat flux at surface, L_y is the domain depth. In buoyancy driven flow, the guaranteed constant density in Boussinesq approximation makes $g\beta$, the product of thermal expansion coefficient and gravity acceleration act as a whole in the buoyancy body force. For the same reason, density and heat capacity show up together, because density alone is not effective anywhere else except for yielding heat capacity per unit volume together with c_p, heat capacity per unit mass.

The physical quantities involved are time, length, temperature and energy, while the above group in Table 2.1 has 7 elements. Therefore, there are 3 independent dimensionless groups to specify the problem. Depending on the various choices of repeating variables, the group members may boils down to Reynolds number Re, Rayleigh number Ra, Prandtl number Pr or Nusselt number Nu, defined respectively as below:

$$Re = \frac{uL_y}{\nu} \tag{2.12}$$

$$Ra = \frac{g\beta Q L_y^4}{\alpha \nu k} \tag{2.13}$$

$$Pr = \frac{\nu}{\alpha} \tag{2.14}$$

$$Nu = \frac{k}{\frac{Q}{\theta} L_y} \tag{2.15}$$

In the following section will be given an advanced discussion about the derivation of these numbers, in concert to scaling of governing equations.

2.2.2 Governing equations of mass, momentum, and energy conservation

The mass conservation is presented as that the mass inflow equals the mass outflow of an arbitrary control volume. In differential form it is written as

$$\frac{D\rho}{Dt} = 0 \tag{2.16}$$

or after coordinate transformation to Eulerian notation:

$$\frac{\partial \rho}{\partial t} + \nabla \cdot (\rho \vec{u}) = 0 \tag{2.17}$$

Combined with general incompressibility, i.e., temporal and spatial constant density from Boussinesq approximation, Equation (2.17) can be reduced to

$$\nabla \cdot \vec{u} = 0 \tag{2.18}$$

Momentum conservation is presented as that for a fluid particle, the time rate of change of momentum is equal to the applied surface force plus body force (Newton's second Law).

$$\frac{D(\rho \vec{u})}{Dt} = \nabla \cdot \Gamma + \vec{f} \tag{2.19}$$

where Γ is the stress tensor representing overall surface force applied to the particle, for Newtonian fluid, $\Gamma = \mathbb{F}[\nabla \vec{u}] = f_1 \mathbf{I} + f_2 \mathbf{D}$ is linearly related to deformation tensor $\mathbf{D}$. $\vec{f}$ represents overall body force per unit volume applied to the particle.

With density being constant, the left hand side of Equation (2.19) can be written in substantive derivative as

$$\rho \frac{\partial \vec{u}}{\partial t} + \rho(\vec{u} \cdot \nabla)\vec{u}$$

The right hand side can be divided into two parts, i.e., isotropic and non-isotropic part, as

$$\Gamma = (-p + \lambda \nabla \cdot \vec{u})\mathbf{I} + 2\mu \mathbf{D} = -p\mathbf{I} + \mathbf{T}$$

where p is the thermal dynamic pressure rises from isotropic part of stress tensor, $\mathbf{T}$ is the deviatoric tensor, that comes from anisotropic part of stress tensor. For incompressible fluid, $\lambda \nabla \cdot \vec{u} = 0$, therefore, rearranging Equation (2.19) including writing out viscous

terms yields

$$\frac{\partial \vec{u}}{\partial t} + (\vec{u} \cdot \nabla)\vec{u} = -\frac{1}{\rho}\nabla p + \nu \nabla^2 \vec{u} + \frac{1}{\rho}\vec{f} \tag{2.20}$$

The buoyancy force is implemented by varying gravity body force according to the density variation induced by thermal expansion, as below:

$$\vec{f} = -\rho g(1 - \beta\theta)\hat{e}_y \tag{2.21}$$

Energy conservation comes from advection-diffusion heat equation, written as

$$\frac{\partial \theta}{\partial t} + (\vec{u} \cdot \nabla)\theta = \alpha \nabla^2 \theta + s \tag{2.22}$$

where s is the artificial volumetric heat source reserved for numerical manipulation. In the boundary condition we have configured a constant outgoing heat flux Q, however, instead of infinite depth of real sea surface, we have a limited depth for the simulation domain, therefore, a temperature drift is introduced by the net energy loss caused by heat flux boundary Q. To avoid that and to maintain consistency of temperature in number for convenience, a volumetric, predetermined compensation heat source is applied through s, the value of which is configured to exactly reimburse the energy loss through surface heat flux, i.e.,

$$s_c = \frac{Q}{\rho c_p L_y} \tag{2.23}$$

To sum up, the dimensional form of conservation equations of mass, momentum, and energy goes

$$\nabla \cdot \vec{u} = 0 \tag{2.24}$$

$$\frac{\partial \vec{u}}{\partial t} = \vec{u} \times \vec{\Omega} - \nabla\Pi - \nu \nabla^2 \vec{u} + \beta g \theta \hat{e}_y \tag{2.25}$$

$$\frac{\partial \theta}{\partial t} + (\vec{u} \cdot \nabla)\theta = \alpha \nabla^2 \theta + \frac{Q}{\rho c_p L_y} \tag{2.26}$$

where $\Pi = p/\rho + \vec{u} \cdot \vec{u}/2$ is the modified pressure.

2.2.3 Scaling and non-dimensional governing equations

There are three standard scaling schemes for turbulent convection problem[6, 126]. The classic one to scale Rayleigh problem is firstly proposed in Lord Rayleigh's analysis[126], the variable set of which is composed of β , g, α, ν, z^*, and ΔT, where z^* represents characteristic depth of the convection layer, or the depth of the domain in this particular case of study, and ΔT is the temperature drop across the domain. Dimensionless grouping of these variables lead to z/z^*, $Nu = Qz^*/\alpha\Delta T$, $Ra = \beta g z^{*3}\Delta T/\alpha\nu$ and $Pr = \nu/\alpha$. This Rayleigh scale is originally from the general convection problem description and instability analysis, and is correct in the sense of dimensional analysis. It is not, however, the most convenient scales for turbulence analysis and discussion, suggested by the fact that turbulent Rayleigh number is always greater than the order of 10^6.

Tow alternatives of scaling have been proposed by Townsend[143] and Deardorff[144], which are referred to as 'conduction scale' and 'convection scale', or 'inner scale' and 'outer scale', respectively. Townsend's scale pertains to the conduction layer in the vicinity of the boundary, where vertical turbulent motions are suppressed by the wall, and heat is transferred primarily by conduction. The repeated variables are chosen to be α, ν, βg and Q, the total depth of the domain is reasonably excluded since conduction only dominate in a very thin layer that doesn't extend to the entire domain. In substitution, a new length scale was proposed based on grouping of heat flux and properties of water, the scale turned out to work very well. Inner scaling is essentially correlated to the surface strain model derivation[6, 45].

In the bulk far away from the boundary, heat transfer is predominantly in the form of advection through eddies, circulation and chaotic motion, while molecular diffusion of

Table 2.2: Scales of the free convection problem

	Length	Velocity	Temperature
Rayleigh	L_y	$\frac{\alpha}{L_y}$	$\frac{QL_y}{k}$
Townsend (inner, conduction layer)	$(\frac{\beta g Q}{\rho c_p \alpha^3})^{-\frac{1}{4}}$	$(\frac{\beta g Q \alpha}{\rho c_p})^{\frac{1}{4}}$	$(\frac{Q}{k})^{\frac{3}{4}}(\frac{\beta g}{\alpha^2})^{-\frac{1}{4}}$
Deardorff (outer, convection layer)	L_y	$(\frac{\beta g Q L_y}{\rho c_p})^{\frac{1}{3}}$	$\frac{Q}{\rho c_p}(\frac{\beta g Q L_y}{\rho c_p})^{-\frac{1}{3}}$
Scales we use	$\sqrt{2}(\frac{\beta g Q}{\rho c_p \nu \alpha^2})^{-\frac{1}{4}}$	$(\frac{\beta g Q L_{sc}}{\rho c_p})^{\frac{1}{3}}$	$\sqrt{\frac{\pi}{2}}(\frac{Q}{k})^{\frac{3}{4}}(\frac{\beta g}{\alpha \nu})^{-\frac{1}{4}}$

heat is relatively weak compared to large scale advection in the order of domain depth. For large scale motion of turbulent transport of heat and momentum, Deardorff[144] has proposed convection scales, where the convection layer depth becomes important again, the relevant variables are βg, Q , z^*, length, velocity and temperature scales are composed of these relevant scales. The essential difference between convection scale and Rayleigh scale, which is also the shortcoming of Rayleigh scale, is that the velocity of Rayleigh scale is α/z^*, which is the thermal diffusivity, a molecular level property, divided by layer depth, a macro scale. Deardorff convection scale made adjustment on it by replacing it with composed velocity scale from repeat variables, to make it in the order of convection scale. Outer scaling is valid in the bulk flow where viscosity plays relatively less important role.

A complete list for these three scales, and the scales used in the study here are presented in Table 2.2.

In Table 2.2, after rearrangement, we have

$$L_{sc} = \sqrt{2}(\frac{\beta g Q}{\alpha \nu k})^{-\frac{1}{4}}$$

$$U_{sc} = 2^{\frac{1}{6}} Pr^{\frac{1}{3}} \frac{\alpha}{L_{sc}}$$

$$t_{sc} = 2^{\frac{1}{3}} Pr^{-\frac{1}{3}} \frac{L_{sc}^2}{\alpha}$$

and

$$T_{sc} = \sqrt{\frac{\pi}{2}} \frac{Q}{k} L_{sc}$$

Similar representations can be seen in[126]. Here, it is seen that, the modified Townsend scale, in the last row of Table 2.2, is in the form of Deardorff scale, except the base length scale is substituted by the conduction characteristic length from Townsend scale. This is an evidence that Deardorff scale will reduce to Townsend scale, if the conduction layer alone is of consideration. Essentially, all the scales are interchangeable, the matter of fact is to choose the one with proper magnitude to scale the problem and the results. In our study we use Rayleigh scale to non-dimensionalize the governing equations and boundary conditions, since it is more convenient and conventional. In the result and discussion section, we switch to the modified Townsend scale as is presented in the last row of Table 2.2, supposedly for subsurface turbulence analysis and calculation.

Using Rayleigh scales in Table 2.2, the non-dimensionalization of Equations (2.24) through (2.26) yields

$$\nabla \cdot \vec{u} = 0 \tag{2.27}$$

$$\frac{\partial \vec{u}}{\partial t} = \vec{u} \times \vec{\Omega} - \nabla \Pi - \frac{1}{Re} \nabla^2 \vec{u} + Ra_q \cdot Pr \theta \hat{e}_y \tag{2.28}$$

$$\frac{\partial \theta}{\partial t} + (\vec{u} \cdot \nabla)\theta = \nabla^2 \theta + 1 \tag{2.29}$$

where $Ra_q = \beta g Q L_y^4 / \alpha \nu k$ is the flux based Rayleigh number, $Re = U_{sc} L_{sc} / \nu = \alpha / \nu$ is Reynolds number, $Pr = \nu / \alpha = 1/Re$ is the Prandtl number.

2.3 Discretization and numerical schemes

2.3.1 Weighted residual methods

When it comes to numerical discretization of partial differential equations (PDE), the overall strategy is to interpolate the otherwise continuous solution space into a solution space with limited dimension, with the concept of 'approaching infinity with finite'. In practice, the most convenient way to be taken by numerical methods is to approximate the unknown solution function $u(x)$ with a truncated series expansion under analytical basis $\phi_j(x)$, as

$$u(x) \approx u_N(x) = \sum_{j=0}^{N} a_j \phi_j(x) \tag{2.30}$$

where a_n are unknown coefficients, and $\phi_j(x)$ are known analytical basis. By definition, finite volume methods and finite element methods choose small, usually linear, second or third order basis functions, while spectral method chooses continuous basis function to yield analytical representation of solution in entire computation domain within limited spectral range.

Consider the problem

$$\mathcal{L} u(x) = f(x) \tag{2.31}$$

where $\mathcal{L}$ is a differential operator. Approaching the exact solution $u(x)$ with approximated solution $u_N(x)$ yields the residual

$$\mathcal{R}(x; a) = u_N(x) - f(x) \tag{2.32}$$

Apparently, the ultimate objective is to minimize the overall residual, which is defined variously depending on the particular problem configuration, choice of basis and distribution

of solution. Mostly often, the overall residual is calculated as the weighted summation over the domain, with assistance of the designated weight function on the same domain. Such numerical discretization schemes are classified as weighted residual methods (WRM).

In WRM, the coefficients a_j are determined by requiring that the summation or the integral of the weighted residual over the computational domain approaches zero, i.e.,

$$\int W_j(x) R_j\{x; a_j\} dx = 0 \tag{2.33}$$

by letting $n = 1..N$, a series of equations for a_j is generated. Different choice of weighted function $W_n(x)$ gives rise to different methods, including[145]:

(1) subdomain method: the domain is divided up to m subdomains D_m which may overlap each other, where

$$W_m(x) = \begin{cases} 1 : x \in D_m \\ 0 : otherwise \end{cases} \tag{2.34}$$

Since finite element method and finite volume method are defined with choices of elements as basis, it coincides with choice of the subdomain and weight function. For finite volume method, Equation (2.17) naturally provides appropriate framework for enforcing conservation at the discretized equation level, this is a particular advantage in obtaining accurate solution with finite volume method.

(2) collocation method:

$$W_m(x) = \delta(x - x_m) \tag{2.35}$$

Collocation method means the residual is exactly zero at all collocation points, regardless of the residual away from those points. Finite difference methods are typically collocation methods.

(3) least-square method:

$$W_m(x) = \frac{\partial R_m \{x; a_m\}}{\partial a_m} \tag{2.36}$$

Substitute Equation (2.36) to Equation (2.33), it goes $\int R_m^2(x)dx = 0$ meaning that the least of the integral of squared residual is approached under this scheme.

(4) Galerkin method:

$$W_m(x) = \phi_m(x) \tag{2.37}$$

i.e., the weight functions are chosen from the same basis functions. Similarly, substitute Equation (2.37) to (2.33), one can see that it means the residual is orthogonal to every member of the basis set. Consequently, for $N \to \infty$, the approximation $u_N(x)$will converge to exact solution $u(x)$.

In our spectral code to be discussed later, the collocation method is employed during the transformation of initial condition from physical space to spectral space, meaning that initial condition is supplied on discretized mesh grids that have identical resolution with the solver. The subsequent time step advance of the conservation equations is composed of two parts, the linear part and the non-linear (advection) part. The linear part is evaluated in pure spectral space, the non-linear part is transformed back to physical space, where resolution is expanded for the sake of de-aliasing. After manipulation(multiplication), the result is transformed back to spectral space to combine with the result of the linear part, the transformation employs collocation scheme again, and the extra spectral section higher than original capacity of resolution, which is produced by multiplication, is discarded.

2.3.2 Spectral method versus FEM, FDM

As is stated above, in the case where non-linear terms are involved, the evaluation of products of approximate solution in spectral space is very time-consuming, therefore the

collocation scheme is employed in nodal time advance of non-linear terms, this approach is usually referred to as pseudo-spectral method. Unlike finite element method (FEM) or finite volume method (FVM), spectral method(SM) is a global method, meaning the basis is chosen to be significant through the whole computational domain, instead of the local subdivision. Also, in contrast to Galerkin methods, SM employs orthogonal functions for approximations and weight functions[145]. Commonly, Fourier series, Chebyshev polynomial or Legendre polynomial are the most popular orthogonal functions of preference. Use of orthogonal polynomials simplifies the structure of equations, in addition, if boundary condition is appropriate, SM can generate very high accuracy solution with relatively few terms and computation resources if the exact solution is smooth[146]. Comparably, there are three preliminary strategies for a FEM algorithm to increase resolution, they are h-refinement, r-refinement, and p-refinement. For h-refinement, grid resolution is uniformly increased over the whole domain, as h is the common symbol to refer average grid size. For r-refinement, only local places with possible steep gradient are refined. Being different from the above two, the p-refinement is to raise degree of polynomials in each subdomain[147].

FEM and FVM have their own advantages compared to SM. Firstly, the matrix they generated from discretization of PDE into algebra equations are sparse, because corresponding to each given sub-domain only a few terms are non-zero. In comparison, original SM usually generates full rank coefficient matrices which are nearly impossible to numerically invert to yield the solution. Solution to this difficulty of SM method is to utilize the trigonometric mesh (mesh points assigned at $cos(n\zeta), n\zeta = 0, ..., \pi$) in one direction with basis function being Chebyshev polynomial, which will yield tridiagonal coefficient matrices which is easy to invert, and solve the Chebyshev direction firstly. Moreover, this trigonometric mesh point assignment naturally increases grid resolution near boundaries, which optimizes boundary layer flow accuracy and is particularly beneficial to our study.

Certainly, the solution of SM is not universal, but rather applicable within the particular configuration. Indeed, in multi-dimensional problems, FEM and FVM are capable of working with various kinds of mesh grids including triangles and tetrahedra, thus providing great adaptivity to arbitrary geometries, as SM can only work on limited types of geometry, which includes flow between two plates.

Nevertheless, spectral method has its merit in the following computational aspects[148]:

Convergence: If the solution is highly differentiable, SM with proper design converges faster than any finite power modes, while FDM and FEM yield finite-order rates of convergence. This indicates that SM achieves high accuracy with relatively easy expansion of resolution.

Efficiency: Due to the employment of FFT(Fast Fourier Transfer), SM advances FDM or FEM by a factor of 2-5 fewer degrees of freedom in each dimension for comparable accuracy. Implicit one-step solver in SM compared to iterative solver in FDM or FEM is another quite considerable factor of efficiency.

Boundary Condition: Since SM deals with continuous physical space, the boundary condition imposed on the governing PDE, regardless of its type being Dirichlet or Neumann, is precisely the boundary condition adopted in the computation without theoretical approximation or systematic bias. In contrast, FDM or FEM requires additional adjustment of boundary conditions, which most often introduces additional complication and inaccuracy.

Discontinuity: Although SM is not commonly employed to handle problems with discontinuity, spectral methods do have a good property on localizing errors than FDM or FEM, i.e., requires less local dissipation in order to handle discontinuities.

2.3.3 Hybrid numerical methods: spectral element, DES

Spectral element method is the hybrid descendant of spectral method and finite element method, which performs well especially when the geometry is fairly smooth and regular.

On one side, the domain is divided into subdomains, just like finite element method, in order to adapt to complex geometry and make use of sparse coefficient matrices; on the other side, for each subdomain, the degree of basis function is relatively high in order to gain high accuracy, in the manner of spectral method. Typical polynomial degree for basis function in spectral element method is 6 to 8, compared to 2 to 3 in finite element method and sinusoidal functions in spectral method. Besides, spectral element code is always written in such a way so that the degree of polynomials for basis functions is adjustable[147]. In development of spectral element code, studies have found that regular finite element techniques and theories become increasingly ill-conditioned[147] in higher order of sixth or more, the practical solution is to employ techniques of spectral method. Meanwhile, in dealing with matching spectral expansions across subdomain walls, finite element theories are found to be helpful[147].

DES was originally invented to deal with high Reynolds number situations and highly separated flows in fields such as aerospace engineering and atmospheric study. It is basically the combination of LES and RANS[149], in which a modification of RANS model is carried out that switches to LES calculation in regions where turbulent length scale challenges lower boundary of grid size. In relatively less intense regions of turbulence, RANS or URANS applies. Such an adaptive scheme considerably cuts down the cost of computation. The drawback is that the grid generation is rather complicated due to modal switch between RANS and LES, compared to either single one[150, 151].

2.4 Algorithm and implementation

The algorithm follows the exact realization of Kim, Moin and Moser[152], which is particularly suitable for our study in the following aspects:

(1) The cubic geometry of simulation domain (free from geometrical constraints, in favor of global methods);

(2) Horizontal homogeneity and periodic boundary condition at side ways (compatible

to Fourier series representation in horizontal direction);

(3) Vertical inhomogeneity and emphasis of vicinity of top surface (finer grid resolution beneath surface for trigonometric Chebyshev polynomial);

(4) Flow incompressibility (convenience of pre-conditioning mathematical manipulation).

The detailed procedure of the algorithm is stated below. Through tensorial manipulation, the governing equations for the incompressible flow (2.27) through (2.29) are written in the following form[152]:

$$\frac{\partial u_i}{\partial t} = -\frac{\partial p}{\partial x_i} + H_i + \frac{1}{Re}\nabla^2 u_i \tag{2.38}$$

$$\frac{\partial u_i}{\partial x_i} = 0 \tag{2.39}$$

Here, all variables are non-dimensionalized. H_i includes the convective terms and the mean pressure gradient. With assistance of (2.39), (2.38) can be reduced to yield a fourth order equation for v, and a second order equation for the normal component of vorticity g as follows :

$$\frac{\partial}{\partial t}\nabla^2 v = h_v + \frac{1}{Re}\nabla^4 v \tag{2.40}$$

$$\frac{\partial g}{\partial t} = h_g + \frac{1}{Re}\nabla^2 g \tag{2.41}$$

$$f + \frac{\partial v}{\partial y} = 0 \tag{2.42}$$

where

$$f = \frac{\partial u}{\partial x} + \frac{\partial w}{\partial z} \tag{2.43}$$

$$g = \frac{\partial u}{\partial z} - \frac{\partial w}{\partial x} \tag{2.44}$$

$$h_v = -\frac{\partial}{\partial y}\left(\frac{\partial H_1}{\partial x} + \frac{\partial H_3}{\partial z}\right) + \left(\frac{\partial^2}{\partial x^2} + \frac{\partial^2}{\partial z^2}\right) H_2 \tag{2.45}$$

$$h_g = \frac{\partial H_1}{\partial z} - \frac{\partial H_3}{\partial x} \tag{2.46}$$

Then, the time derivatives of Equation (2.40) through Equation (2.42) are evaluated in Fourier series in horizontal directions and Chebyshev polynomial expansion in the vertical direction. The time advancement is carried out by semi-implicit scheme, that is Crank-Nicolson for viscous terms and Adams-Bashforth for nonlinear terms. Equation (2.41) hence reduces to

$$\left.\begin{aligned} \left(1 - \frac{\Delta t}{2Re}\nabla^2\right) g^{n+1} &= \frac{\Delta t}{2}(3h_g^n - h_g^{n-1}) + (1 + \frac{\Delta t}{2Re}\nabla^2) g^n \\ g\,(\pm 1) &= 0 \end{aligned}\right\} \tag{2.47}$$

Equation (2.47) is solved by the Chebyshev-tau method for each wavenumber after it is Fourier transformed in the horizontal directions, it then reduces to a tridiagonal system with one full row after decoupling the even and odd modes of the Chebyshev coefficients[152].

The fourth order equation (2.40) can be solved most efficiently by splitting it into two second order equations as follows

$$\left.\begin{aligned} \left(1 - \frac{\Delta t}{2Re}\nabla^2\right) \phi^{n+1} &= \frac{\Delta t}{2}\left(3h_v^n - h_v^{n-1}\right) + \left(1 + \frac{\Delta t}{2Re}\nabla^2\right) \phi^n \\ \nabla^2 v^{n+1} &= \phi^{n+1} \\ v^{n+1}\,(\pm 1) = \frac{\partial v^{n+1}}{\partial y}\,(\pm 1) &= 0 \end{aligned}\right\} \tag{2.48}$$

This coupled system is solved by the Chebyshev method, in which the four boundary

conditions are satisfied as follows. Let

$$v^{n+1} = v_p^{n+1} + c_1 v_1^{n+1} + c_2 v_2^{n+1} \tag{2.49}$$

where the particular solution v_p^{n+1} and the two homogeneous solutions v_1^{n+1} and v_2^{n+1} satisfy

$$\left.\begin{aligned} \left(1 - \frac{\Delta t}{2Re}\nabla^2\right)\phi_p^{n+1} &= \frac{\Delta t}{2}\left(3h_v^n - h_v^{n-1}\right) + \left(1 + \frac{\Delta t}{2Re}\nabla^2\right)\phi^n \\ \nabla^2 v_p^{n+1} &= \phi_p^{n+1} \\ \phi_p^{n+1}(\pm 1) &= 0 \\ v_p^{n+1}(\pm 1) &= 0 \end{aligned}\right\} \tag{2.50}$$

$$\left.\begin{aligned} (1 - \frac{\Delta t}{2Re}\nabla^2)\phi_1^{n+1} &= 0 \\ \nabla^2 v_1^{n+1} &= \phi_1^{n+1} \\ \phi_1^{n+1}(1) = 0, \quad \phi_1^{n+1}(-1) &= 1 \\ v_1^{n+1}(\pm 1) &= 0 \end{aligned}\right\} \tag{2.51}$$

$$\left.\begin{aligned} (1 - \frac{\Delta t}{2Re}\nabla^2)\phi_2^{n+1} &= 0 \\ \nabla^2 v_2^{n+1} &= \phi_2^{n+1} \\ \phi_2^{n+1}(1) = 1, \quad \phi_2^{n+1}(-1) &= 0 \\ v_2^{n+1}(\pm 1) &= 0 \end{aligned}\right\} \tag{2.52}$$

Equation (2.50) through (2.52) are solved simultaneously after Fourier transformed in the horizontal directions by eliminating the same banded matrix with three different right hand sides. The constants c_1 and c_2 are then chosen such that

$$\frac{\partial v^{n+1}}{\partial y}(\pm 1) = 0 \tag{2.53}$$

Once the normal velocity and vorticity are computed, the streamwise velocity u and spanwise velocity w are then obtained from the definitions of f and g through solving (2.43) and (2.44). Computation of pressure is not required for time advancement, but is required for turbulence statistics involving pressure. There are two ways to compute pressure, either from normal momentum equation with wall pressure values determined from combination of horizontal momentum equations, or from equation of f with pressure corresponding to zero wave numbers.

The non-linear terms in (2.38) are computed in rotational form to preserve the conservation property of mass, energy and circulation numerically. In addition, the number of collocation points is expanded by a factor of $3/2$ before transforming into physical space to avoid aliasing errors involved in computing the nonlinear terms pseudo-spectrally.

Since the code implicitly conserves mass, momentum, and energy, as long as the computation is stable, the results automatically fit in these conservation laws, therefore the results are unquestionably consistent with physics. Since the time advance is implicit and free of iteration, there is no convergence issue. The code employs CFL number $u\Delta t/\Delta x$ to measure, monitor and track stability, once the CFL number is above 0.2 0.3, it is considered that computation is vulnerable to errors and development of computational instability, and the time step needs to decrease. When CFL number is kept below 0.2, the numerical dissipation is in charge of canceling the development of unstable modes (which also introduces numerical error to the simulation).

The problems to be simulated are setup in a way that the momentum and thermal energy input and output are always balanced after the flow reaches the anticipated steady state. Therefore, it is unnecessary to take special care of the initial condition setup. Indeed, all simulations start from the initial condition of zero velocity and uniform temperature, with very small perturbation to trigger flow instability. Nevertheless, it is worth noticing that, at the very beginning of the simulation, the transient dynamic response of the flow

field from impulsive stimulation introduced by a sudden modification of the boundary condition is certainly interesting, as will be discussed in section 3.3.7.

The algorithm is implemented in *Fortran 77*, and compiled with *Intel Fortran* in real*8 float point accuracy. The calculation of the first, second order derivatives are modularized as subroutines and subfunctions to raise programming efficiency. Simulations were carried out on *Cray CX1* supercomputer with 24 cores in total on 3 independent nodes, each bears a Linux OS, interconnected with *InfiniBand* of 2 Gbit/s data transfer speed. The typical computation time is two days for a single core for 20,000 time steps in the SM code. Besides the main solver, other assistive pre/post processing utilities in *Matlab* and *Fortran* are also developed for the purpose of data processing, initial condition generation, statistics calculation and flow & thermal field visualization.

3. SIMULATION OF TURBULENT FREE CONVECTION WITH PRESENCE OF SURFACTANT*

3.1 Modeling of surfactant dynamics : theory, experiments and simulations

3.1.1 Surface tension balance at curved interface

Surface tension acts only at the free surface, consequently, it does not appear in the Navier-Stokes equations, but rather enters the problem through the boundary conditions. The origin of surface tension is at molecular level, where mutual attraction is larger than mutual repulsion. This is simply because molecules at surface are engaged in less bond than the ones in the bulk, thus is energetically unstable and less restrained, as a result, the mean distance between molecules at surface are larger than the one in bulk. From thermal dynamic point of view, creation of new surface, including curvature of existing surface, is energetically costly because of breaking or stretching of molecular bonds, and a fluid system always tends to minimize surface areas.[153]

Assuming E is the total molecular bond energy per molecule, then it reduces to $E/2$ for a molecule at flat surface. Surface tension is the direct measurement of such an energy loss per unit surface area. If the characteristic molecular dimension is R, then corresponding surface tension will be $\sigma \approx E/(2R^2)$. Previous studies have shown that surface tension increases along with increasing molecular bond and decreasing molecular size. Typical surface tension of water is $\sigma \approx 70 dynes/cm$, while the number for oil is $\sigma \approx 20 dynes/cm$, liquid mercury being $\sigma \approx 500 dynes/cm$[153]. As is stated, the units of surface tension is energy per area, or equivalently, force per length. Compared to the units of pressure (force per area), it is convenient to perceive that surface tension is the '2-D analogy of pressure'

* Data, results and discussion in sections 3.2, 3.3 are reprinted with permission from "Direct numerical simulation of turbulent free convection in the presence of a surfactant" by Qi Zhang, Robert A. Handler, Sam T. Fredriksson (2013). *International Journal of Heat and Mass Transfer*, 61, 82-93, Copyright 2013 by Elsevier.

within the surface, supported by the fact that surface tension work is done through surface contraction, that can be thought of as the perpendicular displacement of a line element at surface, while pressure work is done through bodily contraction, that can be similarly thought of as the perpendicular displacement of an surface element in a volume[153].

Derivation of normal and tangential stress boundary conditions at a fluid-fluid interface is as below. Think about an curved interface S bounded by a close contour element C, as in Figure 3.1, there is hence a surface tension σ in the normal direction s at every point along C that tends to stretch the surface S. Force balance on the volume element V enclosed by the interfacial surface S defined by C gives:[153]

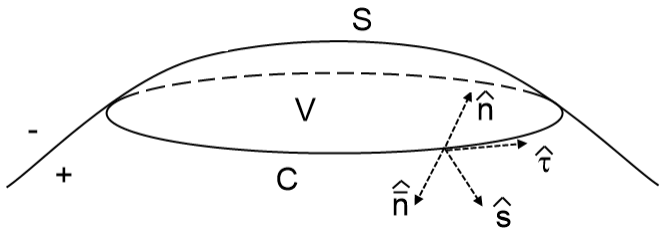

Figure 3.1: Element for interfacial stress balance analysis. Surface S is a surface element between two different fluids, surrounded by contour C that is also in the surface S. Upper fluid is marked with (-), Lower fluid is marked with (+).

$$\underbrace{\int_V \rho \frac{D\vec{u}}{Dt} dV}_{(1)} = \underbrace{\int_V \vec{f} dV}_{(2)} + \underbrace{\int_S \left[\vec{t}(\hat{n}) + \vec{t}(\hat{\bar{n}})\right] dS}_{(3)} + \underbrace{\int_C \sigma \hat{s} dl}_{(4)} \tag{3.1}$$

Here l indicates arclength, dl is the length increment along the curve C. $\vec{t}(\hat{n}) = \hat{n} \cdot \mathbf{T}$ is the stress vector, the force per area exerted by the lower (+) fluid on the interface. The stress tensor is defined in terms of the local fluid pressure and velocity field as $\mathbf{T} = -p\mathbf{I} + \mu\left[\nabla\vec{u} + (\nabla\vec{u})^T\right]$ for the lower (+) fluid side, and $\bar{\mathbf{T}} = -\bar{p}\mathbf{I} + \bar{\mu}\left[\nabla\vec{\bar{u}} + (\nabla\vec{\bar{u}})^T\right]$ for the

upper (-) fluid side. Similarly, the stress exerted on the interface by the upper (-) fluid is $\vec{t}(\hat{\bar{n}}) = \hat{\bar{n}} \cdot \bar{\mathbf{T}}$. Physically, the interpretation of the terms in Equation (3.1) are respectively:

(1) inertial force associated with acceleration of fluid within V;

(2) body forces acting on fluid within V;

(3) hydrodynamic force exerted at interface by fluid +,-;

(4) surface tension force exerted along perimeter C.

In the limiting case of infinitesimal volume, acceleration (1) and body forces (2) scales one dimension higher than surface forces (3)(4), therefore we have

$$\int_S \left[\vec{t}(\hat{n}) + \vec{t}(\hat{\bar{n}})\right] dS + \int_C \sigma \hat{s} dl = 0 \tag{3.2}$$

Substituting $\vec{t}(\hat{n}) = \hat{n} \cdot \mathbf{T}$ and $\vec{t}(\hat{\bar{n}}) = \hat{\bar{n}} \cdot \bar{\mathbf{T}} = -\hat{n} \cdot \bar{\mathbf{T}}$, to yield

$$\int_S \left[\hat{n} \cdot \mathbf{T} - \hat{n} \cdot \bar{\mathbf{T}}\right] dS + \int_C \sigma \hat{s} dl = 0 \tag{3.3}$$

Recall Stokes theorem with contour C as boundary:

$$\int_C \vec{F} \cdot \hat{\tau} dl = \int_S \hat{n} \cdot \left(\nabla \times \vec{F}\right) dS \tag{3.4}$$

Now let $\vec{F} = \vec{f} \times \vec{b}$, where $\vec{f}$ and $\vec{b}$ are arbitrary vectors, let $\vec{b}$ be a constant, we thus have

$$\int_C \left(\vec{f} \times \vec{b}\right) \cdot \vec{\tau} dl = \int_S \hat{n} \cdot \left(\nabla \times \vec{f} \times \vec{b}\right) dS \tag{3.5}$$

Using vector identities $\vec{a} \cdot \left(\vec{b} \times \vec{c}\right) = \left(\vec{a} \times \vec{b}\right) \cdot \vec{c}$ and $\nabla \times \left(\vec{f} \times \vec{b}\right) = \left(\vec{b} \cdot \nabla\right) \vec{f} - \vec{b} \left(\nabla \cdot \vec{f}\right)$ (since $\vec{b}$ is constant), to get

$$\vec{b} \cdot \int_C \left(\vec{f} \times \vec{\tau}\right) dl = \vec{b} \cdot \int_S \left[\hat{n} \left(\nabla \cdot \vec{f}\right) - \left(\nabla \vec{f}\right) \cdot \hat{n}\right] dS \tag{3.6}$$

Since $\vec{b}$ is arbitrary, it is canceled at both sides. Then, choose $\vec{f} = \sigma\hat{n}$ and use the relationship $\hat{n} \times \hat{\tau} = -\hat{s}$, we then have

$$\begin{aligned} -\int_C \sigma\hat{s}dl &= \int_S \left[\hat{n}\nabla\cdot(\sigma\hat{n}) - \nabla(\sigma\hat{n})\cdot\hat{n}\right] dS \\ &= \int_S \left[\hat{n}\nabla\sigma\cdot\hat{n} + \sigma\hat{n}(\nabla\cdot\hat{n}) - \nabla\sigma - \sigma(\nabla\hat{n})\cdot\hat{n}\right] dS \end{aligned} \tag{3.7}$$

Since $\nabla\sigma$ is tangent to surface S, we have $\nabla\sigma\cdot\hat{n} = 0$. Also, by expansion into index notation in Cartesian system, we have

$$(\nabla\hat{n})\cdot\hat{n} = \left(\partial_i\hat{n}_j\right)\hat{n}_j = \partial_i\left(\hat{n}_j\hat{n}_j\right)/2 = 0$$

therefore to yield the desired results:

$$\int_C \sigma\hat{s}dl = \int_S \left[\nabla\sigma - \sigma\hat{n}(\nabla\cdot\hat{n})\right] dS \tag{3.8}$$

Substitute Equation (3.8) into Equation (3.3), and let the surface integrand vanish since the surface integral element is arbitrary, to obtain the **interfacial stress balance equation**,

$$\hat{n}\cdot\mathbf{T} - \hat{n}\cdot\bar{\mathbf{T}} = \sigma(\nabla\cdot\hat{n})\hat{n} - \nabla\sigma \tag{3.9}$$

Equation (3.9) interprets that the stress exerted at the interfacial area from hydrodynamic stress of liquids on both sides is balanced by normal surface tension associated with local curvature and tangent surface tension associated with surface tension gradient.

The normal component of surface stress balance is found by the inner-product between $\cdot\hat{n}$ and the Equation (3.9),

$$\hat{n}\cdot\mathbf{T}\cdot\hat{n} - \hat{n}\cdot\bar{\mathbf{T}}\cdot\hat{n} = \sigma(\nabla\cdot\hat{n}) \tag{3.10}$$

The tangential component of surface stress balance is found by inner-producting $\cdot\hat{\tau}$ to the Equation (3.9),

$$\hat{n} \cdot \mathbf{T} \cdot \hat{\tau} - \hat{n} \cdot \bar{\mathbf{T}} \cdot \hat{\tau} = \nabla\sigma \cdot \hat{\tau} \tag{3.11}$$

3.1.2 Modeling of planar surface tension dynamics with surfactant

The dynamic equation to connect surface tension to surface strain rate at planar gas-liquid interface supplied and used by[87, 88, 70, 154], either in analysis of experimental results or in numerical simulation configurations, is stated below (in x-direction. a similar version can be derived in z-direction):

$$\mu(\frac{\partial u}{\partial y} + \frac{\partial v}{\partial x}) = \frac{\partial \sigma}{\partial x} + (\kappa^s + \mu^s)\frac{\partial}{\partial x}(\frac{\partial u}{\partial x} + \frac{\partial w}{\partial z}) + \mu^s(\frac{\partial u}{\partial z} - \frac{\partial w}{\partial x}) \tag{3.12}$$

where μ^s and κ^s are interfacial shear and dilatational viscosities, respectively.

The first-order correction for a non-planar interface[88, 155], $\partial v/\partial x$ is expected to be $m^2\,(\partial u/\partial y)$, where m is the surface curvature. At low surface deformation, this term is negligible. For weak convection and quasi-stagnant monolayer film of insoluble surfactant, interfacial viscosities may be neglected[88]. This leaves the leading term $\mu^s\left(\partial^2 u/\partial z^2\right)$, which can be shown to be over two orders of magnitude smaller than the values of the two other remaining terms in the stress balance[88].

After above simplification, the stress balance can finally be written as

$$\mu\frac{\partial u}{\partial y}\Big|_{y=0} = \frac{d\sigma}{dx} \tag{3.13}$$

via the chain rule, the elastic term is rewritten to incorporate surfactant concentration γ as

$$\mu\frac{\partial u}{\partial y}\Big|_{y=0} = \frac{d\sigma}{d\gamma}\Big|_{\gamma=\gamma_0}\frac{d\gamma}{dx} \tag{3.14}$$

In simulation modeling, the surface elasticity term $M = (d\sigma/d\gamma)|_{\gamma=\gamma_0}$ is constitu-

tively evaluated at the steepest slope of oleyl alcohol at $\gamma_0 = 1.4mg/m^2$ in Figure 9 of[88], in which the surface tension-surfactant concentration relationship is experimentally calibrated. M is then kept constant so as to resemble a linear surfactant model throughout the simulation.

To close the system, the evolution equation of surfactant concentration is constructed below:

$$\frac{\partial \gamma}{\partial t} + \nabla \cdot (\gamma \vec{u}_s) = \alpha_s \nabla^2 \gamma \tag{3.15}$$

where $\vec{u}_s$ is the 2-D velocity composed of velocity components u, w at surface. α_s is the interfacial diffusivity of surfactant. Though α_s is unknown for most kinds of surfactant, it is expected to be orders of magnitude smaller than advection effects[87].

3.2 Numerical procedure

3.2.1 Modified top boundary condition for insoluble surfactant

To sum up, the top boundary with surfactant dynamics is

$$\frac{\partial \gamma}{\partial t} + \nabla \cdot (\gamma \vec{u}_s) = \alpha_s \nabla^2 \gamma \tag{3.16}$$

$$\sigma = \sigma_0 - M(\gamma - \gamma_0) \tag{3.17}$$

$$\mu \frac{\partial u}{\partial y} = \frac{\partial \sigma}{\partial x} \tag{3.18}$$

$$\mu \frac{\partial w}{\partial y} = \frac{\partial \sigma}{\partial z} \tag{3.19}$$

after scaling with Rayleigh scale in Table 2.2, the non-dimensional top boundary condition goes:

$$\frac{\partial \gamma}{\partial t} + \nabla \cdot (\vec{u}_s \gamma) = \frac{1}{Pe} \nabla^2 \gamma \tag{3.20}$$

$$\sigma = 1 - Ma(\gamma - 1) \tag{3.21}$$

$$\frac{\partial u}{\partial y} = \frac{Re}{We}\frac{\partial \sigma}{\partial x} \tag{3.22}$$

$$\frac{\partial w}{\partial y} = \frac{Re}{We}\frac{\partial \sigma}{\partial z} \tag{3.23}$$

$$v = 0 \tag{3.24}$$

where $\vec{u_s} = u\hat{e}_x + w\hat{e}_z$ is the velocity vector in top surface, $Pe = \alpha/\alpha_s$ is defined as the Peclet number of surfactant, $Ma = M\,(\gamma_0/\sigma_0)$ is the Marangoni number of surfactant, $We = \rho U_{sc}^2 L_{sc}/\sigma_0$ is the Weber number defined as surface kinetic energy versus surface tension energy.

In application of the surfactant boundary condition to the spectral scheme given in section 2.4, the following modifications are required:

(1) Modification of the velocity top boundary condition from Dirichlet condition or Neumann condition to dynamic condition with second-order derivatives;

(2) Development of a subroutine that deals with the particular boundary condition, including computation of velocity at surface and surfactant concentration evolution at surface;

(3) Concern of the stability and accuracy of the subroutine.

In programming level, the subroutine in charge of top boundary condition is implemented in the following computational steps:

(1) Evaluate surface tension σ from surfactant concentration γ from Equation (3.21);

(2) From surface tension gradient obtained in step (1), obtain surface velocity shear rate as second derivative boundary condition for the main spectral solver for bulk, according to Equation (3.22),(3.23);

(3) Advance surfactant concentration according to Equation (3.20), the nonlinear advection term is evaluated in physical space. This step is like a 2-D mini version of the bulk spectral solver.

3.2.2 Simulation design, scheduling and processing

The simulation process is designed as 4 stages: (1) preparation of the disturbed flow as initial condition, (2) realization of multiple instances of the flow with various level of surfactant contamination to be tested, (3) simulation of the transient period where the temporal impact of surfactant surface condition to the flow dies out, and (4) a major, continuous run for sufficient long period while the flow stays in steady state.

The disturbed initial condition is generated within $Matlab$, where a zero velocity and uniform temperature flow field is combined with Gaussian white noise that has 5% less energy compared to the order of full turbulence. The noise satisfies both clean case surface boundary condition and thermal boundary condition (see section 3.2.1). The initial condition is imported to the spectral solver with clean surface and let free to evolve. Since the flow is cooled from above, Rayleigh instability is triggered through initial perturbation, the flow self-evolves under governing equations (2.27), (2.28), and (2.29), to finally reach the status of regular convection.

At the end of the preparation period, after the clean flow reaches steady state (verified through statistics), one frame of the realization is taken as the initial condition of all the major steady state runs. These major runs include one clean case, and several contaminated cases with different levels of surfactant concentration, as is seen in Table 3.1. For the clean case, the continuous run is carried out without special interruption. For contaminated cases, the surfactant boundary condition are switched on, and initially uniformly distributed surfactant with various concentration (Marangoni number) are imposed on each instances, referring to Table 3.1. For the contaminated cases, this indicates their transient period of adapting the impact of surfactant boundary condition. After these cases being settled down, the steady state runs are carried out as is planned. It is worth mentioning that the transient response of surfactant boundary condition turns out to be interesting

and is discussed as well.

Table 3.1: Simulation parameters: non-dimensional numbers of the flow

Run	Ma	Ra_q	Pr	Re	Pe	We
1	0	4.45×10^8	7.0	0.143	1.43×10^{-3}	3.17×10^{-9}
2	2.40×10^{-4}	4.45×10^8	7.0	0.143	1.43×10^{-3}	3.17×10^{-9}
3	2.40×10^{-3}	4.45×10^8	7.0	0.143	1.43×10^{-3}	3.17×10^{-9}
4	2.40×10^{-2}	4.45×10^8	7.0	0.143	1.43×10^{-3}	3.17×10^{-9}
5	0.120	4.45×10^8	7.0	0.143	1.43×10^{-3}	3.17×10^{-9}
6	0.240	4.45×10^8	7.0	0.143	1.43×10^{-3}	3.17×10^{-9}

The simulation parameters for each run are summarized in Table 3.1 in which all non-dimensional numbers listed are defined in section 2.2.3 for bulk and section 3.2.1 for dynamic surface boundary condition with surfactant. The Rayleigh number was set to $Ra_q = 4.45 \times 10^8$ in all simulations. This corresponds to a heat flux of $Q = 100W/m^2$, and a domain height of $Ly = 11.713cm$, for water at $25°\mathrm{C}$. We designate this case as the 'standard' case. Based on these values, the distance between the surface and the first grid node beneath the surface is $17.6\mu m$. The other parameters, Pr, Re, Pe, and We were held fixed as indicated in Table 3.1.With these numbers held constant, the Marangoni number was varied over a wide range spanning three orders of magnitude, which corresponds to increasing surface contamination from weak ($Ma = 2.4 \times 10^{-4}$) to strongly contaminated ($Ma = 2.4 \times 10^{-1}$). In effect, the Marangoni number thus defined can be considered a measure of surface elasticity.

Table 3.2: Simulation parameters: computational domain and grid

L_x/L_y	L_z/L_y	nx	ny	nz
2	2	128	129	128

Each simulation with nonzero elasticity (with the exception of runs 4 and 5) were run until a statistically steady state was achieved and at that point statistics were computed over a time $\Delta t/t^* \approx 6$ which also corresponds to 390 seconds of dimensional time for the standard case. For runs 4 and 5 it was found that only small changes (compared to run 6) were observed in the thermal and velocity statistics during the early stages of these simulations. It was therefore decided not to run these simulations to a statistically steady state. To obtain the statistics for the clean case, we averaged over approximately 1000 seconds in the standard case, or $\Delta t/t^* \approx 15.2$.

3.3 Results and discussion

3.3.1 Onset of free convection

In free surface convection, the aforementioned thermal boundary layer 'cool skin layer' forms beneath the surface. Due to the constant outgoing heat flux, the layer constantly grows until it goes unstable and buoyancy driven local advection happens. The detailed process is as below: Based on the assumption that density of water is inversely, linearly dependent on its temperature(which holds true around ambient condition), the cooler flow at the upper level gets denser than the flow in the bulk below, which is referred to as the inverse density stratified layers[124, 122]. The configuration is described by Rayleigh number, roughly the ratio of buoyancy and viscosity forces times the ratio of momentum and thermal diffusivities. Because of the constant outgoing heat loss, *Ra* keeps increase. When *Ra* exceeds the critical number of Rayleigh instability Ra_c, infinitesimal perturba-

tion becomes amplified, in the macroscale, it is expressed in the way that layers break through each other to form circular advection, to give birth to evolution of subsurface boundary layer and to drive the flow beneath surface.

A standard procedure of linear analysis of Rayleigh instability is found elsewhere[124, 125], the analysis consists of several steps: 1) apply linear perturbation to base state on governing equations; 2) linearize perturbed governing equations to obtain equations for perturbation; 3) represent and decompose perturbations with normal mode analysis; 4) solve modal equations to obtain the dispersion relation of eigenvalues of each mode regarding to modal number; 5) determine modal amplification or damping upon the criterion $\forall s : \lambda(s) < 0$ for stability and vise versa.

3.3.2 Surface pattern and spectral density analysis

Temperature plays the role of a good tracer of flow field, since heat diffuses in the same order of momentum diffusion. Therefore, the evolution of the thermal boundary layer demonstrates a vivid picture of convection flow structure beneath free surface. After instability arise, as is described in section 3.3.1, surface breaks up into regions where convergence and divergence take place. Naturally, and is also predicted in the instability theory[124], convergence zone shrinks into streaks, and divergence zone expands into cells, thus to form the famous hexagonal surface pattern of Benard convection.

Also, effects of surfactants on the convection flow can be intuitively gained by viewing instantaneous snapshots of the surface temperature and the corresponding surfactant concentration over a range of Marangoni numbers. These snapshots, which were obtained when each flow was in a statistically steady state, are shown in Figure 3.2 through Figure 3.5. Here it is evident that the surface temperature field can be described in all cases as being composed of thin cold bands surrounding larger regions of warmer fluid. Flow visualizations (see Figure 3.9 through Figure 3.16) of this flow clearly indicate that the thin cold bands are regions of surface convergence, corresponding to sinking fluid, while

regions of warmer fluid correspond to regions of upwelling which are associated with a divergent flow. Here, surface convergence and divergence are defined by $\partial v/\partial y > 0$ and $\partial v/\partial y < 0$ respectively. The snapshots clearly indicate the general cooling of the surface as the surface elasticity is increased, which mirrors the statistical results discussed above. In Figure 3.6 through Figure 3.8, the corresponding surfactant concentration images are shown. These images clearly indicate that the surfactant concentration is greatest in regions of convergence, and least in divergent regions, as we would expect. In this sense, the surfactant concentration images mirror remarkably well the surface temperature map. This indicates that the choice of the surfactant diffusion coefficient is sufficiently small to capture the phenomena of interest in this investigation. We note, as discussed in more detail in[73], that real surfactants have diffusion coefficients much smaller than the one used here, but directly implementing flows with these coefficients would be numerically prohibitive. As a result, we are currently exploring the possibility of using methods such as a hyperviscosity to more realistically model surfactant diffusion. A particularly intriguing result indicated in Figure 3.2 through Figure 3.5 is the apparent decrease in the scale size of the convective cells as the surface elasticity is increased.

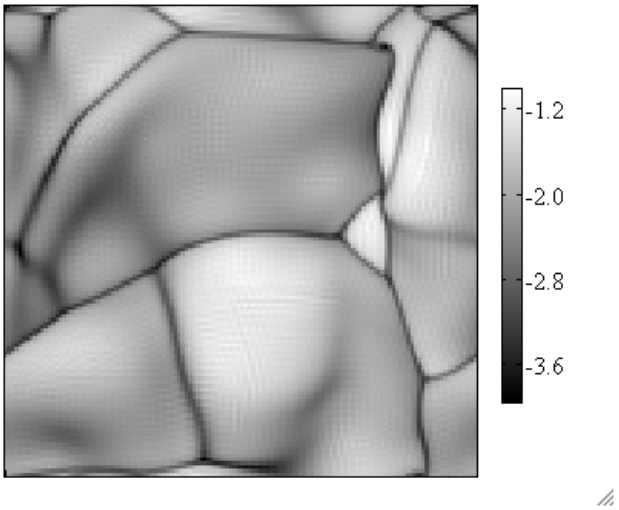

Figure 3.2: Instantaneous visualization of normalized surface temperature θ/θ^* for different surface elasticity. The entire surface of the computational domain is shown. (a) Clean case ($Ma = 0$)

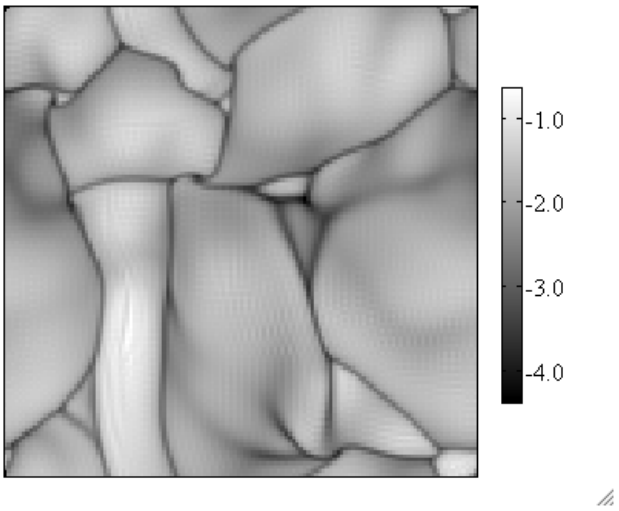

Figure 3.3: Instantaneous visualization of normalized surface temperature θ/θ^* for different surface elasticity. The entire surface of the computational domain is shown. (b) $Ma = 2.4 \times 10^4$

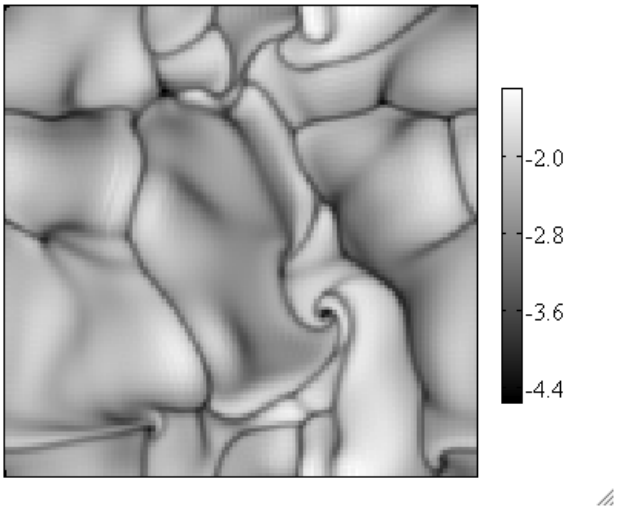

Figure 3.4: Instantaneous visualization of normalized surface temperature θ/θ^* for different surface elasticity. The entire surface of the computational domain is shown. (c) $Ma = 2.4 \times 10^3$

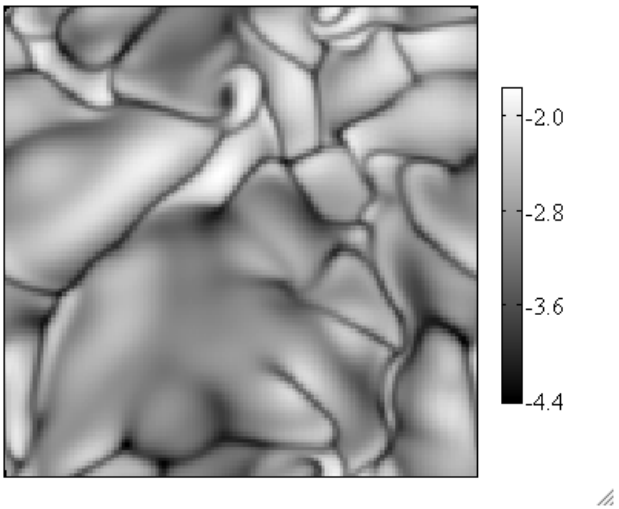

Figure 3.5: Instantaneous visualization of normalized surface temperature θ/θ^* for different surface elasticity. The entire surface of the computational domain is shown. (d) $Ma = 0.24$

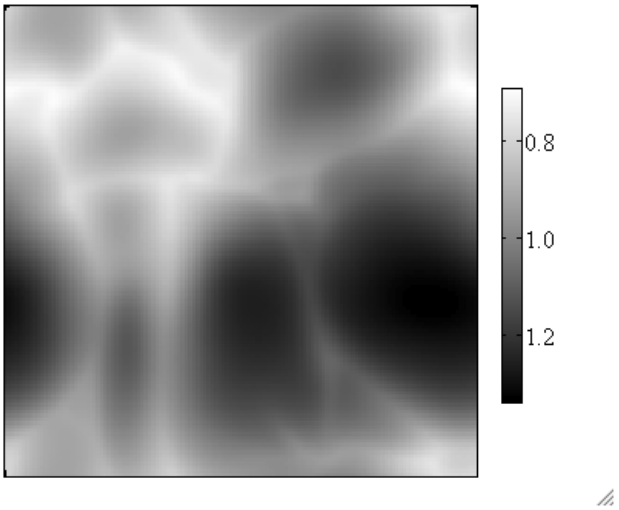

Figure 3.6: Instantaneous visualization of the normalized surfactant concentration γ/γ^* for different surface elasticity. The entire surface of the computational domain is shown. These images were obtained at the same time instants as those in Figures 3.2 through 3.5. γ^*/γ_0 is the initial uniform surfactant concentration. (a) $Ma = 2.4 \times 10^4$

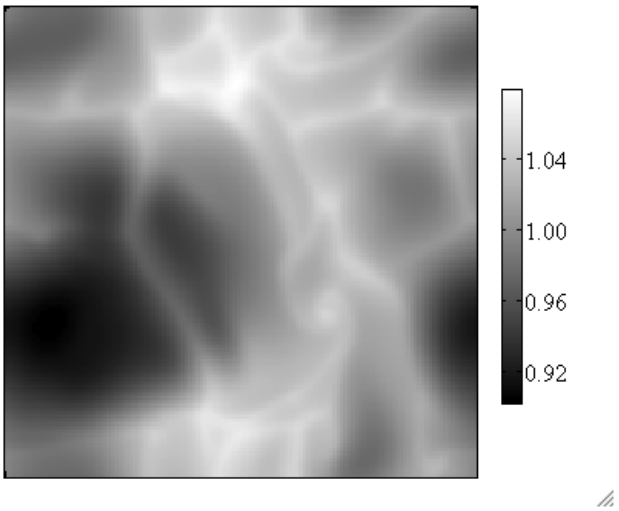

Figure 3.7: Instantaneous visualization of the normalized surfactant concentration γ/γ^* for different surface elasticity. The entire surface of the computational domain is shown. These images were obtained at the same time instants as those in Figures 3.2 through 3.5. γ^*/γ_0 is the initial uniform surfactant concentration. (b) $Ma = 2.4 \times 10^3$

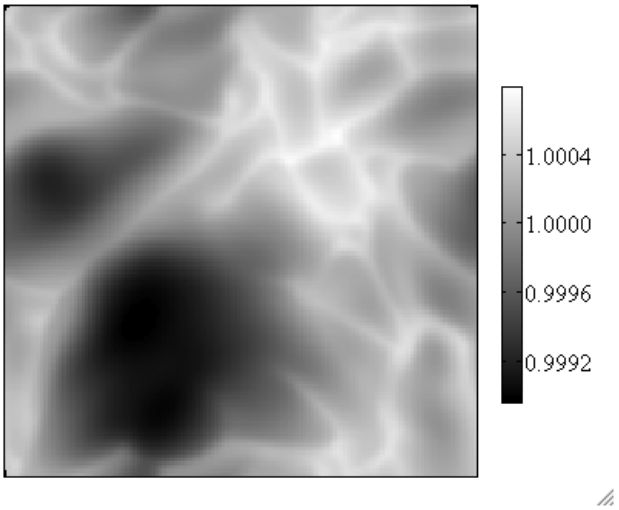

Figure 3.8: Instantaneous visualization of the normalized surfactant concentration γ/γ^* for different surface elasticity. The entire surface of the computational domain is shown. These images were obtained at the same time instants as those in Figures 3.2 through 3.5. γ^*/γ_0 is the initial uniform surfactant concentration. (c) $Ma = 0.24$

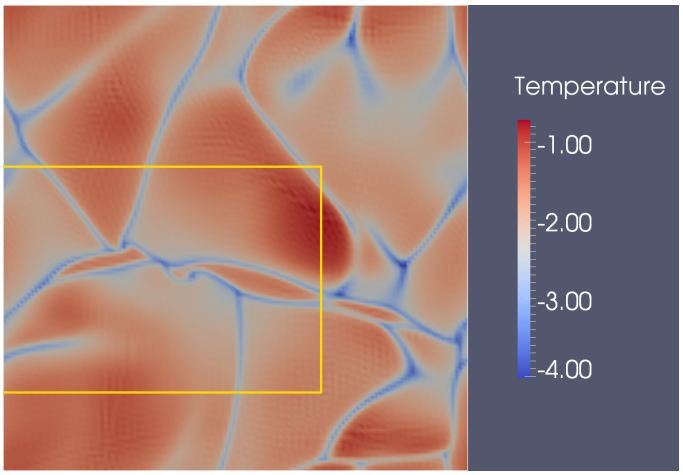

Figure 3.9: Time evolution of the surface temperature, θ/θ^*, for the clean case showing the formation of a cold-core vortex. The total elapsed time in the sequence (a) through (d) is 60 seconds with 20 seconds between images, here time is computed using the 'standard' case defined in the text.(a) 1st snapshot.

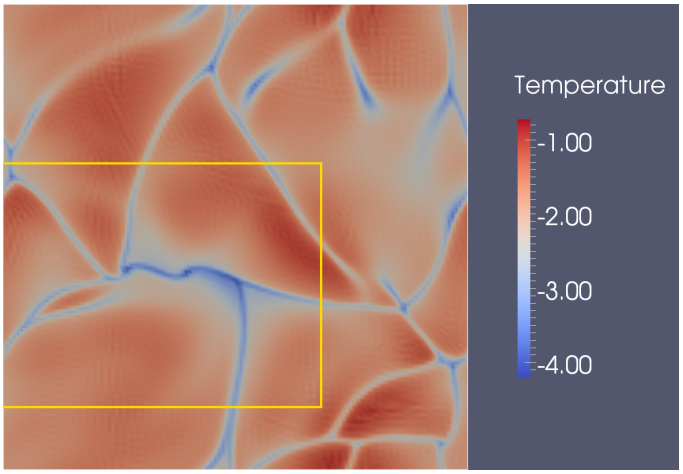

Figure 3.10: Time evolution of the surface temperature, θ/θ^*, for the clean case showing the formation of a cold-core vortex. The total elapsed time in the sequence (a) through (d) is 60 seconds with 20 seconds between images, where here time is computed using the 'standard' case defined in the text.(b) 2nd snapshot.

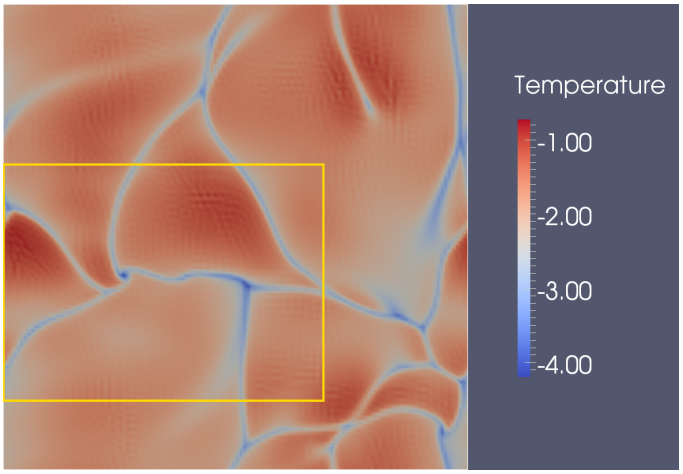

Figure 3.11: Time evolution of the surface temperature, θ/θ^*, for the clean case showing the formation of a cold-core vortex. The total elapsed time in the sequence (a) through (d) is 60 seconds with 20 seconds between images, where here time is computed using the 'standard' case defined in the text.(c) 3rd snapshot.

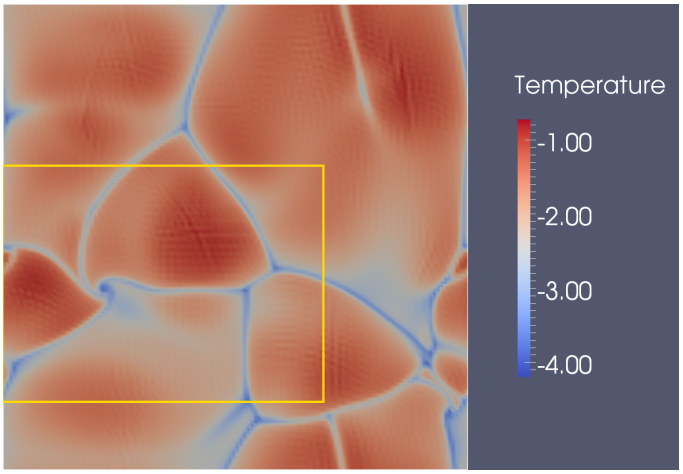

Figure 3.12: Time evolution of the surface temperature, θ/θ^*, for the clean case showing the formation of a cold-core vortex. The total elapsed time in the sequence (a) through (d) is 60 seconds with 20 seconds between images, where here time is computed using the 'standard' case defined in the text.(d) 4th snapshot.

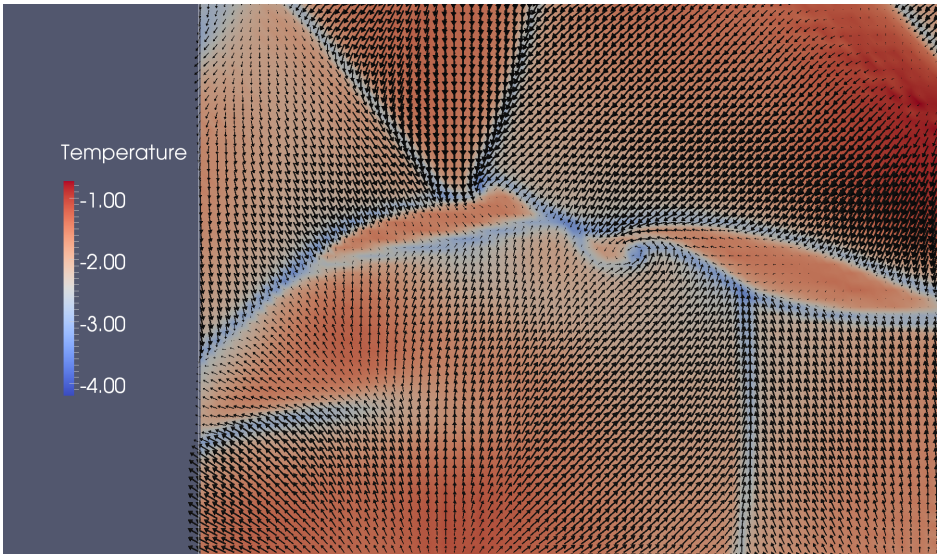

Figure 3.13: Surface temperature and surface velocity vectors associated with the boxes in Figures 3.9 through 3.12.(a) 1st snapshot.

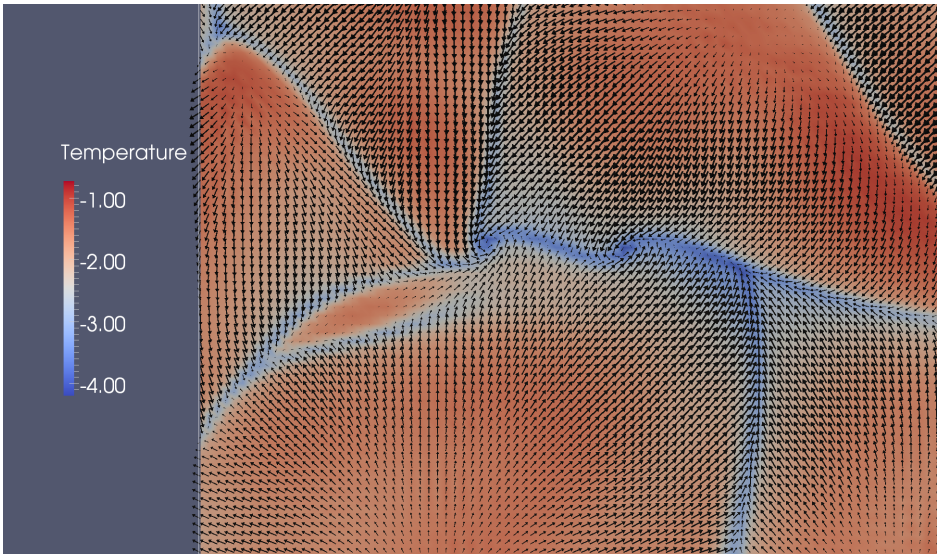

Figure 3.14: Surface temperature and surface velocity vectors associated with the boxes in Figures 3.9 through 3.12.(b) 2nd snapshot.

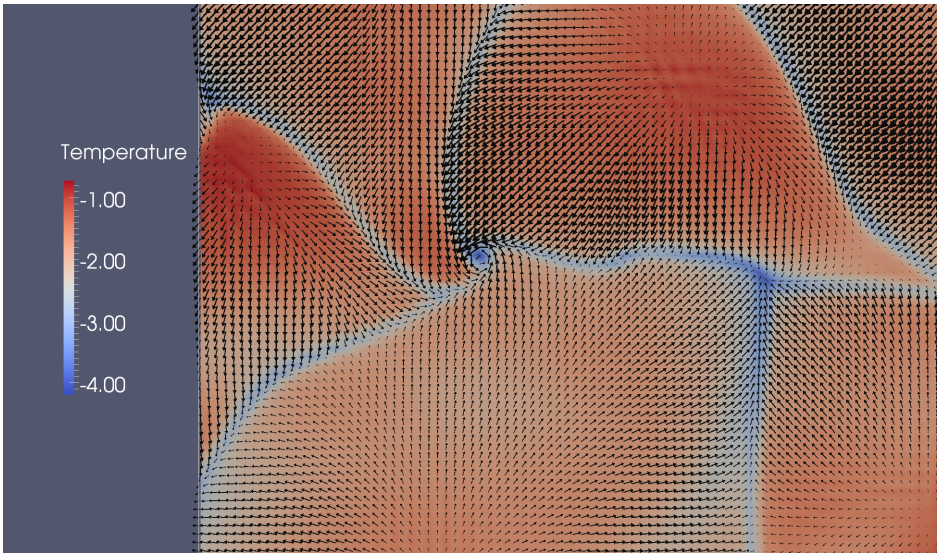

Figure 3.15: Surface temperature and surface velocity vectors associated with the boxes in Figures 3.9 through 3.12.(c) 3rd snapshot.

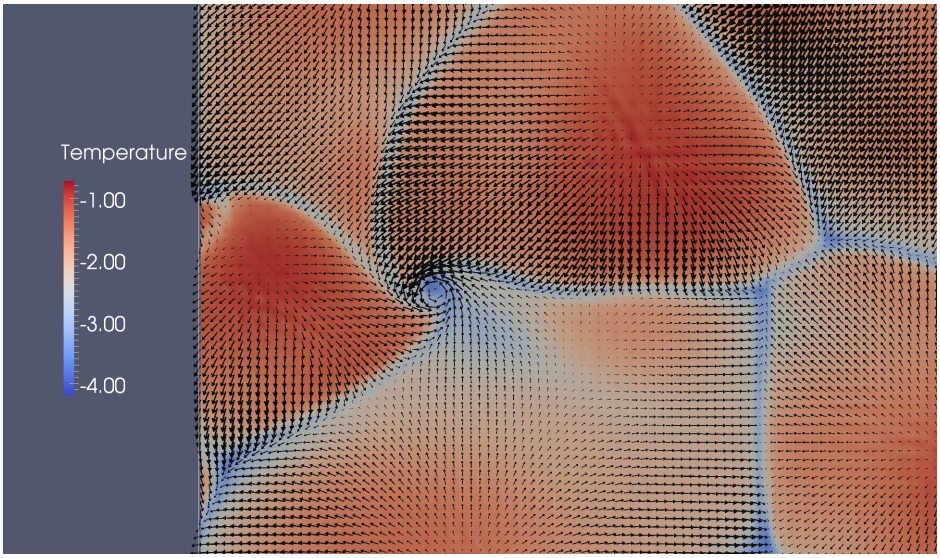

Figure 3.16: Surface temperature and surface velocity vectors associated with the boxes in Figures 3.9 through 3.12.(d) 4th snapshot.

The result that the apparently decreasing in the scale size of the convective cells as increased surface elasticity is somewhat counterintuitive, since one might expect that as elasticity increases, smaller less energetic cells might be damped out by the additional resistance offered by the surfactant. To explore this effect in a more quantitative manner, we show the Fourier spectral energy density of the surface temperature, normalized by the mean square surface temperature, for each case in Figure 3.17.

In Figure 3.17, several features are evident including:

(1) An inertial $\kappa^{-5/3}$ region exists in each case where here $\kappa = 2\pi/\lambda$ is the wavenumber, and k is the wavelength of a Fourier mode.

(2) The presence of surface elasticity clearly decreases the spectral density at high wavenumbers with respect to the clean case.

(3) The presence of surfactants increases the spectral energy content of the thermal field in the inertial region (mid-band wavenumbers) relative to the clean case.

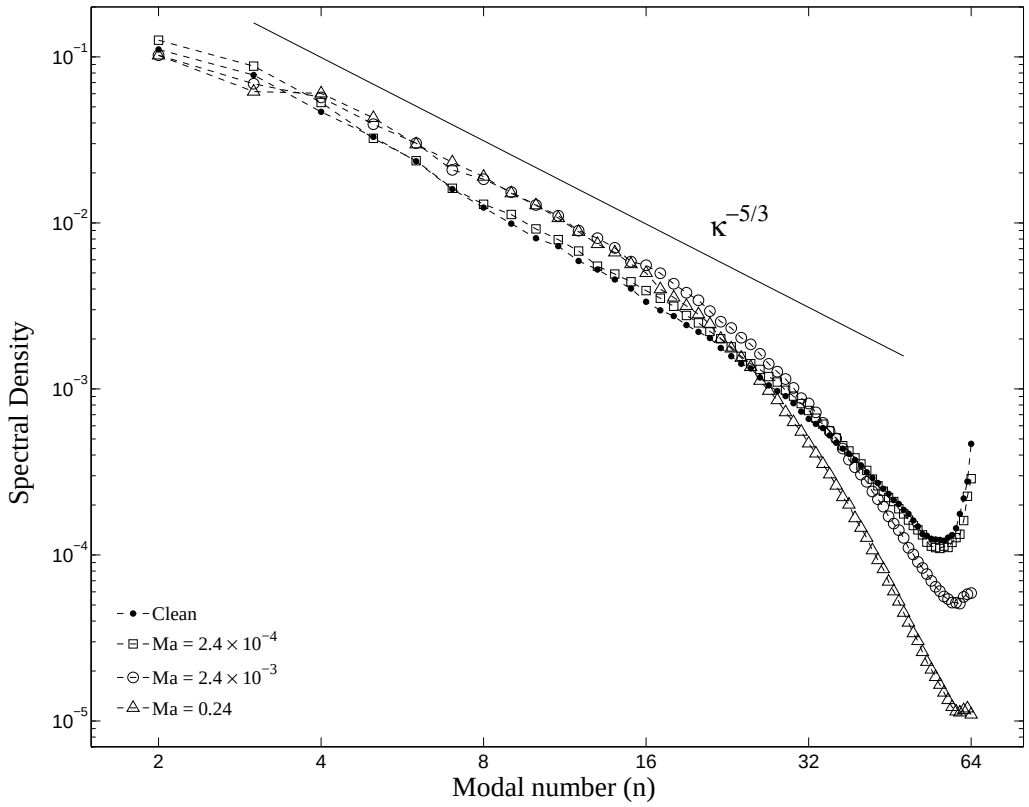

Figure 3.17: Fourier spectral density of the surface temperature field for different elasticities. These spectra were obtained by averaging over all available flow realizations, and were normalized by the mean-square surface temperature. The modal number n is defined such that $n = 1$ corresponds to a sinusoidal wavelength of L_z, the domain size in the z (or x) direction. The Kolmogorov inertial spectrum ($\kappa^{-5/3}$) is shown for reference.

This result is in reasonable agreement with the spectrum shown in[156], (their Figure 3), which also shows a decrease in high wavenumber (small scales) thermal scales and an increase at lower wavenumbers. However, though our spectra are compatible with[156], their infrared imagery (see their Figure 2) shows much more small scale structure in the clean case than ours. At the present time, we cannot resolve this discrepancy, but one possibility is that the aforementioned experiments were performed at a higher Rayleigh

number than our direct simulations. On the other hand, we have performed a preliminary investigation of the effect surfactants on the structure of the thin cold bands observed in the direct numerical simulation imagery, and found that the bands evolve from a cusp shape in the clean case, to smoother, Gaussian-like shapes in the highly contaminated cases. This seems reasonable from a physical point of view, as the surfactants must decrease the intensity of the convergent regions. It also may explain the decrease in spectral content at the highest wavenumbers, since a cusp-like function contains relatively more Fourier spectral content at high wavenumbers than that of a Gaussian.

3.3.3 Vortex and coherent structures

Although the main objective in this work is to determine the effects of surfactants on the turbulence generated by natural convection, we feel it appropriate to comment on a common experimental observation associated with this form of free surface turbulence: that is, the occasional generation of discrete vortices at the surface. These have been observed experimentally[157] and numerically[6]. It is interesting to note that in all of these studies, the vortices are always observed to have cold cores. We explore this phenomenon further by displaying a sequence of snapshots of the entire surface in Figure 3.9(clean case) through Figure 3.12 and displaying close-up views in Figure 3.13 through Figure 3.16 of the evolution of one typical vortex. The images were obtained by first identifying a fully formed vortex in an image, and then going back in time to obtain earlier images with the intent of determining the process of formation of that specific vortex. The image sequence shown in Figure 3.9 through Figure 3.12 clearly shows that a well defined discrete vortex with a cold core forms (see Figure 3.12) after 60 seconds in the standard case. This particular vortex apparently formed as warmer regions of fluid shown in Figure 3.9 collapse onto colder bands of sinking, colder fluid. This process can be seen in greater detail in Figure 3.13 through Figure 3.16, where velocity vectors are superimposed onto the surface temperature map. These velocity vectors clearly indicate that regions of

warmer fluid are divergent flows, whereas the cold bands are convergent zones associated with fluid sinking into the interior. This suggests an obvious mechanism for the formation of these discrete vortices:

(1) Instability of a cold band due to shear flow parallel to the band.

(2) Amplification of the vertical vorticity associated with the shear by the stretching of vorticity due to the rapidly sinking fluid associated with these bands.

This simple mechanism seems to explain the fact that all discrete surface vortices have cold cores, since any random vertical vorticity in the vicinity of rising fluid associated with the warmer divergent regions, should be suppressed by the vertical compression of vortex lines in these regions.

3.3.4 Horizontal homogeneity and statistics of temperature, velocity and vorticity

We present the statistics for the temperature, velocity, and vorticity fields in Figure 3.18 through Figure 3.20 for three Marangoni numbers, as well as for the so called 'clean case', the case in which the surface was free of surfactant. In discussing the mean temperature field it is useful to define the bulk temperature in a manner consistent with[6] as the mean temperature corresponding to the depth δ_{bl} below the surface where the vertical temperature gradient is 5% of the surface gradient. This depth, δ_{bl}, is defined as the thermal boundary layer thickness. We also define $\Delta\theta_0 = |\theta_{top} - \theta_{bot}|$, where θ_{bot} and θ_{top} are the mean temperatures at the top (surface) and bottom of the domain respectively, and $\Delta\theta_1 = |\theta_{top} - \theta_{bl}|$ where θ_{bl} is the mean temperature at a depth of δ_{bl}. The temperature differences $\Delta\theta_0$, $\Delta\theta_1$, and the thermal boundary thickness δ_{bl}, as well as the Nusselt number Nu to be discussed in the next section, are listed for all completed runs in Table 3.3.

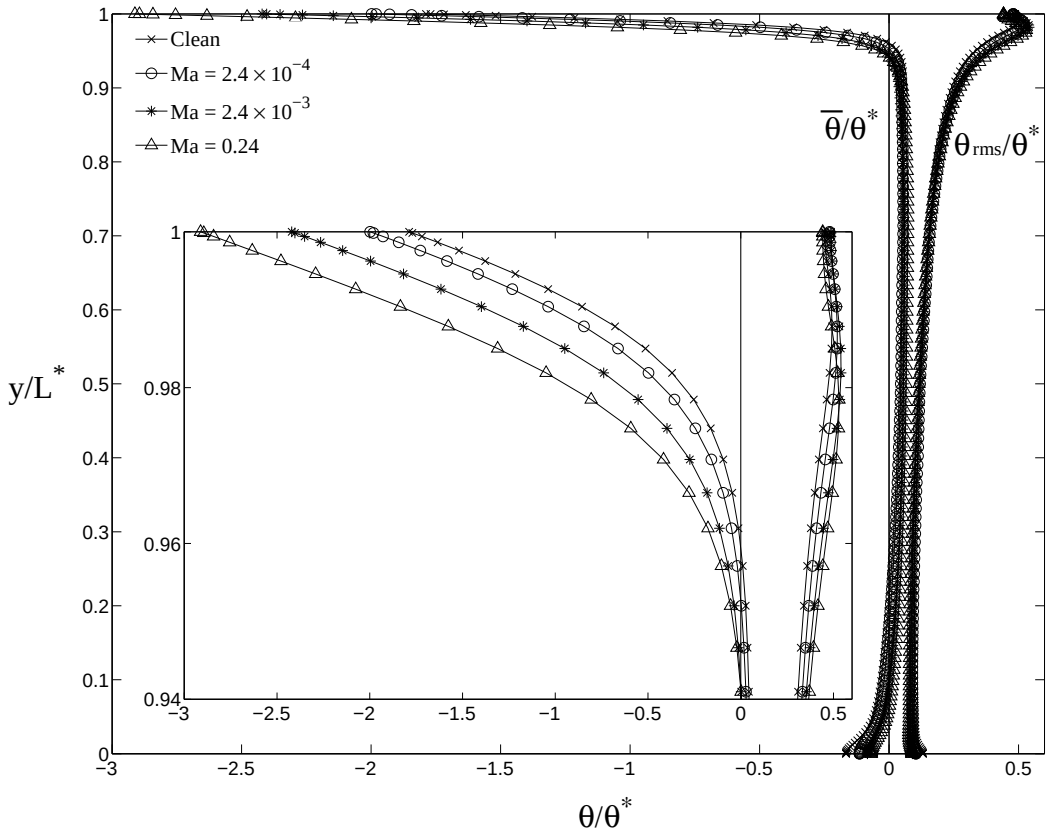

Figure 3.18: Mean and root-mean-square (rms) temperature profiles for different surface elasticity. Here $\overline{\theta}$ and θ_{rms}, the mean and rms temperatures, were obtained by horizontal averaging and averaging over all available flow realizations. The length scale L^* is defined in Table 2.2.

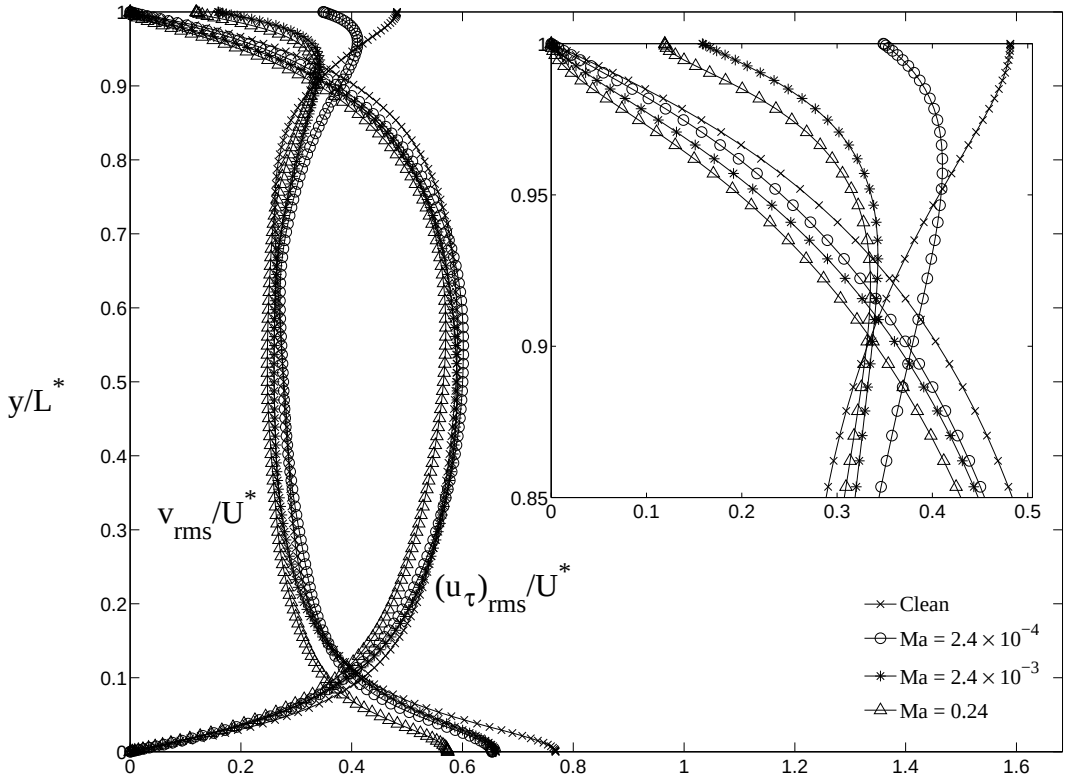

Figure 3.19: Vertical (v_{rms}) and tangential (($u_\tau)_{rms}$) velocity profiles for different surface elasticity. Here, $(u_\tau)_{rms} = \left[\left(u_{rms}^2 + w_{rms}^2\right)/2\right]^{1/2}$, where u_{rms} and w_{rms} are the rms velocities in x and z directions. The velocity scale U^* is defined in Table 2.2

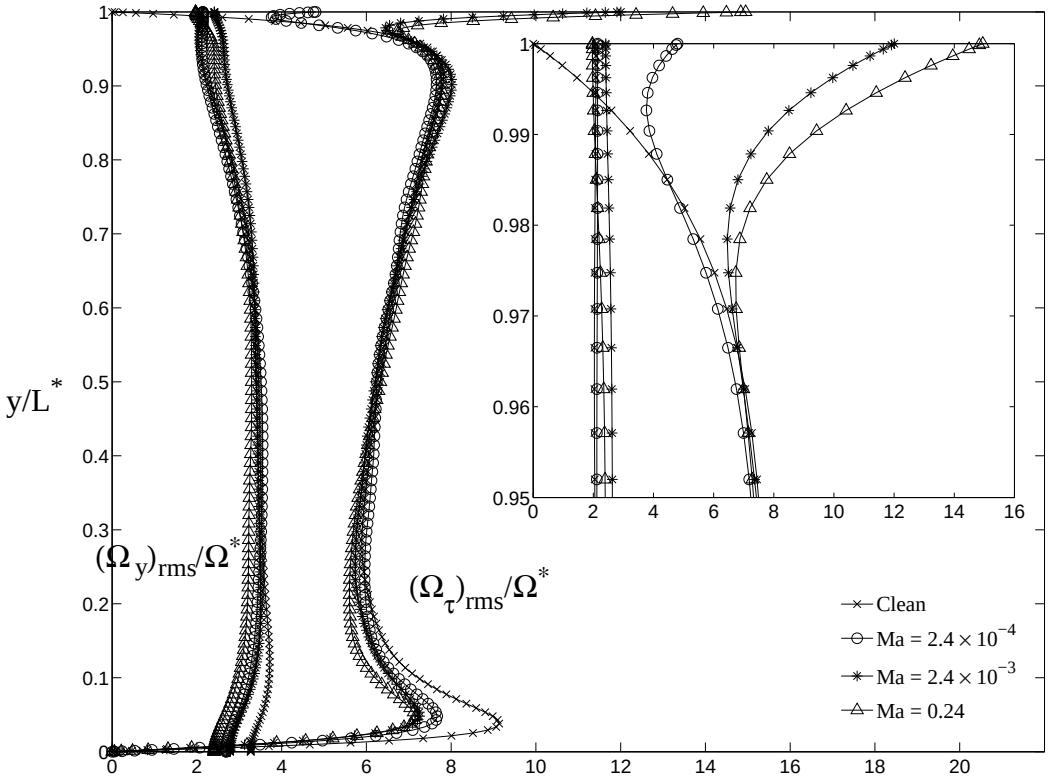

Figure 3.20: Vertical ($(\Omega_y)_{rms}$) and tangential ($(\Omega_\tau)_{rms}$) vorticity profiles for different surface elasticity. Here the tangential rms vorticity is defined by $(\Omega_\tau)_{rms} = \left[\left((\Omega_x)^2_{rms} + (\Omega_z)^2_{rms}\right)/2\right]^{1/2}$ where $(\Omega_x)_{rms}$ and $(\Omega_z)_{rms}$ are the rms vorticities in the x and z directions. The vorticity scale is $\Omega^* = U^*/L^*$.

Table 3.3: Horizontally averaged statistics of the simulation results

Run	Nu_0	Nu_1	$\Delta\theta_0$ (°C)	$\Delta\theta_0/\theta^*$	$\Delta\theta_1$ (°C)	$\Delta\theta_1/\theta^*$	δ_{bl}/L_y
1	71.45	2.519	0.2732	1.622	0.2996	1.779	0.0387
2	61.50	2.470	0.3174	1.884	0.3326	1.974	0.0421
3	49.57	2.287	0.3938	2.338	0.4008	2.379	0.0469
4	-	-	-	-	-	-	-
5	-	-	-	-	-	-	-
6	40.76	2.096	0.4789	2.843	0.4857	2.883	0.0522

* Here $Nu_0 = QL_y/k\Delta\theta_0$ is the Nusselt number defined across the simulation domain, $Nu_1 = Q\delta_{bl}/k\Delta\theta_1$ is the Nusselt number defined across the thermal boundary layer, $\Delta\theta_0 = \left|\theta_{top} - \theta_{bot}\right|$ is the temperature difference across the simulation domain,$\Delta\theta_1 = \left|\theta_{top} - \theta_{bl}\right|$ is the temperature difference across thermal boundary layer,$\theta^* = \sqrt{\pi/2}\,(\beta g/\alpha\nu)^{-1/4}\,(Q/k)^{3/4}$, and δ_{bl} is the thermal boundary layer thickness as defined in the text.

The statistics for the mean temperature, $\overline{\theta}$, and the root mean square temperature (rms), θ_{rms}, shown in Figure 3.18 exhibit several prominent features. Perhaps the most important one, which is not fully evident in Figure 3.18, is that run 6 ($Ma = 0.240$) represents what we call a saturated state or fully contaminated state. That is, as we noted above, a reduction of Ma by a factor of 2 and 10 (runs 4 and 5) produce only small changes in surface temperature and other statistics relative to run 6. In this sense, we assume that any increase in elasticity beyond that of run 6 will have essentially no effect on the statistics of the turbulence, and this case along with the clean case can then be used as the reference states. The most prominent effect of increased surface elasticity, which is clearly evident in Figure 3.18, is the corresponding decrease in the mean surface temperature. This result is of particular interest since it is surface temperature, as opposed to surface velocity, which is most

easily obtained by using currently available high resolution IR sensors[22, 126]. The results in Table 3.3 indicate that the thermal boundary layer thickness,δ_{bl}, increases by about 35% as the surface goes from clean to fully contaminated. Since the heat flux is fixed, the mean surface temperature must therefore decrease. The changes in $\Delta\theta_0/\theta^*$ and $\Delta\theta_1/\theta^*$ are accordingly 1.22 (75%) and 1.10 (62%) respectively, with respect to the clean case. This result was noted previously for channel flow turbulence[73], and in experiments[156]. Although it is beyond the scope of this investigation to delve into the detailed turbulence dynamics that give rise to an increased thermal boundary layer thickness, this result is physically reasonable in the context of surface renewal theory[48, 108]. Within the context of this idealized theory, increased surface elasticity can be expected to have a dampening effect on the dominant surface renewal eddies near the surface. It can easily be envisioned, for example, that as a counter-rotating pair of eddies approaches a contaminated surface, the eddies lose kinetic energy as they encounter the resistance offered by the elastic surface. This leads to an increase in the average surface renewal time scale, and therefore an increase in thermal boundary layer thickness results. An alternative, but equivalent model, the surface strain model (see[6] or[45]) leads to a similar conclusion.

In Figure 3.19 and 3.20 the results for the rms velocity and vorticity are shown. Due to the symmetry of the flow in the horizontal directions, there can be no statistical difference between the horizontal $(x-z)$ components of the velocity and vorticity, and therefore these components can be combined to give what we refer to as the tangential velocity and vorticity statistics in the figures. As a comparison, the simulations of[6] give about 0.48 for the rms tangential velocity at the surface, which compares well with 0.482 in our simulations for the clean case, where here the rms velocities are made non-dimensional by U^*. It is evident that the main effect of surface elasticity is to decrease the tangential velocity fluctuations and to enhance the tangential vorticity fluctuations. The vertical components of velocity and vorticity are seen to be relatively unaffected by the presence of surfactants.

It is important to observe in Figure 3.19 that the tangential velocity fluctuations do not go to zero, even in the case of the highest surface elasticity. Since the highest elasticity in our simulations is a so-called saturated state, this result implies that even under highly contaminated conditions, some flow continues to be maintained in the surface, so that a no-slip boundary condition is not likely to be an adequate model in such cases. The tangential vorticity fluctuations shown in Figure 3.20 are seen to increase significantly as surface elasticity increases, which is a direct result of the resistance of the surfactant to subsurface fluid motion (see Equation 3.22 to Equation 3.24) and the subsequent generation of local tangentially oriented surface shear. It is interesting to note that below approximately $y/L^* = 0.97$, in the top half of the domain, the tangential vorticity fluctuations are nearly unaffected by surface elasticity, so that as far as the vorticity is concerned, its region of influence is confined to a very thin surface layer.

3.3.5 Effect on heat transfer coefficient

Nusselt number is defined employing the discussion of scaling in section 2.2.3, as $Nu_0 = QL_y/k\Delta\theta_0$ and $Nu_1 = Q\delta_{bl}/k\Delta\theta_1$, corresponding to the heat transfer coefficient throughout the entire computational domain, and the heat transfer coefficient in the vicinity of surface. The Nusselt number and the relevant temperature differences $\Delta\theta_0$, $\Delta\theta_1$ and the thermal boundary thickness δ_{bl} are listed in Table 3.3.

We also list in Table 3.3 the dimensional values of $\Delta\theta_0$ and $\Delta\theta_1$ and note that changes in these temperature differences due to surface elasticity are on the order of $0.2°\mathrm{C}$. This temperature difference can easily be detected in experiments with state-of-the-art infrared imagers which typically have a sensitivity of $10 \times 10^{-3}°\mathrm{C}$[22]. The Nusselt numbers Nu_0 and Nu_1 listed in Table 3.3 show decreases, with increased elasticity, of 43% and 17% with respect to the clean case. Somewhat surprisingly, the characteristic magnitude of the thermal fluctuations at the surface and in the fluid at depth appears to be relatively unaffected by the presence of a surfactant. These results compare favorably with those

of[6] for the same Rayleigh number in the clean case. For example, Leighton[6] obtains $\Delta\theta_1/\theta^* \approx 1.76$, $\theta_{rms}/\theta^* \approx 0.46$ and $\delta_{peak}/\Delta \approx 1.3$, where θ_{rms} is the rms temperature at the surface, δ_{peak} is the distance beneath the surface at which the rms temperature reaches its maximum value, and $\Delta = \sqrt{2}(\beta g Q/\rho c_P \nu \alpha^2)^{-1/4}$ and our corresponding results are 1.78, 0.45, and 1.25. Finally we note that the so called 'piston velocity', which is commonly used in oceanographic investigations to describe oceanic surface heat and mass flux, and is defined by $U_{pist} = Q/\rho c_p \Delta\theta_0$, can be directly related to the Nusselt number via $Nu_0 = U_{pist} L_y/\alpha$.

3.3.6 Elasticity-turbulence interaction parameter

As we have indicated above, as the surface elasticity embodied in the Marangoni number is changed from 0.24 to 0.024, we observe little change in surface temperature, and have concluded that this range of values can be considered essentially a saturated, or nearly saturated state of surface contamination. Similarly, our results indicate that when $Ma < 2.4 \times 10^4$, the surface can be considered nearly free of surfactant. These observations suggest, as we have indicated in Figure 3.21, that the relationship between the surface temperature and Marangoni number, is not only nonlinear, but is sigmoidal. In fact the dashed line in Figure 3.21, which is of the form $\Delta\theta_1 \approx tanh(\sqrt{Ma})$, gives a satisfactory fit to the direct numerical simulation results, particularly when taking into account the results from runs 4-6. We emphasize, of course, that this sigmoidal curve is only meant to be suggestive of what a more extensive set of numerical investigations would yield.

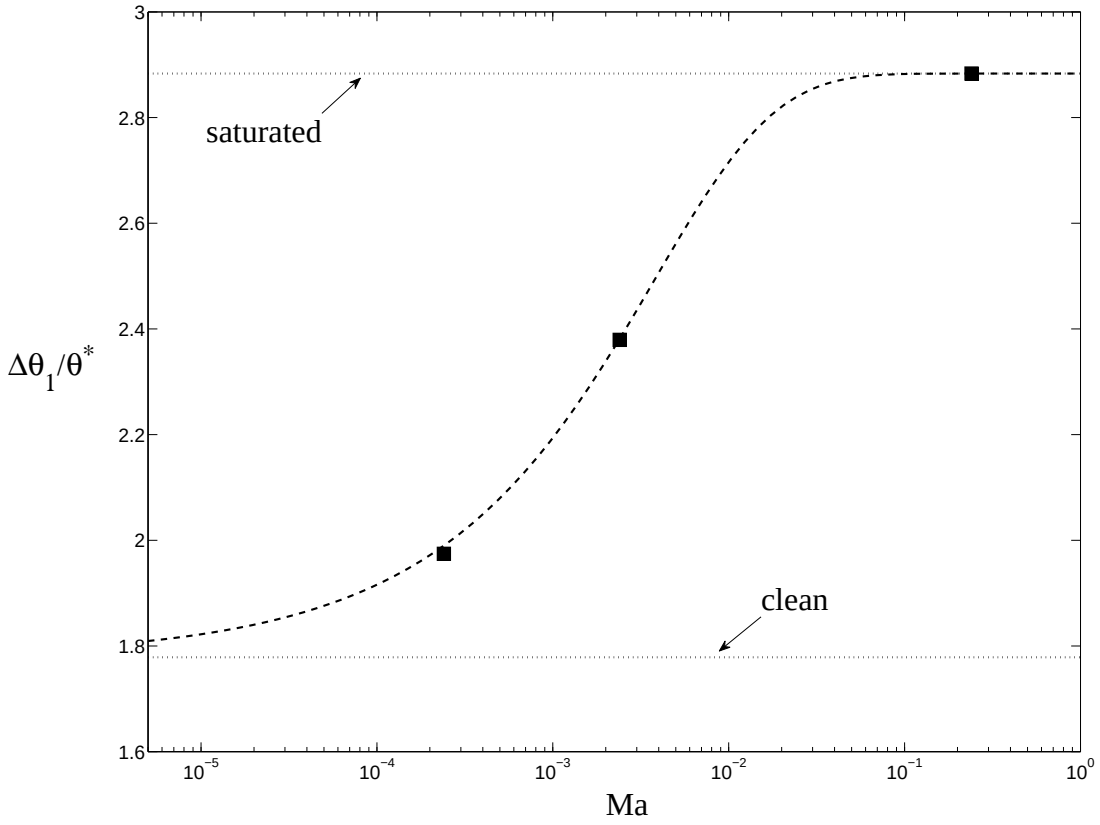

Figure 3.21: Non-dimensional surface-bulk temperature difference vs. Marangoni number. The curve is $\Delta\theta_1/\theta^* = tanh\left(12.5\sqrt{Ma}\right) \cdot (\Delta\theta_{sat}/\theta^* - \Delta\theta_{clean}/\theta^*) + \Delta\theta_{clean}/\theta^*$,where $\Delta\theta_{sat}$ and $\Delta\theta_{clean}$ are the temperature differences corresponding to the 'saturated' and 'clean' cases respectively.

In Handler et al.[73] it was found that a non-dimensional parameter expressing the ratio of elastic forces to inertial forces gives a measure of the degree to which surfactants may affect near surface turbulence dynamics. Here we define a turbulenceŰsurfactant parameter as below:

$$\beta_E = \frac{E\gamma_0}{\rho U^{*2} L^*} \tag{3.25}$$

where $E = d\sigma/d\gamma|_{\gamma=\gamma_0}$ is the surface elasticity. In essence, this is a modified inverse of a

Weber number, where surface tension is replaced by elasticity. In Figure 3.22 the relationship between the surface temperature and this parameter is also shown to be sigmoidal. This indicates that: (1) starting from a clean surface, β_E must be increased by about three orders of magnitude to achieve full saturation, and (2) full saturation is achieved for $\beta_E > O(1)$. It is interesting to note that this result is generally in good agreement with that of Handler et al. [14] [2003] in which fully turbulent open channel flow was subject to surface contamination.

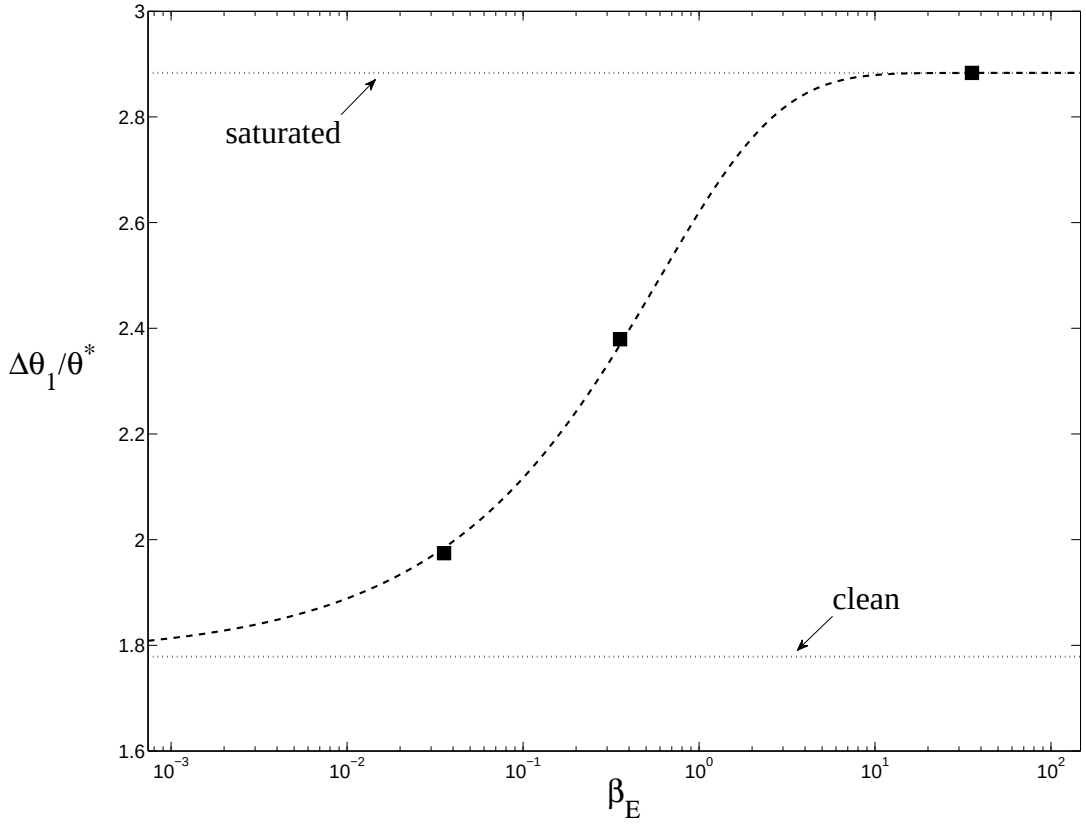

Figure 3.22: Non-dimensional surface-bulk temperature difference versus the turbulence-surfactant interaction parameter, $\beta_E = E/\left[\rho\,(U^*)^2\,L^*\right]$. The dotted curve is $\Delta\theta_1/\theta^* = tanh\left(\sqrt{\beta_E}\right)\cdot(\Delta\theta_{sat}/\theta^* - \Delta\theta_{clean}/\theta^*) + \Delta\theta_{clean}/\theta^*$.

3.3.7 Discussion of transient response to lumped parameter system

The temporal evolution of the mean surface temperature immediately after the imposition of the surfactant to the turbulent flow obtained in the 'clean' case, is shown in Figure 3.23 for surface elasticity values ranging from none to fully contaminated. It is evident, particularly in the case of the highest surfactant elasticity, that the surface temperature responds immediately to the imposition of a surfactant, and decreases roughly linearly in time for $t/t^* < 0.5$. It is seen that in the case of the highest surface elasticity, the surface temperature reaches a minimum at about $t/t^* \approx 1.2$, before rebounding and rising to a local maximum at $t/t^* \approx 3.4$. The surface temperature then appears to reach a statistically steady state for $t/t^* \approx 1.2$. A feature of some interest is the rebound of the surface temperature, which is most apparent in the highly contaminated case, which begins around $t/t^* \approx 1.2$. This behavior is certainly reminiscent of the response of a spring-mass-dashpot system, or more specifically, the position of the mass in such a system when started from a non-equilibrium state. This response is not surprising given the fact that the surfactant imparts elasticity to the surface, and also additional viscous dissipation associated with the terms $\partial u/\partial y$ and $\partial w/\partial y$, which would be zero in the clean case. A theoretical estimate of the precise natural frequency of this system, however, would require a model for the effective mass and rate of viscous dissipation for this system, which is beyond the scope of this work. In Figure 3.24, the details of initial response of the surface temperature are shown, and here we have added two runs (4 and 5) to the runs shown in Figure 3.23. It is evident from these results that the surface temperature for runs 4, 5, and 6 are not markedly different despite a one order of magnitude change in surface elasticity ($Ma = 0.24$ to $Ma = 0.024$). This indicates, first, that the response of the flow to surfactants is non-linear and secondly, that run 6 can very reasonably be considered saturated since along with surface elasticity increase from runs 4-6, the change in flow statistics is minimal.

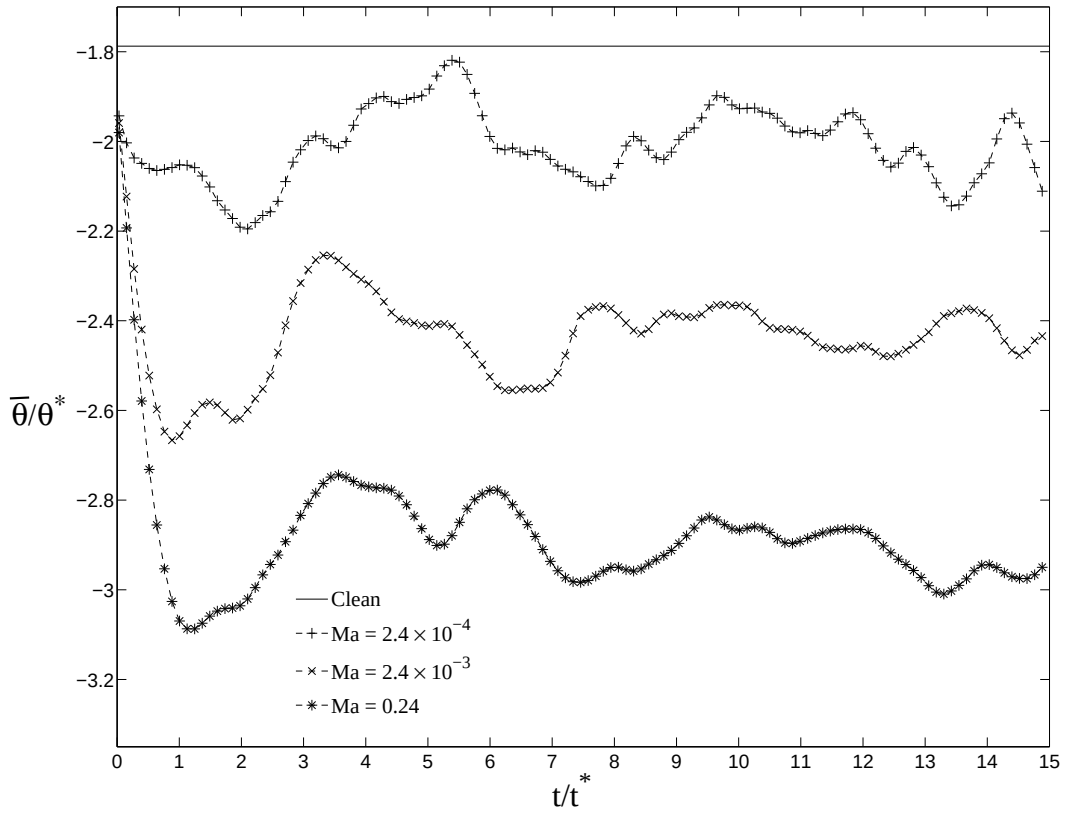

Figure 3.23: Temporal evolution of the mean (horizontally averaged) surface temperature, $\overline{\theta}$, for different surface elasticity. Each simulation was initialized with the same velocity and temperature field. Temperature and time scales θ^* and t^* are defined in Table 2.2.

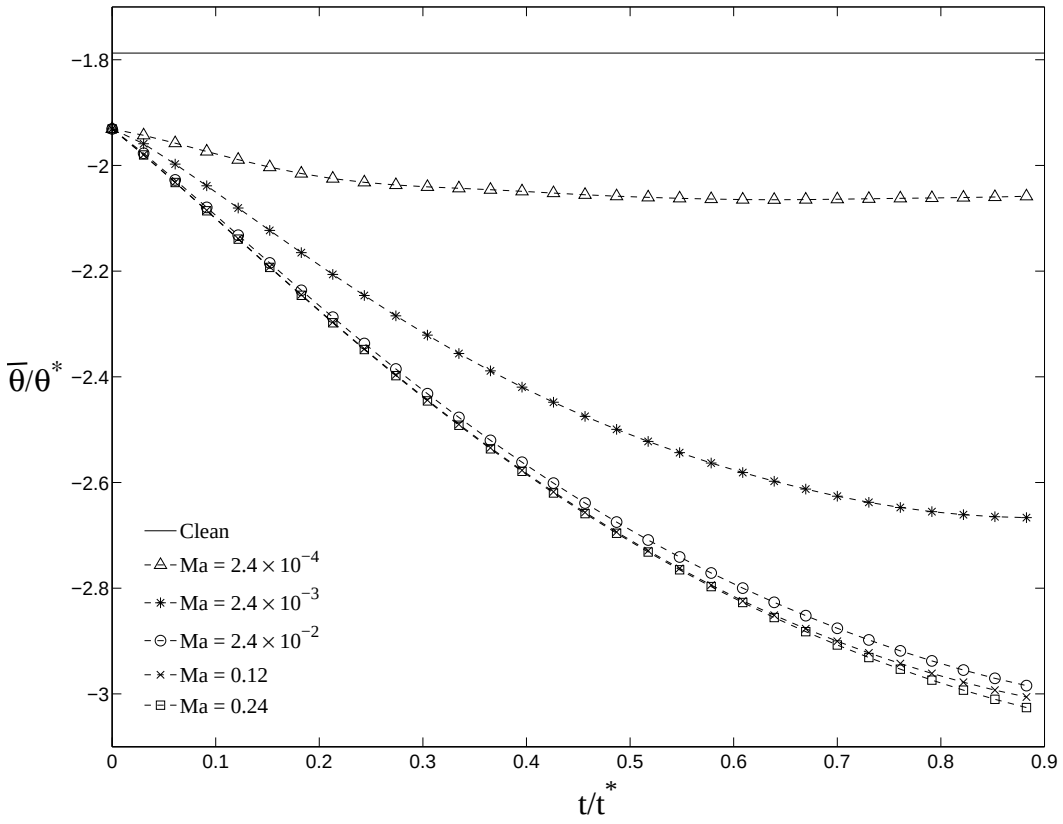

Figure 3.24: Details of the initial temporal evolution of the mean surface temperature. Here, the results of all six runs are shown.

4. ACTIVE SUPPRESSION OF BUOYANT CONVECTION BENEATH SURFACE*

4.1 Methodology

4.1.1 Definition and conventional measurements of gas transfer velocity

Transfer velocity of gas is defined as the ratio of flux density and concentration difference across the boundary layer,

$$k = \frac{j}{\Delta c} \tag{4.1}$$

where k has unit of m/s, j has unit of $m/s \cdot kg/m^3 = kg/s \cdot m^2$. For heat, a similar relation is $k_h = Q/\Delta T$, where Q has the unit of $J/s \cdot m^2$.

In conventional mass balance method, by the relation in Equation 4.1, transfer velocity is inferred from measurements of concentration variation of tracer in air and water. The volume and time average flux density is given by mass balance of the tracer concentration in a volume of water[9]

$$V_w c_w = F_w j \tag{4.2}$$

where F_w is the surface area of a well-mixed water body. Correspondingly the time constant $\tau_w = V_w/F_w k$ can be deduced to be commonly in the order of hours (wind/wave tunnels) to weeks (ocean)[9, 158]. The relatively long time scale of the traditional measurement technique of the transfer velocity is its main shortcoming, the reason of which is the limitation of the probe accuracy, as well as the turbulent mixing of water body. In other words, c_w here is the bulk averaged value which is taken within the horizontal and vertical span of V_w and F_w, which are all in relatively large scale, therefore finer discrimination and high accuracy are prohibited.

It is seen that in the conventional mass balance method using natural tracers, not only

* Data, results and discussion in sections 4.2, 4.3 are reprinted with permission from "Active suppression of buoyancy driven turbulence" by Qi Zhang, Robert A. Handler, (2014) *International Journal of Heat and Mass Transfer*, 75, 207-212, Copyright 2014 by Elsevier.

the measuring procedure is complicated and time consuming, but also the result is contaminated with sources and sinks other than surface gas exchange to lead error. The latter problem can be overcome by using artificially injected tracers[159, 160, 161]. Though, the response time of the mass balance method remains much too slow to yield a true and instantaneous parameterization of the gas exchange rate with the natural fluctuations and changes of the meteorology and the waves.

4.1.2 Fundamentals of the controlled flux method

Based on definition of the transfer velocity in Equation (4.1), the conventional methods determine the concentration differences first by either making use of passive tracer or imposing active tracer, then the flux density of the tracer is figured out. In an inversed manner, the controlled flux method predetermines the flux density by injecting tracer with controllable flux density, then it tries to measure the concentration difference between both sides of the interface.

The most convenient flux source is heat, which can be easily applied on water surface. In consequence, the surface temperature that reflects the heat transfer process beneath is easily measured. The validity of the analogy between heat and gas transfer is provided with below relationship[9]:

$$\frac{k_1}{k_2} = \left(\frac{D_1}{D_2}\right)^n \approx \left(\frac{Sc_1}{Sc_2}\right)^{-n} \tag{4.3}$$

Equation (4.3) basically says that molecular diffusion coefficient of heat and gas are proportional in water, therefore it is rational to expect that their transfer velocity is proportional too, since eddy diffusivity essentially boils done to molecular dissipation but on a greater scale of mixing.

A detailed demonstration of the controlled flux method is found in[9] in two separate approaches, both of them use heat as tracer and infrared laser for tracer injection. The first way is a square wave excitation. At first, assuming a heat transfer balance condition at

air-water interface, then, suddenly, the laser heating is imposed at water surface, which is equivalent to a net flux density increase at surface as certain ratio of heat is absorbed by water surface within $20\mu m$, and 97% of them are transferred further downwards across the aqueous boundary layer[9] due to the air-water interfacial heat transfer barrier. The heat flux balance is thus shifted due to this known net flux density, and the mean surface temperature in the area subject to injection is also shifted. Then, instead of obtaining subsurface mean temperature change, it is assumed that subsurface heat transfer is mainly constrained in viscous boundary layer, therefore laser heating is switched off for the inversed procedure to take place, that is, heat flux density is suddenly changed back. During the entire on-and-off cycle, the response of surface temperature shift and recovery is recorded, and the time scale of such a response under square excitation is analyzed, from where the direct concentration measurement is avoided yet the transfer velocity is deduced, through the following relationship[9].

Firstly, assume the viscous layer depth can be represented as:

$$z_* = \frac{D}{k} \tag{4.4}$$

assuming only molecular transport throughout the layer, which is roughly valid in the limited depth of 30 to 300 μm from the surface, because the diffusion coefficient of gaseous species in water is quite small(in other words, the Schmidt number $Sc = \nu/D$ is quite high), also because turbulence mixing decays towards surface.[9]. Therefore, the time constant is defined as

$$t_* = \frac{z_*}{k} = \frac{D}{k^2} \tag{4.5}$$

compared to mass balance method, Equation 4.5 has greatly reduced time scale to the order of seconds.

As is previously stated, from Equation 4.4, for a periodically on-off flux source, as

soon as j is known, and Δc is estimated from saturation point of on and off status, $k = j/\Delta c$ is obtained directly. Alternatively, k can be obtained using Equation (4.5) from the time constant roughly estimated from transient response duration after flux applied on the surface. Furthermore, for a sinusoidal flux source, the concentration can be calibrated through[9]

$$c = \frac{j}{(D\omega)^{1/2}} \tag{4.6}$$

where phase lag and amplitude damping can be used in concert to determine transfer velocity.

Compared to the conventional techniques, controlled flux method yields a much more detailed insight into the transfer processes across the free aqueous viscous boundary layer, it allows a local and instantaneous measurement of the transfer velocity and an investigation of the dynamic response of the transfer across the boundary layer.

4.1.3 Proposition of full suppression of turbulence

Controlled flux method suggests a new technique for gas flux measurement, the inspiring idea of actively heating up surface to gain signature of subsurface activity for gas flux measurement leads us to explore the possibility of further heating the surface to the degree of full suppression of subsurface convection. There are several initiatives to advance the study of such a novel approach:

(1) The suppression of subsurface convection eliminates the need of modeling convection layer, which usually involves surface renewal theory, or surface strain theory. In these theories, undetermined, conditional parameter still exists and the models are not yet closed. Indeed, in Jähne's study[9], these models were used to calibrate the measurement results.

(2) The suppression of subsurface convection has limited effect to surface heat flux. As is stated, surface heat flux is categorized in three types, latent heat flux, sensible heat

flux and radiation, and none of them will be significantly affected by surface heating in the amount of couple degrees of Kelvin ([9], Figure 4). As soon as the analogy of heat and gas preserves anywhere including viscous boundary layer and the bulk, the gas transfer velocity is approachable.

(3) The study is also related to the observation of formulation of warm layer at ocean surface and its cooling process. In ocean surface, once solar heating exceeds the combined cooling effects by turbulent scalar heat transfer and net longwave radiation, the main body of the mixed layer is cut off from its source of turbulence, to form a stratified warm layer[10].

4.2 Parameterization and implementation of radiation absorption of water

The heating of surface is realized in simulation in a way that, a volumetric heat source other than the compensation heat source described in section2.2.2 is added. The heat source is configured so that it varies along depth to resemble the absorption profile of radiation. Practically, such a radiation may stand for either laser, sunlight or anything else.

Imposition of the heating source starts from modification of Equation 2.26 to add up the additional term representing the heating source:

$$\frac{\partial \theta}{\partial t} + \vec{v} \cdot \nabla \theta = \alpha \nabla^2 \theta + \frac{s_0 + s_L}{\rho c_p} \tag{4.7}$$

where

$$s_0 = \frac{Q}{L_y} \tag{4.8}$$

is the compensation heat source and

$$s_L = \Phi \exp \frac{y}{\delta_p} \cdot \mathit{I}\,(t; \Delta t) \tag{4.9}$$

is the resembling heat source. Where

$$\mathcal{I}(t;\Delta t) \approx \begin{cases} 1 & : \frac{1}{2}\Delta t < t < \frac{3}{2}\Delta t \\ 0 & : otherwise \end{cases} \tag{4.10}$$

is responsible for resembling the switch-on-and-off action of the laser source, and is guaranteed smooth to avoid numerical issues by realization through combination of two hyperbolic tangent functions with adjustable scaling on magnitude and time for steepness and duration. The first $1/2\Delta t$ is left untouched intentionally to assure a steady, fully developed initial condition. Φ is the un-damped magnitude of radiation absorption, δ_p is the characteristic depth for absorption profile, which is called 'penetration depth' here.

After non-dimensionalization using Rayleigh scale (see section2.2.3), the heat source can be scaled as

$$\tilde{s}_L = \frac{\Phi L_y}{Q} \exp \frac{y L_y}{\delta_p} \cdot \mathcal{I}(t; \frac{\alpha}{L_y^2}\Delta t;) \tag{4.11}$$

The same scaling yields three non-dimensional numbers representing respectively the magnitude, the penetration depth, and the duration of the heating source. They are defined as

$$N_s = \frac{\Phi \delta_b l}{Q} \tag{4.12}$$

$$N_\delta = \frac{\delta_p}{\delta_{bl}} \tag{4.13}$$

$$N_\tau = \frac{\alpha \Delta t}{\delta_{bl}^2} \tag{4.14}$$

Here, the magnitude of the heating source is scaled with the original heat flux, which is assumed to be constant, the penetration depth is scaled with boundary layer thickness δ_{bl}, and the duration of heating is scaled with the diffusion scale in the boundary layer α/δ_{bl}^2.

The heating source is implemented with an additional subroutine to determine the vol-

umetric, temporal and spatial various heating source outside of the main solver, and the calculated number is fed to the main solver prior to solution process of Equation (2.27) through Equation (2.27).

4.3 Results and discussion

4.3.1 Suppression effectiveness and consecutive flow reaction

In Figure 4.1 the temporal response of the horizontal average of the surface temperature $\overline{\theta}$ is shown for a range of surface heat fluxes and source strengths, keeping all other dimensionless numbers fixed. In each case, once the statistically steady buoyancy driven turbulence is subject to volumetric surface heating,$\overline{\theta}$ is seen to rise (heating phase), followed by a fall (cooling phase) when the source is removed. For the larger source strengths, $N_s = 20, 10, 5$, we observe in most cases a subtle but clearly discernible change in slope $d\overline{\theta}/dt$ in the surface temperature during the cooling phase. For example, for $N_s = 5$ these 'events' or 'bumps' are evident at t $110s, 200s$,and $280s$ for $Q = 100W/m^2, 200W/m^2$, and $500W/m^2$ respectively. In the case of the weakest surface heating ($N_s = 2$) the surface temperature rise due to heating is still distinguishable from the random background thermal fluctuations associated with buoyancy induced turbulent motions.

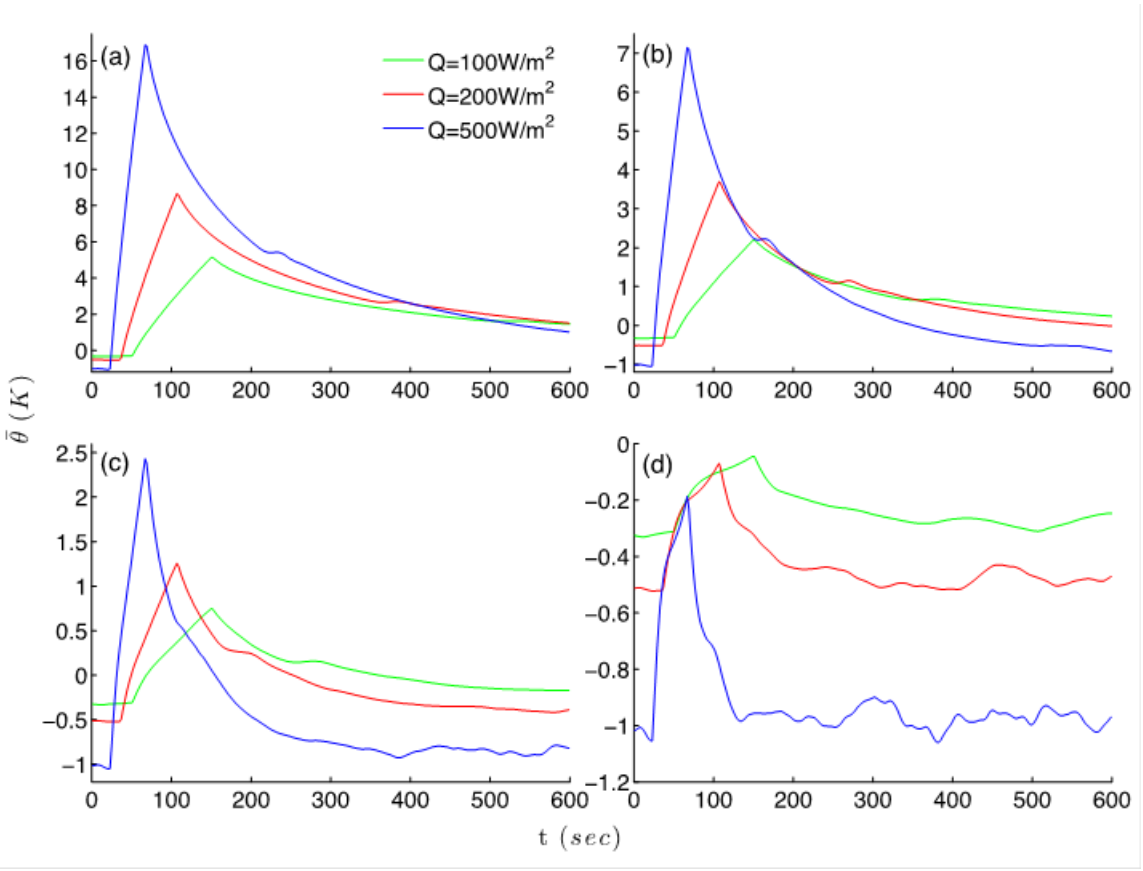

Figure 4.1: Horizontally averaged surface temperature during the heating and cooling phases. (a) $N_s = 20$, (b) $N_s = 10$, (c) $N_s = 5$, (d) $N_s = 2$. In each case, the surface temperature rises rapidly immediately after the heating source is turned on. The temperature then decays after reaching a maximum after the source is turned off.

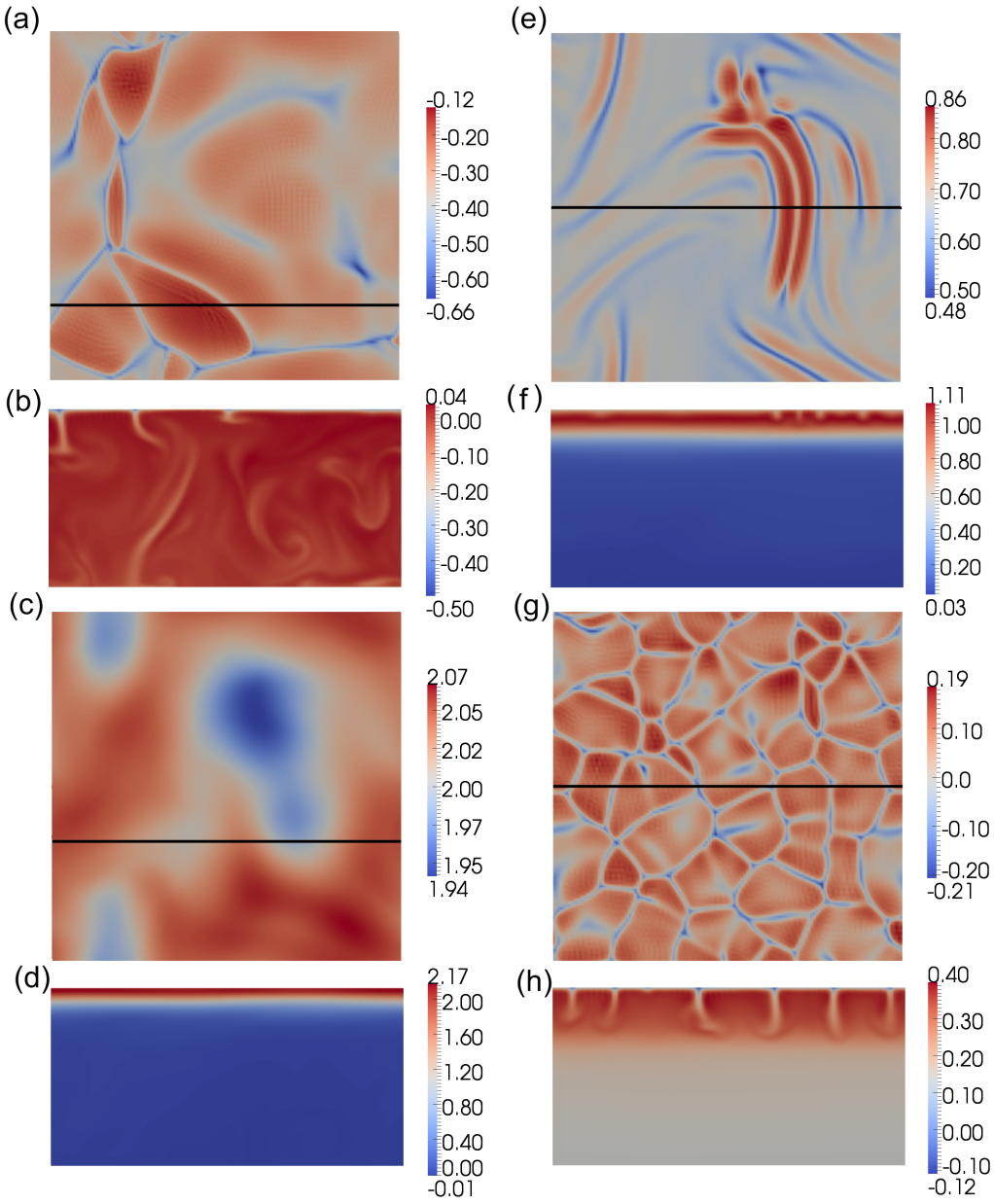

Figure 4.2: Instantaneous surface temperature in the x-z plane (a, c, e, g) and vertical temperature maps in the x-y plane (b, d, f, h). Here the entire computational domain is represented. The vertical maps are taken below the lines indicated in (a), (c), (e), and (g). Results are for $N_s = 10$, $Q = 100W/m^2$, and times given by (a, b) $t/t^* = 0$, (c, d) $t/t^* = 53.4$, (e, f) $t/t^* = 113.5$ and (g, h) $t/t^* = 260.3$. Here $L_y = 11.713cm$ and time t is made non-dimensional by t^*.

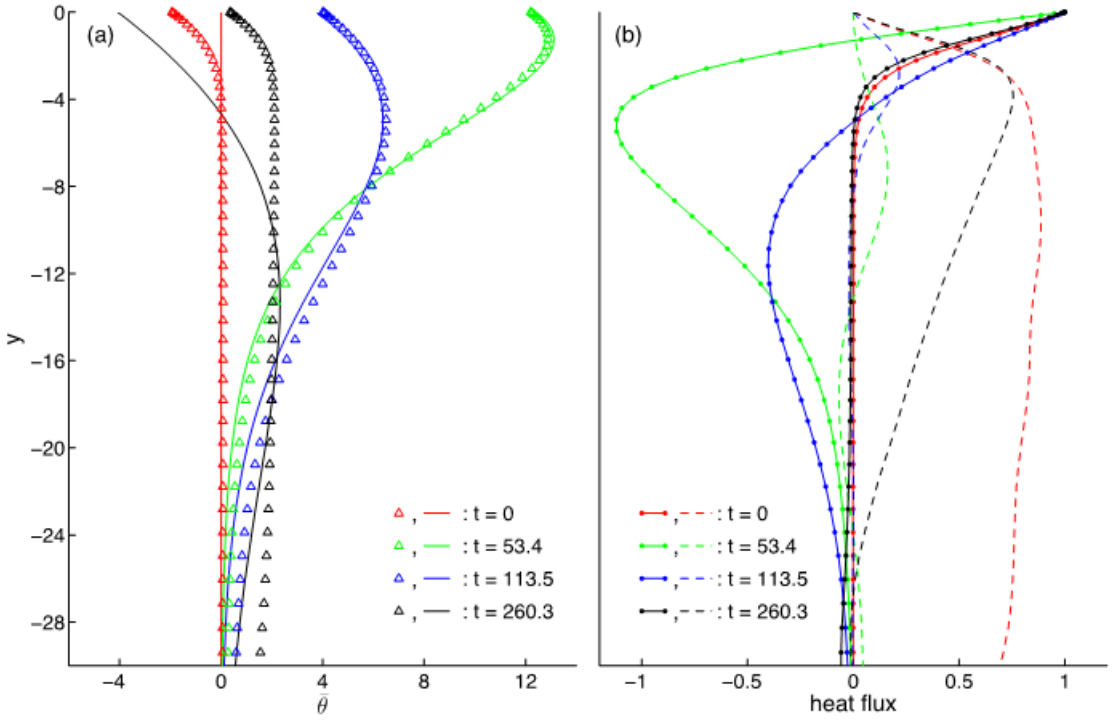

Figure 4.3: Vertical profiles of the horizontally averaged temperature (a) and heat fluxes (b) at various times during the heating and cooling phases for $N_s = 10$, $Q = 100W/m^2$. In (a) triangles represent simulation results and solid lines represent the analytical conduction solution. In (b) the dotted line is $-\left(d\bar{\theta}/dy\right)/\left(Q/k\right)$ and dashed line is the convective flux $\overline{v'\theta'}/\left(Q/\rho c\right)$. Here v' is the fluctuating vertical (y-directed) velocity and θ' is the fluctuating temperature.

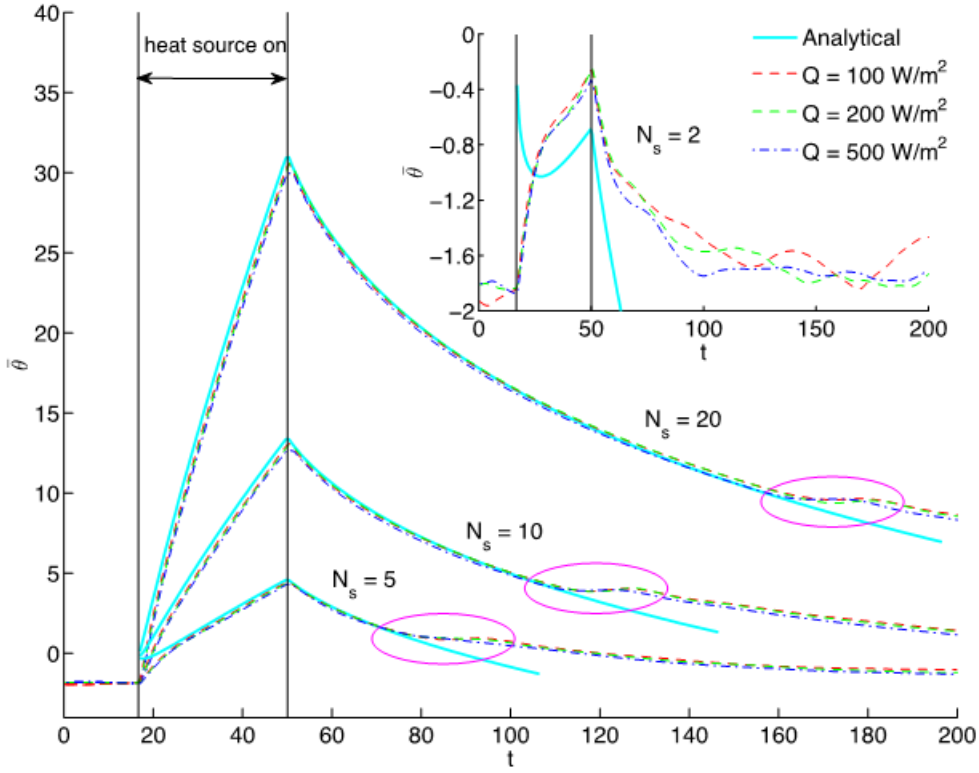

Figure 4.4: Horizontally averaged surface temperature versus time compared with the analytical conduction solution given by Equation (4.17). Convection cells are found to reform at times corresponding to the circled regions. The inset plot gives results for $N_s = 2$.

A more detailed view of the thermal response of the surface can be obtained by visualizing the instantaneous temperature fields at and below the surface at various times during and after surface heating. These thermal patterns are shown in Figure 4.2 for $N_s = 10, Q = 100 W/m^2$ at four time instants. The temperature pattern at $t/t^* = 0$, before the heat source has been applied, indicates the presence of buoyancy driven turbulence in which the cool thin bands at the surface correspond to regions in which surface fluid sinks into the interior. Larger regions of warm fluid on the surface correspond to fluid from

below impacting the surface. The thermal structure at the instant the heat source has been turned off at $t/t^* = 53.4$, is shown in Figure 4.2(c,d). Here it is evident that the clearly delineated surface cells seen in Figure 4.1(a) have become diffuse regions as shown in Figure 4.2(c). A thick warm region overlaying a cooler region is seen in Figure 4.2(d), and the initial buoyancy driven turbulence is no longer apparent. The thermal structure in the cooling phase just before the warm 'bump' in the surface temperature at $t/t^* = 113.5$ (see Figure 4.4) is shown in Figure 4.2(e,f). Numerous linear, streaky thermal patterns are seen on the surface in Figure 4.2(e). A vertical temperature slice shown in Figure 4.2(f) shows distinct downwelling of cold fluid corresponding to these linear features, though vigorous turbulent mixing is clearly absent. Later, at $t/t^* = 260.3$ (Figure 4.2(g,h)) the linear features seen previously have evolved into distinct thermal cells, smaller in size than the initial cells seen in Figure 4.2(a), with some cells forming polygonal shapes.

Greater insight into these processes can be obtained by studying the instantaneous horizontal average of the temperature, $\overline{\theta}(y,t)$, and the conductive ($d\overline{\theta}/dy$) and convective ($\overline{v'\theta'}$) thermal flux profiles, where v' and θ' are the fluctuating vertical velocity and temperature respectively. These are shown in Figure 4.3. The mean temperature profile at $t/t^* = 0$ shows a well-defined thin cool region near the surface, sometimes referred to as a 'cool-skin' layer[2, 6]. The flow at $t/t^* = 0$ is in a statistically steady state so that the outgoing heat flux at the surface is exactly balanced by an upward (positive) convective buoyancy induced thermal flux, as indicated in Figure 4.2(b). At the end of the heating phase ($t/t^* = 53.4$) the surface temperature has increased significantly, and though a cool surface layer still exists, the temperature profile now has a subsurface maximum at $y = -1.2477$. More importantly, we observe in Figure 4.3(b) that the convective flux has been much reduced. This corresponds well with the observed near absence of turbulence seen in Figure 4.2(d), indicating that surface heating has been sufficient to suppress surface turbulence. At $t/t^* = 113.5$ we again see a subsurface temperature maximum at

$y = -4.9302$. However, the convective flux has reemerged and is positive in the region $y > -7.5$. This is compatible with the re-development of the streaky instabilities described in Figure 4.2(d,e). Finally, at $t/t^* = 260.3$ the temperature profile has lost its subsurface maximum, and the convective flux has increased to a peak magnitude nearly the same as that at $t/t^* = 0$. This, along with the complex thermal structure seen in Figure 4.2(g,h) indicates that flow has returned to nearly the fully developed turbulence seen at $t/t^* = 0$.

The scaling given above in section 2.2.3 indicates that the dimensionless parameters N_s,N_τ,N_δ,Ra_q, and Pr govern the problem. However, since the Rayleigh numbers used here are large, we can expect that the flow should be relatively insensitive to it. As a result, with N_δ,N_τ, and Pr fixed, we should expect that the surface temperature versus time scaled, by θ^* and t^* should depend on N_s alone. From Figure 4.4 it is clear that this is the case. Also shown in Figure 4.4 is a comparison between the conduction solution and the simulations. The agreement is shown to be excellent for $N_s = 20, 10, 5$ with the exception of a brief period right after the heat source is turned on, and for the period subsequent to the 'bump' feature. This should be expected since very early in time convective turbulence still exists, whereas near and subsequent to the 'bump' feature, convective instabilities have reemerged. For $N_s = 2$ the agreement is poor as we would expect since in this case the heat source strength is apparently insufficient to suppress surface turbulence.

4.3.2 Conduction approximation model and corresponding analytical solution of mean surface temperature

This observed suppression of turbulence suggests that a model based on pure conduction can be used to predict the response of the surface temperature to heating. We also note that $L_y/\delta_{bl} \sim Ra_q^{1/4} \sim 10^2$ for the Rayleigh numbers chosen, signifying that the nominal thickness of the thermal boundary is much larger than the domain height in our

simulations. This leads us to consider a one-dimensional, semi-infinite model given by:

$$\frac{\partial\theta}{\partial t} = \alpha\frac{\partial^2\theta}{\partial y^2} + \Phi\exp\frac{y}{\delta_p}[H(t) - H(t-\tau)] \tag{4.15}$$

where $H(t)$ is the Heaviside function, with boundary condition

$$\frac{\partial\theta}{\partial y}|_{y=0} = -\frac{Q}{k}, \theta(y\to-\infty) = 0 \tag{4.16}$$

and initial condition $\theta(y=0, t=0) = 0$

The model stated above is analytically soluble, with the help of Laplace transformation. The complete solution in time space is

$$\begin{aligned}
\theta(y,t) = &\left(-\frac{Q}{k} + \frac{\Phi\zeta}{\gamma}\right)\left(\sqrt{\frac{4\alpha t}{\pi}}e^{-\frac{y^2}{4\alpha t}} + y\cdot erfc\left(-\frac{y}{\sqrt{4\alpha t}}\right)\right)\\
&- \frac{\Phi\zeta}{\gamma}\cdot\frac{1}{2}e^{\gamma t}\sqrt{\frac{\alpha}{\gamma}}\left[e^{\sqrt{\frac{\gamma}{\alpha}}y}efrc\left(-\frac{y}{\sqrt{4\alpha t}} - \sqrt{\gamma t}\right) - e^{-\sqrt{\frac{\gamma}{\alpha}}y}efrc\left(-\frac{y}{\sqrt{4\alpha t}} + \sqrt{\gamma t}\right)\right]\\
&+ \frac{\Phi}{\gamma}e^{\zeta y}\left(e^{\gamma t} - 1\right) + \mathcal{H}(t-\tau)\cdot\left\{-\frac{\Phi\zeta}{\gamma}\left(\sqrt{\frac{4\alpha\hat{t}}{\pi}}e^{-\frac{y^2}{4\alpha\hat{t}}} + y\cdot erfc\left(-\frac{y}{\sqrt{4\alpha\hat{t}}}\right)\right)\right.\\
&+ \frac{\Phi\zeta}{\gamma}\cdot\frac{1}{2}e^{\gamma\hat{t}}\sqrt{\frac{\alpha}{\gamma}}\left[e^{\sqrt{\frac{\gamma}{\alpha}}y}efrc\left(-\frac{y}{\sqrt{4\alpha\hat{t}}} - \sqrt{\gamma\hat{t}}\right) - e^{-\sqrt{\frac{\gamma}{\alpha}}y}efrc\left(-\frac{y}{\sqrt{4\alpha\hat{t}}} + \sqrt{\gamma\hat{t}}\right)\right]\\
&\left.-\frac{\Phi}{\gamma}e^{\zeta y}\left(e^{\gamma\hat{t}} - 1\right)\right\}
\end{aligned} \tag{4.17}$$

where $\zeta = 1/\delta_p$ and $\gamma = \alpha\zeta^2$.

There are several discrepancies between the model and the numerical simulation configuration, making the model an approximated approach to the problem. Though, Figure 4.4 as well as analysis in section 4.3.1 indicates that the model approximation is of high accuracy. These discrepancies and their effects are stated and analyzed as below:

(1) The model is based on the assumption that subsurface turbulence is immediately

deactivated, i.e., the initial condition of velocity for the model solution is zero. The fact that this approximation yields good results suggests that, firstly, previous fully developed convection turbulence is rather weak, with low kinematic energy, and secondly, vertical advection and circulation is almost immediately erased after heating source is applied. Otherwise, the inertial of advection would deviate the conduction modal solution from simulation result in the first place.

(2) The model is based on the assumption that the surface cool skin profile (see Figure 3.18) is negligible in the sense of total heat of the volume, i.e., the initial condition of temperature is uniform throughout the domain. Under strong heating source, this is a reasonable approximation, verified through Figure 3.18, where, for the comparable volume with penetration depth greater boundary layer thickness, i.e., $N_\delta = 4.386$, the temperature rise after applying heat source is about one order of magnitude greater than cool skin temperature difference.

(3) Furthermore, the constant source s_0 which is included in the numerical simulations is eliminated in the model, since it can be shown that $s/Q \sim 10^{-2}$ for strong surface heating.

(4) The domain depth in the model is assumed to be infinite. Firstly, since $L_y/\delta_{bl} \sim Ra_q^{1/4} \sim 10^2$ for the Rayleigh numbers chosen, it is quite reasonable to make such an approximation. Secondly, the semi-infinite domain is more realistic concerning the original problem of ocean surface convection, under the circumstance, the finite setup of numerical simulation itself becomes an approximation. Finally, semi-infinite domain offers good mathematical convenience in obtaining analytical solution.

4.3.3 Preliminary statement of linear instability analysis

During the cooling phase a noticeable rise in surface temperature, which we call a 'bump', is observed. This bump feature was found to mark the transition from pure conduction to buoyant convection. The mechanism by which this process takes place requires

some consideration. A complete explanation would certainly require at the very least, the determination of the stability of the vertical temperature profiles during the various stages of surface heating and cooling. Such an analysis would need to consider both the linear and nonlinear aspects of the problem, as well as the existence of a temporally varying temperature profile. Such an analysis is well beyond the scope of this work. On the other hand, a heuristic explanation based on classical analyses[124, 125] seems possible. During surface heating the vertical temperature profile is seen to exhibit a subsurface maximum. Thus a convectively stable temperature profile exists below this maximum and we can expect and indeed observe turbulence suppression. However, an unstable profile exhibits in the region between this maximum and the surface as a consequence of the constant outward heat flux. In this region it is appropriate to define a Rayleigh number as $Ra_T = g\beta\Delta T L^3/\alpha\nu$ where ΔT is the temperature difference between the subsurface maximum and the top boundary, and L is the distance between the surface and the subsurface maximum. It can therefore be anticipated that the stability of the flow in this region will depend on the size of this Rayleigh number. We find that at $t/t^* = 53.4$, at the end of surface heating, that $Ra_T = 4.6557$ compared to $Ra_T = 1058.1$ before the 'bump' feature at $t/t^* = 113.5$. Linear stability analyses[124, 118] show that the critical Rayleigh numbers are about 103, which compares favorably with our value right before the 'bump' feature. This indicates that during the heating process, Ra_T falls below a critical value and thus turbulence is suppressed both above and below the subsurface temperature maximum. During the cooling phase both ΔT and L increase giving rise to the convection cells observed initially at $t/t^* = 113.5$.

5. CONCLUSION AND FUTURE WORKS

5.1 Conclusion

In order to determine the effects of surfactant on the turbulence beneath a free, smooth surface subject to an outgoing heat flux, with emphasis on the nature of the temperature field at the interface, direct numerical simulations based on a fully spectral code were used to investigate the evolution of the velocity, temperature, and surfactant concentration. The standard Boussinesq approximation was employed to model buoyancy effects. An idealized model was chosen in which the surface was subject to zero external shear, the surface was assumed to be undeformed, the surfactant was assumed to be insoluble, and the Rayleigh number was fixed.

It was determined that as surface elasticity increases from a clean state to a fully contaminated state, that the major quantitative effects of surfactant in the cases investigated here are:

(1) A decrease in mean surface temperature by $0.2°C$ assuming a heat flux of $100W/m^2$ and a Rayleigh number of 4.45×10^8 in water.

(2) An increase in the thermal boundary layer thickness by 35%.

(3) A decrease in the Nusselt number by as much as 43%.

In addition, images of the surface temperature fields and subsequent Fourier analysis of these fields, revealed that as surface elasticity increases, the spectral energy density in the inertial region of the spectrum increases, while decreasing at the highest wavenumbers. The decrease in spectral energy at the highest wavenumbers is not unexpected, since surfactants would be expected to increase viscous dissipation at these scales. In fact this result corresponds reasonably well with recent experiments in which IR imagery was employed. The increase of spectral density at inertial, or mid-band wavenumbers, was some-

what unexpected, and at present there appears to be no obvious explanation for this. A turbulence-surfactant interaction parameter, β_E, was defined as the ratio of elastic to inertial forces. It was found that there is a sigmoidal relationship between this parameter and the average surface temperature, and that starting from a clean surface, β_E must be increased by about three orders of magnitude to achieve full saturation. It is found that full saturation is achieved for $\beta_E > O(1)$.

Finally, we performed flow visualizations of the surface thermal and velocity fields to elucidate the nature of the cold core vortices that are often observed in experiments in this flow. The visualizations reveal the likelihood that these vortices are caused by instabilities of the flow in the vicinity of the narrow cold bands associated with downwelling fluid. For example, any randomly generated differential in the velocity component parallel to a cold band, which would be associated with vertical (y-oriented) vorticity, will be amplified by a downwelling due to the vortex stretching effect. If the shear across the cold band and the downwelling are strong enough, a region of more intense, concentrated vorticity may result. Such vortices are unlikely to form near warm upwellings since vertically oriented vorticity will be reduced in these regions by virtue of vortex compression. It is interesting to note that no warm core vortices have ever been observed in these flows, either in these or other direct numerical simulation or in experiments.

In the turbulence suppression study, it has been shown that surface heating can almost entirely suppress buoyancy induced turbulent convection at an interface free of shear. The problem can be entirely characterized by five dimensionless parameters. Three of these characterize the strength, penetration depth, and time duration of the heat source, the other two being the Prandtl and Rayleigh numbers. We find that the turbulence can be almost entirely eliminated when the source is of sufficient strength, depth, and duration. In cases where the turbulence has been suppressed, a one-dimensional conduction model is found to accurately describe the temporal response of the surface temperature during the heating

and cooling phases. During the cooling phase a noticeable rise in surface temperature, which we call a 'bump', is observed. This 'bump' feature was found to mark the transition from pure conduction to buoyant convection. The mechanism by which this process takes place requires some consideration. Furthermore, the outgoing heat flux can readily be estimated by comparing the evolution of the observed surface temperature with a pure conduction model.

We suggest that for these observations to be useful in either laboratory or field settings, laboratory based verification is needed. This can now be accomplished by using high sensitivity IR imagers[21, 22, 23] in conjunction with detailed subsurface flow measurements via digital particle velocimetry. It is important to keep in mind that while surface heating can suppress buoyancy driven turbulence, it may modify, but might not suppress shear driven turbulence.

5.2 Future works

Numerical simulations especially spectral schemes have achieved notable success in multiple aspects including accuracy and efficiency. Nevertheless, the limitations include the difficulty in simulating interfacial flows at high Reynolds, Schmidt, and Prandtl numbers, and also in simulating deformed surface, for example, wave breaking. At present, in the high Reynolds number simulations, LES (Large-eddy-simulations) still remains a practical approach. The smallest unresolvable scales of motion still have to be modeled other than directly computed, based on pure imperical, ad-hoc models. In simulating the gently deformed surface, a noticeable work have been done[110, 111] to map the curved physical space to Cartesian coordinates, where spectral solver is employed. In this mathematically and numerically effort-consuming approach, moderately deformed surfaces can be tackled with, although strong deformation from breaking waves to multi-phase flows are still challenging problems. Indeed, pure numerical improvement is not an ultimate solution in any sense, and physical modeling is always necessary. In this sense, a possi-

ble future work is likely to explore the possibility of incoorperating the two most popular models, surface renewal model and surface straining model, to the spectral method, so as to model the small scale breaking-wavelet, bubbles and sprays at interface, instead of solving them directly.

In the study, other suggested directions of the future work may include modeling the surfactant with non-linear elasticity, simulating the surfactant effects in a shear driven flow, exploring the surfactant-wave interaction on wavy surface and shear driven turbulence, exploring the untouched parameter space of the active heating problem, simulating a 3-D heated spot evolution at free surface, and exploring heating suppression of the shear driven turbulence.

REFERENCES

[1] P. S. Liss and L. Merlivat, "Air-sea gas exchange rates: Introduction and synthesis," in *The Role of Air-Sea Exchange in Geochemical Cycling* (P. Buat-Ménard, ed.), ch. 3, pp. 113–127, Netherlands: Springer, 1 ed., 1986.

[2] P. M. Saunders, "The temperature at the ocean-air interface," *Journal of the Atmospheric Sciences*, vol. 24, no. 3, pp. 269–273, 1967.

[3] O. M. Phillips, "On the generation of waves by turbulent wind," *Journal of Fluid Mechanics*, vol. 2, no. 05, pp. 417–445, 1957.

[4] J.-T. Jeong and H. Moffatt, "Free-surface cusps associated with flow at low reynolds number," *Journal of Fluid Mechanics*, vol. 241, no. 1, pp. 1–22, 1992.

[5] C. Zappa, W. Asher, and A. Jessup, "Microscale wave breaking and air-water gas transfer," *Journal of Geophysical Research: Oceans*, vol. 106, no. C5, pp. 9385–9391, 2001.

[6] R. Leighton, G. Smith, and R. Handler, "Direct numerical simulations of free convection beneath an air–water interface at low Rayleigh numbers," *Physics of Fluids*, vol. 15, no. 10, pp. 3181–3193, 2003.

[7] T. Sarpkaya, "Vorticity, free surface, and surfactants," *Annual Review of Fluid Mechanics*, vol. 28, no. 1, pp. 83–128, 1996.

[8] D. Walker, R. Leighton, and L. O. Garza-Rios, "Shear-free turbulence near a flat free surface," *Journal of Fluid Mechanics*, vol. 320, pp. 19–52, 1996.

[9] B. Jähne, P. Libner, R. Fischer, T. Billen, and E. Plate, "Investigating the transfer processes across the free aqueous viscous boundary layer by the controlled flux method," *Tellus B*, vol. 41, no. 2, pp. 177–195, 1989.

[10] C. Fairall, E. F. Bradley, J. Godfrey, G. Wick, J. B. Edson, and G. Young, "Cool-skin and warm-layer effects on sea surface temperature," *Journal of Geophysical Research*, vol. 101, no. C1, pp. 1295–1308, 1996.

[11] X. Qiu and K. Xia, "Viscous boundary layers at the sidewall of a convection cell," *Physical Review E*, vol. 58, no. 1, pp. 486–491, 1998.

[12] G. Marmorino, G. Smith, and G. Lindemann, "Infrared imagery of large-aspect-ratio langmuir circulation," *Continental Shelf Research*, vol. 25, no. 1, pp. 1–6, 2005.

[13] G. Marmorino and G. Smith, "Reduction of surface temperature in ocean slicks," *Geophysical Research Letters*, vol. 33, no. 14, pp. L14603–1–5, 2006.

[14] S. Phongikaroon, K. P. Judd, G. B. Smith, and R. A. Handler, "The thermal structure of a wind-driven reynolds ridge," *Experiments in Fluids*, vol. 37, no. 2, pp. 153–158, 2004.

[15] J. Schnieders, C. Garbe, W. Peirson, G. Smith, and C. Zappa, "Analyzing the footprints of near-surface aqueous turbulence: An image processing-based approach," *Journal of Geophysical Research: Oceans*, vol. 118, no. 3, pp. 1272–1286, 2013.

[16] C. Chickadel, S. A. Talke, A. R. Horner-Devine, and A. T. Jessup, "Infrared-based measurements of velocity, turbulent kinetic energy, and dissipation at the water surface in a tidal river," *Geoscience and Remote Sensing Letters, IEEE*, vol. 8, no. 5, pp. 849–853, 2011.

[17] R. Handler, K. Housiadas, and A. Beris, "Karhunen-Loéve representations of turbulent channel flows using the method of snapshots," *International Journal for Numerical Methods in Fluids*, vol. 52, no. 12, pp. 1339–1360, 2006.

[18] A. Jessup, C. Zappa, M. Loewen, and V. Hesany, "Infrared remote sensing of breaking waves," *Nature*, vol. 385, no. 6611, pp. 52–55, 1997.

[19] A. Jessup, C. Zappa, and H. Yeh, "Defining and quantifying microscale wave breaking with infrared imagery," *Journal of Geophysical Research*, vol. 102, no. C10, pp. 23145–23153, 1997.

[20] G. B. Smith, R. A. Handler, and N. Scott, "Observations of the structure of the surface temperature field at an air-water interface for stable and unstable cases," in *Transport at the Air-Sea Interface* (C. S. Garbe, R. A. Handler, and B. Jähne, eds.), ch. 4, pp. 205–222, Berlin: Springer, 1 ed., 2007.

[21] R. Handler, G. Smith, and R. Leighton, "The thermal structure of an air–water interface at low wind speeds," *Tellus A*, vol. 53, no. 2, pp. 233–244, 2001.

[22] R. A. Handler and G. B. Smith, "Statistics of the temperature and its derivatives at the surface of a wind-driven air-water interface," *Journal of Geophysical Research: Oceans*, vol. 116, no. C06021, pp. 1–14, 2011.

[23] R. A. Handler, I. Savelyev, and M. Lindsey, "Infrared imagery of streak formation in a breaking wave," *Physics of Fluids*, vol. 24, no. 12, pp. 121701–1–7, 2012.

[24] A. Bentamy, K. B. Katsaros, A. M. Mestas-Nuñez, W. M. Drennan, E. B. Forde, and H. Roquet, "Satellite estimates of wind speed and latent heat flux over the global oceans," *Journal of Climate*, vol. 16, no. 4, pp. 637–656, 2003.

[25] R. Sureshkumar, A. N. Beris, and R. A. Handler, "Direct numerical simulation of the turbulent channel flow of a polymer solution," *Physics of Fluids*, vol. 9, no. 3, pp. 743–755, 1997.

[26] R. Handler, E. Levich, and L. Sirovich, "Drag reduction in turbulent channel flow by phase randomization," *Physics of Fluids A: Fluid Dynamics*, vol. 5, no. 3, pp. 686–694, 1993.

[27] K. B. Katsaros, W. T. Liu, J. Businger, and J. E. Tillman, "Heat transport and thermal structure in the interfacial boundary layer measured in an open tank of water in

turbulent free convection," *Journal of Fluid Mechanics*, vol. 83, no. 2, pp. 311–335, 1977.

[28] K. B. Katsaros, "Radiative sensing of sea surface temperature," in *Air-sea Interaction: Instruments and Methods* (F. Dobson, L. Hasse, and R. Davis, eds.), ch. 3, pp. 293–318, NY: Plenum Press, 1 ed., 1980.

[29] C. S. Garbe, H. Spies, and B. Jähne, "Estimation of surface flow and net heat flux from infrared image sequences," *Journal of Mathematical Imaging and Vision*, vol. 19, no. 3, pp. 159–174, 2003.

[30] J. M. Kaihatu, R. A. Handler, G. O. Marmorino, and L. K. Shay, "Empirical orthogonal function analysis of ocean surface currents using complex and real-vector methods," *Journal of Atmospheric & Oceanic Technology*, vol. 15, no. 4, pp. 927–941, 1998.

[31] C. S. Garbe, R. A. Handler, and B. Jähne, *Transport at the Air-sea Interface: Measurements, Models and Parametrizations*. NY: Springer, 1 ed., 2007.

[32] C. Paulson and J. Simpson, "The temperature difference across the cool skin of the ocean," *Journal of Geophysical Research: Oceans*, vol. 86, no. C11, pp. 11044–11054, 1981.

[33] C. Fairall, E. F. Bradley, J. Hare, A. Grachev, and J. Edson, "Bulk parameterization of air-sea fluxes: Updates and verification for the coare algorithm," *Journal of Climate*, vol. 16, no. 4, pp. 571–591, 2003.

[34] K. P. Judd, G. B. Smith, R. A. Handler, and A. Sisodia, "The thermal signature of a low reynolds number submerged turbulent jet impacting a free surface," *Physics of Fluids*, vol. 20, no. 11, pp. 115102–1–14, 2008.

[35] S. D. Smith, "Coefficients for sea surface wind stress, heat flux, and wind profiles as a function of wind speed and temperature," *Journal of Geophysical Research: Oceans*, vol. 93, no. C12, pp. 15467–15472, 1988.

[36] A. K. Prasad and P. Gonuguntla, "Turbulence measurements in nonpenetrative thermal convection," *Physics of Fluids*, vol. 8, no. 9, pp. 2460–2470, 1996.

[37] R. A. Handler, R. P. Mied, T. E. Evans, and T. F. Donato, "Convergence fronts in tidally forced rotating estuaries," *Journal of Geophysical Research: Oceans*, vol. 106, no. C11, pp. 27145–27162, 2001.

[38] C. D. Dimitropoulos, R. Sureshkumar, A. N. Beris, and R. A. Handler, "Budgets of reynolds stress, kinetic energy and streamwise enstrophy in viscoelastic turbulent channel flow," *Physics of Fluids*, vol. 13, no. 4, pp. 1016–1027, 2001.

[39] R. Handler, T. Swean, R. Leighton, and J. Swearingen, "Length scales and the energy balance for turbulence near a free surface," *AIAA Journal*, vol. 31, no. 11, pp. 1998–2007, 1993.

[40] G. Webber, R. Handler, and L. Sirovich, "Energy dynamics in a turbulent channel flow using the Karhunen-Loéve approach," *International Journal for Numerical Methods in Fluids*, vol. 40, no. 11, pp. 1381–1400, 2002.

[41] D. G. Dommermuth, "The laminar interactions of a pair of vortex tubes with a free surface," *Journal of Fluid Mechanics*, vol. 246, pp. 91–91, 1993.

[42] R. P. Mied, R. A. Handler, and T. F. Donato, "Regions of estuarine convergence at high rossby number: A solution in estuaries with elliptical cross sections," *Journal of Geophysical Research: Oceans*, vol. 107, no. C11, pp. 27–1–9, 2002.

[43] G. B. Smith, R. Volino, R. Handler, and R. Leighton, "The thermal signature of a vortex pair impacting a free surface," *Journal of Fluid Mechanics*, vol. 444, no. 1, pp. 49–78, 2001.

[44] M. Osborne, "The effect of convergent and divergent flow patterns on infrared and optical radiation from the sea," *Deutsche Hydrografische Zeitschrift*, vol. 18, no. 1, pp. 1–25, 1965.

[45] G. Csanady, "The role of breaking wavelets in air-sea gas transfer," *Journal of Geophysical Research: Oceans*, vol. 95, no. C1, pp. 749–759, 1990.

[46] S. Banerjee, D. Lakehal, and M. Fulgosi, "Surface divergence models for scalar exchange between turbulent streams," *International Journal of Multiphase Flow*, vol. 30, no. 7, pp. 963–977, 2004.

[47] A. J. Wells, C. Cenedese, J. T. Farrar, and C. J. Zappa, "Variations in ocean surface temperature due to near-surface flow: straining the cool skin layer," *Journal of Physical Oceanography*, vol. 39, no. 11, pp. 2685–2710, 2009.

[48] P. Danckwerts, "Significance of liquid-film coefficients in gas absorption," *Industrial & Engineering Chemistry*, vol. 43, no. 6, pp. 1460–1467, 1951.

[49] W. T. Liu and J. A. Businger, "Temperature profile in the molecular sublayer near the interface of a fluid in turbulent motion," *Geophysical Research Letters*, vol. 2, no. 9, pp. 403–404, 1975.

[50] W. T. Liu, K. B. Katsaros, and J. A. Businger, "Bulk parameterization of air-sea exchanges of heat and water vapor including the molecular constraints at the interface," *Journal of the Atmospheric Sciences*, vol. 36, no. 9, pp. 1722–1735, 1979.

[51] A. V. Soloviev and P. Schlüssel, "Parameterization of the cool skin of the ocean and of the air-ocean gas transfer on the basis of modeling surface renewal," *Journal of Physical Oceanography*, vol. 24, no. 6, pp. 1339–1346, 1994.

[52] A. Jessup, W. Asher, M. Atmane, K. Phadnis, C. Zappa, and M. Loewen, "Evidence for complete and partial surface renewal at an air-water interface," *Geophysical Research Letters*, vol. 36, no. 16, pp. L16601–1–5, 2009.

[53] R. A. Handler, P. S. Bernard, A. L. Rovelstad, and J. D. Swearingen, "On the role of accelerating fluid particles in the generation of reynolds stress," *Physics of Fluids A: Fluid Dynamics*, vol. 4, no. 6, pp. 1317–1319, 1992.

[54] W. R. McGillis, J. B. Edson, J. D. Ware, J. W. Dacey, J. E. Hare, C. W. Fairall, and R. Wanninkhof, "Carbon dioxide flux techniques performed during GasEx-98," *Marine Chemistry*, vol. 75, no. 4, pp. 267–280, 2001.

[55] C. S. Garbe, U. Schimpf, and B. Jähne, "A surface renewal model to analyze infrared image sequences of the ocean surface for the study of air-sea heat and gas exchange," *Journal of Geophysical Research: Oceans*, vol. 109, no. C8, pp. C08S15–1–18, 2004.

[56] R. A. Handler, R. P. Mied, G. J. Lindemann, and T. E. Evans, "Turbulent channel flows on a rotating earth," *Journal of Physical Oceanography*, vol. 39, no. 4, pp. 952–968, 2009.

[57] D. Turney and S. Banerjee, "Transport phenomena at interfaces between turbulent fluids," *AIChE Journal*, vol. 54, no. 2, pp. 344–349, 2008.

[58] N. V. Scott, R. A. Handler, and G. B. Smith, "Wavelet analysis of the surface temperature field at an air–water interface subject to moderate wind stress," *International Journal of Heat and Fluid Flow*, vol. 29, no. 4, pp. 1103–1112, 2008.

[59] G. Samanta, A. N. Beris, R. A. Handler, and K. D. Housiadas, "Velocity and conformation statistics based on reduced Karhunen-Loéve projection data from DNS of viscoelastic turbulent channel flow," *Journal of Non-Newtonian Fluid Mechanics*, vol. 160, no. 1, pp. 55–63, 2009.

[60] J. Milgram, R. A. Skop, R. D. Peltzer, and O. M. Griffin, "Modeling short sea wave energy distributions in the far wakes of ships," *Journal of Geophysical Research: Oceans*, vol. 98, no. C4, pp. 7115–7124, 1993.

[61] K. D. Housiadas, A. N. Beris, and R. A. Handler, "Viscoelastic effects on higher order statistics and on coherent structures in turbulent channel flow," *Physics of Fluids*, vol. 17, no. 3, pp. 035106–1–20, 2005.

[62] R. Peltzer, W. Garrett, and P. Smith, "A remote sensing study of a surface ship wake," in *OCEANS'85-Ocean Engineering and the Environment*, pp. 277–286, IEEE, 1985.

[63] W. Alpers and H. Hühnerfuss, "The damping of ocean waves by surface films: A new look at an old problem," *Journal of Geophysical Research: Oceans*, vol. 94, no. C5, pp. 6251–6265, 1989.

[64] J. Lucassen, "Longitudinal capillary waves. part 1. theory," *Transactions of the Faraday Society*, vol. 64, pp. 2221–2229, 1968.

[65] E. Lucassen-Reynders, A. Cagna, and J. Lucassen, "Gibbs elasticity, surface dilational modulus and diffusional relaxation in nonionic surfactant monolayers," *Colloids and Surfaces A: Physicochemical and Engineering Aspects*, vol. 186, no. 1, pp. 63–72, 2001.

[66] S. Brown, M. Triantafyllou, and D. Yue, "Complex analysis of resonance conditions for coupled capillary and dilational waves," *Proceedings of the Royal Society of London. Series A: Mathematical, Physical and Engineering Sciences*, vol. 458, no. 2021, pp. 1167–1187, 2002.

[67] A. Mikishev and A. Nepomnyashchy, "Nonlinear large-scale Marangoni convection in a heated liquid layer with insoluble surfactant," *Physical Review E*, vol. 82, no. 4, pp. 046306–1–12, 2010.

[68] X. Liu and J. H. Duncan, "The effects of surfactants on spilling breaking waves," *Nature*, vol. 421, no. 6922, pp. 520–523, 2003.

[69] K. P. Judd, S. Phongikaroon, G. B. Smith, and R. A. Handler, "Thermal structure of clean and contaminated free-surfaces subject to an impinging gas jet," *Experiments in Fluids*, vol. 38, no. 1, pp. 99–111, 2005.

[70] L. Scriven, "Dynamics of a fluid interface equation of motion for newtonian surface fluids," *Chemical Engineering Science*, vol. 12, no. 2, pp. 98–108, 1960.

[71] J. C. Shelley and M. Y. Shelley, "Computer simulation of surfactant solutions," *Current Opinion in Colloid & Interface Science*, vol. 5, no. 1, pp. 101–110, 2000.

[72] S. Phongikaroon, R. Hoffmaster, K. P. Judd, G. B. Smith, and R. A. Handler, "Effect of temperature on the surface tension of soluble and insoluble surfactants of hydrodynamical importance," *Journal of Chemical & Engineering Data*, vol. 50, no. 5, pp. 1602–1607, 2005.

[73] R. Handler, R. Leighton, G. Smith, and R. Nagaosa, "Surfactant effects on passive scalar transport in a fully developed turbulent flow," *International Journal of Heat and Mass Transfer*, vol. 46, no. 12, pp. 2219–2238, 2003.

[74] L. Shen, D. K. Yue, and G. S. Triantafyllou, "Effect of surfactants on free-surface turbulent flows," *Journal of Fluid Mechanics*, vol. 506, no. 1, pp. 79–115, 2004.

[75] Y. Kawaguchi, F. Li, Y. Bo, and K. Hishida, "Experimental and numerical investigation of the mechanism of drag reduction by surfactant additives and heat transfer," in *Proceedings of 6th Symposium on Smart Control of Turbulence*, pp. 1–14, 2005.

[76] B. Yu and Y. Kawaguchi, "Effect of weissenberg number on the flow structure: direct numerical simulation study of drag-reducing flow with surfactant additives," *International Journal of Heat and Fluid Flow*, vol. 24, no. 4, pp. 491–499, 2003.

[77] B. Yu, F. Li, and Y. Kawaguchi, "Numerical and experimental investigation of turbulent characteristics in a drag-reducing flow with surfactant additives," *International Journal of Heat and Fluid Flow*, vol. 25, no. 6, pp. 961–974, 2004.

[78] S. Ganesan and L. Tobiska, "A coupled arbitrary lagrangian–eulerian and lagrangian method for computation of free surface flows with insoluble surfactants," *Journal of Computational Physics*, vol. 228, no. 8, pp. 2859–2873, 2009.

[79] G. Samanta, K. D. Housiadas, R. A. Handler, and A. N. Beris, "Effects of viscoelasticity on the probability density functions in turbulent channel flow," *Physics of Fluids*, vol. 21, no. 11, pp. 115106–1–23, 2009.

[80] J. Xu, Z. Li, J. Lowengrub, and H. Zhao, "A level-set method for interfacial flows with surfactant," *Journal of Computational Physics*, vol. 212, no. 2, pp. 590–616, 2006.

[81] M. Lai, Y. Tseng, and H. Huang, "An immersed boundary method for interfacial flows with insoluble surfactant," *Journal of Computational Physics*, vol. 227, no. 15, pp. 7279–7293, 2008.

[82] W. T. Tsai and D. K. Yue, "Effects of soluble and insoluble surfactant on laminar interactions of vortical flows with a free surface," *Journal of Fluid Mechanics*, vol. 289, pp. 315–350, 1995.

[83] W. T. Tsai, "Impact of a surfactant on a turbulent shear layer under the air-sea interface," *Journal of Geophysical Research*, vol. 101, no. C12, pp. 28557–28568, 1996.

[84] W. T. Tsai and L. Hung, "Three-dimensional modeling of small-scale processes in the upper boundary layer bounded by a dynamic ocean surface," *Journal of Geophysical Research*, vol. 112, no. C2, pp. C02019–1–18, 2007.

[85] G. Tryggvason, J. Abdollahi-Alibeik, W. W. Willmarth, and A. Hirsa, "Collision of a vortex pair with a contaminated free surface," *Physics of Fluids A: Fluid Dynamics*, vol. 4, no. 6, pp. 1215–1229, 1992.

[86] A. Hirsa and W. Willmarth, "Measurements of vortex pair interaction with a clean or contaminated free surface," *Journal of Fluid Mechanics*, vol. 259, pp. 25–46, 1994.

[87] A. Hirsa, G. Korenowski, L. Logory, and C. Judd, "Determination of surface viscosities by surfactant concentration and velocity field measurements for an insoluble monolayer," *Langmuir*, vol. 13, no. 14, pp. 3813–3822, 1997.

[88] M. J. Vogel and A. H. Hirsa, "Concentration measurements downstream of an insoluble monolayer front," *Journal of Fluid Mechanics*, vol. 472, pp. 283–305, 2002.

[89] G. Samanta, K. D. Housiadas, A. N. Beris, and R. Handler, "Data reduction in viscoelastic turbulent channel flows based on extended Karhunen-Loéve analysis," *Journal of Non-Newtonian Fluid Mechanics*, vol. 165, no. 19, pp. 1386–1399, 2010.

[90] J. Lopez and J. Chen, "Coupling between a viscoelastic gas/liquid interface and a swirling vortex flow," *Journal of Fluids Engineering*, vol. 120, no. 4, pp. 655–661, 1998.

[91] S. McKenna and W. McGillis, "The role of free-surface turbulence and surfactants in air–water gas transfer," *International Journal of Heat and Mass Transfer*, vol. 47, no. 3, pp. 539–553, 2004.

[92] K. Morris, R. A. Handler, and D. W. Rouson, "Intermittency in the turbulent ekman layer," *Journal of Turbulence*, vol. 12, no. 12, pp. 1–25, 2011.

[93] H. R. Khakpour, L. Shen, and D. K. Yue, "Transport of passive scalar in turbulent shear flow under a clean or surfactant-contaminated free surface," *Journal of Fluid Mechanics*, vol. 670, pp. 527–557, 2011.

[94] G. Fortescue and J. Pearson, "On gas absorption into a turbulent liquid," *Chemical Engineering Science*, vol. 22, no. 9, pp. 1163–1176, 1967.

[95] J. C. Lamont and D. Scott, "An eddy cell model of mass transfer into the surface of a turbulent liquid," *AIChE Journal*, vol. 16, no. 4, pp. 513–519, 1970.

[96] P. Liss and P. Slater, "Flux of gases across the air-sea interface," *Nature*, vol. 247, pp. 181–184, 1974.

[97] L. Hasse, "Gas exchange across the air-sea interface," *Tellus*, vol. 32, no. 5, pp. 470–481, 1980.

[98] A. V. Soloviev and P. Schlüssel, "Evolution of cool skin and direct air-sea gas transfer coefficient during daytime," *Boundary-Layer Meteorology*, vol. 77, no. 1, pp. 45–68, 1996.

[99] P. Liss, "Processes of gas exchange across an air-water interface," in *Deep Sea Research and Oceanographic Abstracts*, vol. 20, pp. 221–238, Elsevier, 1973.

[100] B. Jähne, K. Münnich, and U. Siegenthaler, "Measurements of gas exchange and momentum transfer in a circular wind-water tunnel," *Tellus*, vol. 31, no. 4, pp. 321–329, 1979.

[101] W. Large and S. Pond, "Sensible and latent heat flux measurements over the ocean," *Journal of Physical Oceanography*, vol. 12, no. 5, pp. 464–482, 1982.

[102] F. Ocampo-Torres, M. Donelan, N. Merzi, and F. Jia, "Laboratory measurements of mass transfer of carbon dioxide and water vapour for smooth and rough flow conditions," *Tellus B*, vol. 46, no. 1, pp. 16–32, 1994.

[103] Y. Pan and S. Banerjee, "A numerical study of free-surface turbulence in channel flow," *Physics of Fluids*, vol. 7, no. 7, pp. 1649–1664, 1995.

[104] R. A. Handler, "Applications of direct numerical simulations to interfacial problems," in *Geoscience and Remote Sensing Symposium (IGARSS), 2012 IEEE International*, pp. 362–365, IEEE, 2012.

[105] R. Nagaosa, "Direct numerical simulation of vortex structures and turbulent scalar transfer across a free surface in a fully developed turbulence," *Physics of Fluids*, vol. 11, no. 6, pp. 1581–1595, 1999.

[106] R. Nagaosa and R. A. Handler, "Characteristic time scales for predicting the scalar flux at a free surface in turbulent open-channel flows," *AIChE Journal*, vol. 58, no. 12, pp. 3867–3877, 2012.

[107] R. Nagaosa and R. A. Handler, "Statistical analysis of coherent vortices near a free surface in a fully developed turbulence," *Physics of Fluids*, vol. 15, no. 2, pp. 375–394, 2003.

[108] R. Handler, J. Saylor, R. Leighton, and A. Rovelstad, "Transport of a passive scalar at a shear-free boundary in fully developed turbulent open channel flow," *Physics of Fluids*, vol. 11, no. 9, pp. 2607–2625, 1999.

[109] A. Kermani, H. R. Khakpour, L. Shen, and T. Igusa, "Statistics of surface renewal of passive scalars in free-surface turbulence," *Journal of Fluid Mechanics*, vol. 678, pp. 379–416, 2011.

[110] V. De Angelis, P. Lombardi, and S. Banerjee, "Direct numerical simulation of turbulent flow over a wavy wall," *Physics of Fluids*, vol. 9, no. 8, pp. 2429–2442, 1997.

[111] M. Fulgosi, D. Lakehal, S. Banerjee, and V. De Angelis, "Direct numerical simulation of turbulence in a sheared air-water flow with a deformable interface," *Journal of Fluid Mechanics*, vol. 482, pp. 319–345, 2003.

[112] H. Haußecker, S. Reinelt, and B. Jähne, "Heat as a proxy tracer for gas exchange measurements in the field: Principles and technical realization," *Air-Water Gas Transfer*, pp. 405–413, 1995.

[113] L. Kral and H. Fasel, "Numerical investigation of three-dimensional active control of boundary-layer transition," *AIAA Journal*, vol. 29, no. 9, pp. 1407–1417, 1991.

[114] R. D. Joslin, R. Nicolaides, G. Erlebacher, M. Y. Hussaini, and M. D. Gunzburger, "Active control of boundary-layer instabilities-use of sensors and spectral controller," *AIAA Journal*, vol. 33, no. 8, pp. 1521–1523, 1995.

[115] H. Choi, P. Moin, and J. Kim, "Active turbulence control for drag reduction in wall-bounded flows," *Journal of Fluid Mechanics*, vol. 262, pp. 75–75, 1994.

[116] J. Tang and H. H. Bau, "Feedback control stabilization of the no-motion state of a fluid confined in a horizontal porous layer heated from below," *Journal of Fluid Mechanics*, vol. 257, pp. 485–485, 1993.

[117] L. E. Howle, "Control of Rayleigh-Bénard convection in a small aspect ratio container," *International Journal of Heat and Mass Transfer*, vol. 40, no. 4, pp. 817–822, 1997.

[118] T. Marimbordes, A. Ould El Moctar, and H. Peerhossaini, "Active control of natural convection in a fluid layer with volume heat dissipation," *International Journal of Heat and Mass Transfer*, vol. 45, no. 3, pp. 667–678, 2002.

[119] R. H. Kraichnan, "Turbulent thermal convection at arbitrary Prandtl number," *Physics of Fluids*, vol. 5, no. 11, pp. 1374–1389, 1962.

[120] L. N. Howard, "Convection at high Rayleigh number," in *Applied Mechanics* (H. Görtler, ed.), ch. 2, pp. 1109–1115, Berlin: Springer, 1 ed., 1966.

[121] J. Deardorff and G. Willis, "Investigation of turbulent thermal convection between horizontal plates," *Journal of Fluid Mechanics*, vol. 28, no. 4, pp. 675–704, 1967.

[122] T. D. Foster, "Onset of convection in a layer of fluid cooled from above," *Physics of Fluids*, vol. 8, no. 10, pp. 1770–1774, 1965.

[123] T. D. Foster, "Intermittent convection," *Geophysical & Astrophysical Fluid Dynamics*, vol. 2, no. 1, pp. 201–217, 1971.

[124] S. Chandrasekhar, *Hydrodynamic and Hydromagnetic Stability*, ch. 2, pp. 9–71. Oxford, UK: Clarendon Press, 1 ed., 1961.

[125] P. G. Drazin and W. H. Reid, *Hydrodynamic Stability*, ch. 2, pp. 32–63. Cambridge,UK: Cambridge university press, 2 ed., 2004.

[126] R. Adrian, R. Ferreira, and T. Boberg, "Turbulent thermal convection in wide horizontal fluid layers," *Experiments in Fluids*, vol. 4, no. 3, pp. 121–141, 1986.

[127] T. Boeck and A. Thess, "Inertial Bénard-Marangoni convection," *Journal of Fluid Mechanics*, vol. 350, pp. 149–175, 1997.

[128] N. Kovalchuk, V. Kovalchuk, and D. Vollhardt, "Numerical study of the Marangoni instability resulting in surface tension auto-oscillations: General regularities of the system evolution," *Physical Review E*, vol. 63, no. 3, pp. 031604–1–10, 2001.

[129] N. Kovalchuk and D. Vollhardt, "Instability and spontaneous oscillations by surfactant transfer through a liquid membrane," *Colloids and Surfaces A: Physicochemical and Engineering Aspects*, vol. 309, no. 1, pp. 231–239, 2007.

[130] E. D. Siggia, "High Rayleigh number convection," *Annual Review of Fluid Mechanics*, vol. 26, no. 1, pp. 137–168, 1994.

[131] S. Grossmann and D. Lohse, "Prandtl and Rayleigh number dependence of the reynolds number in turbulent thermal convection," *Physical Review E*, vol. 66, no. 1, pp. 016305–1–6, 2002.

[132] M. Brocchini and D. Peregrine, "The dynamics of strong turbulence at free surfaces. part 1. description," *Journal of Fluid Mechanics*, vol. 449, no. 1, pp. 225–254, 2001.

[133] M. Brocchini and D. Peregrine, "The dynamics of strong turbulence at free surfaces. part 2. free-surface boundary conditions," *Journal of Fluid Mechanics*, vol. 449, no. 1, pp. 255–290, 2001.

[134] E. F. Bradley, P. Coppin, and J. Godfrey, "Measurements of sensible and latent heat flux in the western equatorial pacific ocean," *Journal of Geophysical Research: Oceans*, vol. 96, no. S01, pp. 3375–3389, 1991.

[135] J. J. Simpson and C. A. Paulson, "Mid-ocean observations of atmospheric radiation," *Quarterly Journal of the Royal Meteorological Society*, vol. 105, no. 444, pp. 487–502, 1979.

[136] B. C. Weare, "Uncertainties in estimates of surface heat fluxes derived from marine reports over the tropical and subtropical oceans," *Tellus A*, vol. 41, no. 4, pp. 357–370, 1989.

[137] M. R. Lewis, M. E. Carr, G. C. Feldman, W. Esaias, and C. McClain, "Influence of penetrating solar radiation on the heat budget of the equatorial pacific ocean," *Nature*, vol. 347, pp. 543–545, 1990.

[138] G. A. Wick, W. J. Emery, L. H. Kantha, and P. Schlüssel, "The behavior of the bulk-skin sea surface temperature difference under varying wind speed and heat flux," *Journal of Physical Oceanography*, vol. 26, no. 10, pp. 1969–1988, 1996.

[139] D. D. Gray and A. Giorgini, "The validity of the Boussinesq approximation for liquids and gases," *International Journal of Heat and Mass Transfer*, vol. 19, no. 5, pp. 545–551, 1976.

[140] K. Rajagopal, M. Ruzicka, and A. Srinivasa, "On the Oberbeck-Boussinesq approximation," *Mathematical Models and Methods in Applied Sciences*, vol. 6, no. 08, pp. 1157–1167, 1996.

[141] E. Spiegel and G. Veronis, "On the Boussinesq approximation for a compressible fluid," *The Astrophysical Journal*, vol. 131, pp. 442–447, 1960.

[142] J. M. Mihaljan, "A rigorous exposition of the Boussinesq approximations applicable to a thin layer of fluid," *The Astrophysical Journal*, vol. 136, pp. 1126–1133, 1962.

[143] A. Townsend, "Temperature fluctuations over a heated horizontal surface," *Journal of Fluid Mechanics*, vol. 5, no. 02, pp. 209–241, 1959.

[144] J. W. Deardorff, "Convective velocity and temperature scales for the unstable planetary boundary layer and for Rayleigh convection," *Journal of the Atmospheric Sciences*, vol. 27, no. 8, pp. 1211–1213, 1970.

[145] C. A. Fletcher, *Computational Techniques for Fluid Mechanics*, ch. 5, pp. 98–156. NY: Springer-Verlag, 2 ed., 1991.

[146] C. A. Fletcher, *Computational Galerkin Methods*, ch. 1, pp. 1–68. NY: Springer-Verlag, 1 ed., 1984.

[147] J. P. Boyd, *Chebyshev and Fourier Spectral Methods*. Mineola, NY: Dover Publications, 2 ed., 2001.

[148] D. Gottlieb and S. A. Orszag, *Numerical Analysis of Spectral Methods*, ch. 1, pp. 1–68. Philadelphia, PA: SIAM, 1 ed., 1977.

[149] P. Spalart, W. Jou, M. Strelets, and S. Allmaras, "Comments on the feasibility of les for wings, and on a hybrid RANS/LES approach," *Advances in DNS/LES*, vol. 1, pp. 4–8, 1997.

[150] P. R. Spalart, "Detached-eddy simulation," *Annual Review of Fluid Mechanics*, vol. 41, pp. 181–202, 2009.

[151] D. Goldstein, R. Handler, and L. Sirovich, "Modeling a no-slip flow boundary with an external force field," *Journal of Computational Physics*, vol. 105, no. 2, pp. 354–366, 1993.

[152] J. Kim, P. Moin, and R. Moser, "Turbulence statistics in fully developed channel flow at low reynolds number," *Journal of Fluid Mechanics*, vol. 177, no. 1, pp. 133–166, 1987.

[153] J. Bush, "18.357 interfacial phenomena, fall 2010." MIT OpenCourseWare: Massachusetts Institute of Technology, 2010 (Accessed 21 Apr, 2014). http://ocw.mit.edu/courses/mathematics/18-357-interfacial-phenomena-fall-2010. License: Creative Commons BY-NC-SA.

[154] J. C. Slattery, L. Sagis, and E. S. Oh, *Interfacial Transport Phenomena*. NY: Springer, 2 ed., 2007.

[155] D. A. Edwards, H. Brenner, and D. T. Wasan, *Interfacial Transport Processes and Rheology*. Boston: Butterworth-Heinemann, 1 ed., 1991.

[156] J. Saylor, G. Smith, and K. Flack, "The effect of a surfactant monolayer on the temperature field of a water surface undergoing evaporation," *International Journal of Heat and Mass Transfer*, vol. 43, no. 17, pp. 3073–3086, 2000.

[157] S. Bower and J. Saylor, "The effects of surfactant monolayers on free surface natural convection," *International Journal of Heat and Mass Transfer*, vol. 54, no. 25, pp. 5348–5358, 2011.

[158] B. Jähne and H. Haußecker, "Air-water gas exchange," *Annual Review of Fluid Mechanics*, vol. 30, no. 1, pp. 443–468, 1998.

[159] R. Wanninkhof, J. R. Ledwell, and W. S. Broecker, "Gas exchange-wind speed relation measured with sulfur hexafluoride on a lake," *Science*, vol. 227, no. 4691, pp. 1224–1226, 1985.

[160] R. Wanninkhof, J. R. Ledwell, W. S. Broecker, and M. Hamilton, "Gas exchange on mono lake and crowley lake, california," *Journal of Geophysical Research: Oceans*, vol. 92, no. C13, pp. 14567–14580, 1987.

[161] R. Wanninkhof, "Relationship between wind speed and gas exchange over the ocean," *Journal of Geophysical Research: Oceans*, vol. 97, no. C5, pp. 7373–7382, 1992.